Are ‘exceptionally’ preserved skeletal fossils necessarily exceptional chemically and cytologically?

Dana Elaine Korneisel

Thesis submitted to the faculty of the Virginia Polytechnic Institute and State University in partial fulfillment of the requirements for the degree of

Master of Science
In
Geosciences

Shuhai Xiao, Chair
Sterling J. Nesbitt
Sarah Werning

July 16, 2019
Blacksburg, VA

Keywords: taphonomy, Lagerstätte, Jehol Biota, Yixian Formation, Cretaceous

Are ‘exceptionally’ preserved skeletal fossils necessarily exceptional chemically and cytologically?

Dana Elaine Korneisel

ABSTRACT

At the macroscopic scale, vertebrate fossils are considered exceptional when non-biomineralized (soft) tissues are preserved. Histologically, high quality is defined by trueness to original shape of a bone, preservation of fine details (e.g. canaliculi), and presence or absence of matrix material in void spaces. Some fossils are hypothesized to preserve cells and durable organelles. Traditionally, cytological details and biomolecular remains have been sought in exceptional fossils. Durable cytological features such as melanosomes do appear to follow feather preservation, but traditionally exceptional fossils are not necessarily exceptional on a microscopic scale. Here, we analyze a feathered dinosaur specimen from the Jehol Lagerstätte to assess claims of blood cell preservation and the state of potential biomolecular preservation. *Beipiaosaurus inexpectus* is a fairly complete specimen with preserved feathers. Though crushed, fine details in thin section are prevalent. Using Raman spectroscopy, Energy Dispersive X-ray Spectrometry, and Time-of-Flight Secondary Ion Mass Spectroscopy we found no evidence of exceptional molecular preservation. Instead, we found evidence that the vasculature, once hypothesized to contain preserved red blood cells, is filled with clay minerals, with the purported cells chemically indistinguishable from materials of other shapes infilling the vessels. Despite yielding exceptional fossils, the preservational environment of the Jehol biota does not necessarily preserve exceptional details cytologically or biomolecularly. Consequently, we conclude that a systematic approach to biomolecular and cytological preservation studies should rely on traits other than classic exceptional preservation.

Are ‘exceptionally’ preserved skeletal fossils necessarily exceptional chemically and cytologically?

Dana Elaine Korneisel

GENERAL AUDIENCE ABSTRACT

What makes a fossil particularly excellent? Traditionally, fossils from animals with skeletons were considered high quality when many or most of the bones from an animal are preserved. If these bones line up with one another like they would in the animal when it was alive (i.e. are articulated) the fossil is even better. To be exceptional, though, soft tissues, or parts of the animal that were not hardened with minerals while the animal lived (e.g. feathers, skin) need to be preserved. All of these traits can be observed with the naked eye. With the use of a microscope, we can see how much a skeleton has been crushed and whether the spaces in the bone for blood vessels and cells have been well preserved. Additionally, we may be able to observe preserved cells, which would be exceptional. On an even smaller scale, the molecules present in a bone might be well or poorly preserved. How much the minerals that make up the bone have changed chemically from when the animal was alive is one indicator of quality. Another might be preservation of molecules that come from the animal such as DNA and the proteins present in bone. In this study, we chose an exceptional fossil based on the traits visible to the naked eye (many of the bones are present and it has feathers) and looked for evidence of cell and unique molecule preservation. On the microscope, we saw beautiful details of the structures in the bone that held bone cells and blood vessels. We also observed red spheres which have been described by other researchers as possible blood cells in the spaces for blood vessels. Using three types of machine which can identify minerals, elements, and molecules in the bone and vessels, we did not find any evidence that the spheres represent preserved blood cells. Nor did we find any

evidence of exceptional molecules. However, we did find evidence that the bone itself is not highly changed from when the animal lived, though we see elements and molecules in the vessels that probably did not come from the animal. We started this study knowing that the fossil we chose is exceptional in some ways, but what we found shows that it has a mix of excellent and poor traits visible on the microscope and it does not have any excellent traits in terms of its molecules besides the minerals in the bone itself. We conclude that fossils that are exceptional in the traditional sense are not necessarily exceptional in other ways.

TABLE OF CONTENTS

LIST OF FIGURES

ATTRIBUTION

This project was conceived of by SX and designed by DEK and SX. Data collection and analyses were conducted by DEK. Figures were completed by DEK with input from SX, SJN, and SW. Writing was composed by DEK, with advice from and edits by SX, SJN, and SW.

1. Abstract

At the macroscopic scale, vertebrate fossils are considered exceptional when non-biomineralized (soft) tissues are preserved. Histologically, high quality is defined by the preservation of fine details such as canaliculi and the absence of matrix material in the bone. Some fossils are hypothesized to preserve cells and durable organelles. Traditionally, cytological details and biomolecular remains have been sought in exceptional fossils. Durable cytological features such as melanosomes do appear to follow feather preservation, but traditionally exceptional fossils are not necessarily exceptional on a microscopic scale. Here, we analyze a feathered dinosaur specimen from the Jehol Lagerstätte to assess claims of blood cell preservation and the state of potential biomolecular preservation. *Beipiaosaurus inexpectus* is a fairly complete specimen with preserved feathers. Though crushed, fine details in thin section are prevalent. Using Raman spectroscopy, Energy Dispersive X-ray Spectrometry, and Time-of-Flight Secondary Ion Mass Spectroscopy we found no evidence of exceptional molecular preservation. Instead, we found evidence that the vasculature, once hypothesized to contain preserved red blood cells, is filled with clay minerals, with the purported cells chemically indistinguishable from materials of other shapes infilling the vessels. Despite yielding exceptional fossils, the preservational environment of the Jehol biota does not necessarily preserve exceptional details cytologically or biomolecularly. Consequently, we conclude that a systematic approach to biomolecular and cytological preservation studies should rely on traits other than classic exceptional preservation.

2. Introduction

The Jehol Biota of the Yixian Formation in Northeast China is considered a Lagerstätte (1-3), an exceptional site both in the concentration of fossils and in the quality of preservation (4, 5). The Lower Cretaceous lake sediments that host the biota are famous for preserving the earliest known angiosperms (6), abundant avialians (7-10), and many specimens surrounded by epidermal outlines including resplendent feathers (11-15). The abundance of fossil specimens includes lacustrian, terrestrial, and flying vertebrates and invertebrates (2, 9, 16-20). The fossils are often articulated and preserve the morphology of soft tissues: the 'tails' of three-tailed mayfly larvae (*Ephemeropsis trisetalis*), carbonaceous films showing the body outline of frogs and salamanders, and feathers on the avialians and other dinosaurs are common in the formation. Soft tissue preservation is what makes the fossils from the Jehol Biota exceptional on the macroscopic scale. (3, 5).

Exceptional preservation is more difficult to assess on a microscopic level. One sign of exceptional preservation would be fine details preserved on the cytological level. Though most specimens preserve lacunae, the details of canaliculi are not always visible (21). Possible soft tissues have been reported multiple times in dissolved fossil bone (22-25) though alternatively interpreted as bacterial in origin (26). Vasculature is easily distinguishable, but fossils that do not contain sediment and diagenetic minerals in their vasculature are harder to come by (21). Though Jehol fossils are often flattened (27), many preserve the fine details of canaliculi (28, 29). Melanosomes (alternatively interpreted as bacteria (30)) with intact melanin have been found in fossilized eyes, hairs, and feathers (31-34) including those in the Jehol biota (32, 33), indicating that some Jehol specimens are high quality in their cytological preservation. Jehol specimens have also been proposed to contain fossilized blood cells (28). Though the first putative blood

cells were described in 1907 (35), fossilization of blood cells became a popular subject at the end of the 20th and into the 21st century (e.g. (23, 28, 36, 37)). Authors putting forth a blood cell hypothesis at the time often advised further study (23, 24, 36, 38), but since then, only a fraction of these hypotheses have been investigated further (26, 39, 40). Most are unresolved (28, 35-37, 41, 42). A recent study asserting red blood cell preservation (43) extensively examined the structures in question with a variety of chemical methods and considered a wide range of non-chemical factors (e.g. blood cell size, shape, & location in the vessels).

The range of biomolecular durability is still being established, but differences in preservation potential between biomolecules is well established (44). Collagen structures are very durable and the molecule itself may be preserved in fossil specimens (45-48). Lipids are somewhat durable (44, 49). The detection of possibly ancient amino acids is alluring, and the discussion of how to achieve this goes beyond vertebrate paleontology (50). Recent Cenozoic proteins and their associated amino acids are considered reliably detectable (51, 52), but their reliability in more ancient fossils is still being discussed (53-56). DNA has been established to degrade rapidly and the special circumstances which allow for its preservation beyond the timescale of thousands-of-years has been discussed with nuance (57-59). The predictability of other molecular and cytological preservation is not as well established. Studies have often taken the approach of looking for biomolecule preservation in exceptional fossils, as exceptional features on a large scale may indicate favorable conditions for the preservation of biomolecules (34, 48, 60, 61).

Here, we examine the holotype of *Beipiaosaurus inexpectus*, a macroscopically exceptional feathered dinosaur from the Yixian Formation. This specimen has been purported to contain fossilized red blood cells (28). To assess the quality of preservation on the cytological

and molecular level, we aim at determining the composition of the putative blood cells, the degree of diagenetic alteration of the specimen, and whether biomolecules can be detected. To accomplish this, we utilized a combination of analytical tools including light microscopy, Scanning Electron Microscopy (SEM), Energy Dispersive X-ray Spectroscopy (EDS or EDX), Raman spectroscopy, and Time of Flight Secondary Ion Mass Spectrometry (TOF-SIMS). Although each analytical tool has its limitation, the combined strengths of these tools offer unprecedented insights into the preservation quality of an exceptional Jehol fossil.

3. Geology

The Yixian Formation is composed of 110-150 meters of mudstones, siltstones, and fine sandstones interbedded with volcanic tuffites (62). These fine sediments preserve an astounding density of fossils, many with preserved traces of soft tissues (4, 5, 9). Palynological data (63) and radiometrically dated volcanic ashes (64) throughout the otherwise extremely fine-grained and finely laminated shales (62) make it possible to precisely date the Yixian and underlying Tuchengzi formation (Figure 1)(65-69). Multiple analyses ($^{40}Ar/^{39}Ar$ and U/Pb SHRIMP) of volcanic tuffs interbedded with the primary vertebrate-bearing beds at Sihetun give dates of 124.6-124.7 Ma, thus dating the specimen used in this study to the Aptian Age of the Early Cretaceous Period (64, 67). Fossils in the Yixian Formation are known from a number of productive and closely spaced localities. These include the Huangbanjigou site, which produced *Archefructus*, the nearby and largely correlatable site at Jianshangou, home of *Manchurochelys liaoxiensis* and many feathered birds, as well as the stratigraphically lower Sihetun site, which bore *B. inexpectus* (Figure 1, B). These localities are in the Beipiao Bird Fossil National Nature Reserve, an area dominated by Yixian sediments and volcanic rocks (64).

4. Materials and Methods

Newly thin sectioned specimens come primarily from a small collection of gastralia fragments from *B. inexpectus* (IVP V11559) stored with the original thin sections from Yao et al. (2002). Mixed in with this material were fragments of petrified wood from the Yixian Formation of an unknown species – presumably a gymnosperm given the age of the locality (see table 1). The layer bearing *B. inexpectus* (in Wang et al 1999's Layers 25-29) underlies a tuff dated to between 124.35 and 126.1 Ma at the Sihetun locality of the Yixian Formation by less than 3.5 m (64). The original thin sections were covered in a highly fluorescent epoxy as well as a glass coverslip, so were not useful for Raman, EDS, SEM, and TOF-SIMS chemical analyses.

a. Thin sectioning: To access the spheres for chemical analysis and make the areas of interest in this sample visible, thin sectioning was necessary. To make thin sections that could be used to acquire quality Raman spectroscopy, EDS, and TOF-SIMS data, we embedded a gastralium segment in Castolite AC Polyester Resin. Before we imbedded new samples, we tested cured Castolite AC using Raman spectroscopy and found that its background fluorescence was low enough not to obscure Raman peaks. After embedding the specimens in a vacuum, we cut 0.5 mm slices on an Isomet 1000 precision saw using tap water to fill the basin and approximately 5 mL of Buehler Cool 2 Cutting Fluid for cooling. Before each new specimen, we cut 3-5 mm deep in a priming block to clean the blade for a smooth cut. We air-dried slices overnight, 12 hours at minimum, roughened part of a plexiglass slide about the size of the slice with a 120 grit sanding sponge, then mounted the slice in the roughened space with Loctite ultragel control commercial superglue. Mounted slices were then ground until thin enough to view details in transmitted light (approximately 100 µm thick) on a Metaserv 2000 Grinder/Polisher using a series of 240, 400, and 800 grit papers. First, we ground the specimens

on 240 grit until about 300 µm thickness, followed by 400 grit to half the thickness (150 µm, measured tactilely), and 800 grit until final thickness, judged on a light microscope. 1200 grit paper was initially used for additional grinding when the specimen still appeared dark under a microscope after grinding on 800 grit paper, but this appeared to scratch the specimen and was not used after the first section processed. Sectioned petrified wood was processed in the same way prior to the bone sections but cut at a thickness of 1 mm due to complications from considerable density changes in the specimen. Very dense silicified wood deflected the blade laterally, which caused the slice to fracture at the plane of density change. Researchers unfamiliar with wood sectioning should note that this process takes considerably longer than bone sectioning, and different methods are likely more effective.

b. Raman Spectroscopy: Raman spectroscopy became available for research in the 1960s, but paleontologists started to utilize it much later, beginning with invertebrate paleontology (70-74) and being used more often in taphonomy of invertebrates and vertebrates later on (75-78). Researchers have explored questions of exceptional preservation in plant fossils using Raman spectroscopy (74). Extensive research has also been done on a wide range of ambers (79). In vertebrates, Thomas et al. (77) focused on degrees of diagenetic alteration in the apatite of fossil humeri, and their further work (78) sought to establish Raman spectroscopy as a way to evaluate diagenetic alteration and to screen specimens for further geochemical analysis. Subsequently, Thomas et al. (79) examined soft-tissue preservation with a study of both fossil feathers and other carbonaceous compression fossils, looking for evidence of pigment preservation (79). Minerals such as pyrite and iron oxides have distinctive peaks on a Raman spectrum (80, 81). In short, Raman studies on vertebrate fossils have focused largely on how much original chemistry is preserved, looking at the most common minerals in bones and teeth.

As this is a central goal in our study of *B. inexpectus*' chemical and/or cytological preservation, Raman spectroscopy was selected as an inexpensive and useful analytical technique for this study.

To test alternative hypotheses for the identity of putative blood cells as framboids of iron minerals and to define the quality of preservation, we employed Raman spectroscopy to analyze *B. inexpectus* specimens. All Raman spectra were obtained from thin sectioned material. Data were collected on a high-resolution 800 mm focal length spectrometer (JY Horiba LabRam HR800) with a 785 nm laser at Virginia Tech's Raman Spectroscopy laboratory. The maximum power of the laser was 150 mW at the source. At full power, the laser burned through the thin section, so measurements were made with five second collections at 1/10 power. This decreased the intensity of the peaks, but also limits the addition of epoxy peaks in the measurements. The 514 nm laser, standard for inorganic materials, produced too much fluorescent background to be of use. Raman spectra were baselined using Fityk and CrystalSleuth. The CrystalSleuth database was referenced for interpreting the spectra.

c. Energy Dispersive X-ray Spectrometry: To locate vessels exposed on the surface of thin sections and get a general idea of variation of materials inside and outside of the vessels, we loaded samples into a Hitachi TM-3000 Tabletop SEM coupled with an EDS system. We left the samples uncoated, but surrounded them with aluminum tape to improve conductivity, and used Quantax70 to interpret and visualize the EDS data. This technique was readily available in the Virginia Tech Paleobiology Lab and offered the opportunity to screen for samples with exposed vessels to scan in subsequent TOF-SIMS analysis. From these preliminary scans, we identified VT-L2 as the best candidate for TOF-SIMS because of the relative abundance of vessels exposed on the surface of the section.

After preforming our TOF-SIMS analyses, we collected additional EDS data on an FEI Quanta 600FEG environmental SEM with both back scattered electron (BSE) and secondary electron (SE) capability operating at a voltage of 5-20 kV. Samples were coated in a mixture of gold and palladium to improve resolution and surrounded by aluminum tape for the same purpose. We used the attached Bruker EDX to collect additional mapped data and quantitative point analyses on vessel fills.

d. Time of Flight - Secondary Ion Mass Spectrometry: TOF-SIMS has been used extensively in clinical studies of modern bone (82) from identifying biomolecules to characterizing pathologies. It has also been used to identify biomolecule signatures in fossil bone (31) and to estimate the 'half-life' of a variety of organic compounds (e.g. DNA & collagen). Relative to other mass spectrometers for fossil analysis, TOF-SIMS is minimally destructive, only sampling a very thin layer of ions from a surface. It creates a map of relative ion abundance across an area of a specimen, can analyze both organic and inorganic molecules at the same time, and can detect molecules as well as individual elements (83). It has been used to analyze fossil melanosomes, and spectra can be analyzed at small points (pixels) of the ion map, allowing the distinction of microstructures from the matrix background (32).

TOF-SIMS also has limitations. A particular area (about 5nm in diameter) can only be sampled once, as the primary ion beam breaks apart a number of bonds, altering the molecules at the sampling site. Additionally, when using TOF-SIMS for large organic molecules, the primary ion beam breaks apart these molecules, yielding multiple peaks from fragments that are not typically specific to a larger molecule. We can compare the spectra to standards, but specific assignment of each peak is not always possible (83). Perhaps one of the biggest drawbacks of TOF-SIMS is that, because it was developed to characterize the presence and absence of simple

molecules and ions, non-synthetic specimens, especially those with a complex chemistry like fossil bone, stretch the capacity of this analytical tool; data from biological specimens are much more complex than traditional TOF-SIMS data from synthetic materials. With these complications in mind, we decided to utilize this technique due to its superb precision.

As we could not thin section unembedded fragments, we ground a fresh edge on a hand sample of gastralia in finely bedded mudstone matrix leant to us by IVPP from V11559 on fresh 240 and 800 grit paper on a Metaserv 2000 water grinder. Just prior to scanning, the ground edge was cut to approximately one millimeter thickness with a Dremel tool and rinsed with isopropyl alcohol to remove surface contamination undoubtably present from handling of the specimens during collection, storage, and processing. Though isopropyl may carry away endogenous organics, we felt it was necessary as much of the handling of these specimens was not done with chemical analyses in mind. This specimen was mounted on a silicon stub to be placed into the TOF-SIMS's vacuum chamber. Areas of interest were sputtered with a 2 kV Cesium beam for a minimum of 5 minutes to remove surface contamination. Cesium sputtering removes organics more quickly than inorganic material to reveal a clean surface at depth. Spectra were acquired from the sputtered surfaces using a 30 kV Bismuth ion beam as bismuth is not of biological interest and excites negative species. The primary species was Bi1 for the thin sectioned specimen and Bi3 for the unembedded, in situ specimen.

Original data are stored at the University of Texas at Austin in the care of the Texas Materials Institute servers. We remotely accessed the data and IONTOF software associated with the machine for data processing. The first step of processing TOF data is to calibrate mass, which we did using the following expected negative species: C, ^{18}O, O_2, F, Na, C2, Al, Si, P, Cl, ^{37}Cl, PO, PO_2, and PO_3. The software identifies peaks imperfectly and cuts off tails which are part of

the peak. So, after identifying calibration peaks, we manually adjusted the width or location of each range to cover the whole peak. We then assigned non-calibration peaks starting at low masses and identifying larger mass peaks when possible. In decisions between possible masses, we referred to the deviation measure (the difference of an observed peak from the expected location for a given secondary ion) and aimed for deviations below 200 ppm (very close to what would be expected for the identity assigned). When multiple options fit this criteria, we favored identities where a smaller elements of the larger molecule were already confidently assigned. For example, when we knew Silicon and Oxygen were present (masses 28u and 16u respectively), we could confidently assign the unidentified mass 60u to SiO_2 rather than a same-mass less likely compound such as C_5. We could not always discern the additional components of shouldered peaks but split these peak ranges in the nadir of the valley or shoulder when distinguishable by the IONTOF software.

5. Results

a. Histology: Sections VTL1 through VTL5, a series of longitudinal thin sections from a fragment of *B. inexpectus* gastralia, are roughly rectangular in shape with a projection of bone extending beyond the length of the thickest part from an uneven break in the fragment. The texture does not differ much between the exterior and interior of the bone. The collagen patterns are unorganized when observed with a quartz wedge. Most of the vascular canals run parallel to the bone surface but anastomose laterally between visible channels in section and through the depth of the thin section. Osteocytes are visible in each of these sections and are generally lenticular in shape (Figures 2. B-D & 3. 1-4). Some canaliculi are visible in longitudinal section. Osteocytes are dense throughout the sections except at the bone margin and directly adjacent to vascular channels.

Sections VTX1 and VTX2 were cut in cross section in sequence from a 3.5 × 1 mm fragment in the same collection as the longitudinal sections discussed above. The slices are gently curved, part of the circular cross section of another gastralia or small rib fragment. Only primary osteons are apparent in cross section, and canaliculi are readily visible in cross section.

New thin sections visually resemble the original sections from Yao et al. 2002 despite having been taken from different bone fragments (Table 1). Like the Yao sections, ours contain a variety of colors and shapes of vessel fill, from massive and opaque to small grains of a very light translucent orange (Figure 3, 1-4). Translucent red-orange spheres are visible throughout the vascular channels of the bone in longitudinal section. Cross sections reveal dark-filled lacunae and primary osteons; the variation in textures and colors of vessel fill is not apparent in this view and neither are the spheres.

The spheres are more abundant at points where two channels connect (Fig 3, 4) and places where the adjacent channel is filled with non-spherical material, especially translucent orange and red-orange material. They range in color from pale orange to red-orange, overlapping the color range of but never appearing as deeply red as non-spherical vessel fill. In some vessels, it is unclear whether the fill is very dense individual spheres or an amalgamation with some rounded portions (Fig 3, 1). The individual spheres range in size from 6 to 15 µm, but the majority are about 10 µm in diameter. In areas where the spheres are easily distinguished from one another and sparse, and especially for paler orange spheres, the external texture appears bumpy with a texture of 1-3 µm round elements visible when adjusting focus through the depth of the section.

b. Raman Spectroscopy: Raman spectra acquired from across these specimens are characterized most notably by a complex of peaks around 1000-1300 cm^{-1}, identified in previous publications as Raman bands of organic compounds such as amides (73, 84-86) (Figure 3). These are extremely similar to other spectra obtained from fossil dinosaur bone (e.g. (86, 87)).

Apatite peaks are visible in most of the Raman spectra. Raman peaks for apatite in enamel are known to shift between 962 cm^{-1} in modern bone and fossil bone with little alteration and 966 cm^{-1} in fluorapatite and highly altered fossil bone (78). The average position for the apatite peaks in our samples is 962.4 cm^{-1}, much nearer unaltered enamel apatite than inorganic fluorapatite.

c. Energy Dispersive X-ray Spectrometry: The most notable species in the bone under EDS are, of course, phosphorus & oxygen (Fig 4, D&H). The signals from filled vessels differ across the thin section. Some are dominated by aluminum & silicon, indicating the possible presence of clay minerals (F&G). At other locations, carbon is concentrated in the vessels and

abundant in void spaces and fractures in the bone. Color cannot be distinguished on SEM, and texture is difficult to compare with what is observable under light microscopy, but the exposed vessel fills scanned did not show unique chemical signatures indicative of biological origin. We did not detect notable variation in Fe, S, or Mn between vessel fills and the bone.

d. Time of Flight – Secondary Ion Mass Spectrometry:

i. Thin Section

Longitudinal thin section VTL2 was initially selected for TOF-SIMS study because vessels exposed at the surface of the sample were more common than in the other four serial longitudinal sections when scanned with SEM. We identified a surface with visible vessels and collected both a full-area scan of 500 by 500 μm, then zoomed in for a closer scan of the exposed vessel. The exposed fill is approximately tubular and part of the vessel is unfilled. Silicates do appear to be filling surrounding void spaces more than the vessels themselves, and the overwhelming components of the bone are phosphates without observed influence of Fluorine, in line with Raman spectra results on apatite alteration. Carbon and organics generally appear to be dispersed evenly throughout the bone, but with some extra concentration in the vessels, especially of larger organic species. Iron, Manganese, and oxides of these metals were not detected in elevated amounts in any part of the section.

ii. In-situ Section

This specimen consists of a cross-section of a gastralium fragment, thinly laminated mudstone surrounding it, and a round orange-colored concretion (TABLE 1?). The laminations of the mudstone dip between the concretion and the bone. This scan is a composite of 21 scan segments and thus measures 1500 by 3500 μm (Fig 5, A-C). This scan shows a clear difference

in composition between the bone and surrounding matrix, silicates in the matrix and phosphate in bone, but also reveals silicates in the larger pore spaces of the bone, indicating that authigenic or matrix minerals could be contributing to vessel fills (Fig 5, compare D to I). Organics are concentrated in the bone and at the contact between the laminated matrix & concretion, but not abundant within the concretion or matrix (J). The presence of organics at the permeable contact between the concretion and matrix imply that they may have been carried in by fluids or present due to microbial occupation of pore space and fractures. Very low levels of iron and manganese oxides (compared to silica) are evenly dispersed through the matrix and nearby concretion. Aluminum is more densely concentrated in the concretion, otherwise following the presence of silicon except for in the same area influenced by Cl, where it is more abundant in the margin of the bone than some portions of the sediment and deeper into the cross section of the bone. Interestingly, Cl and ^{37}Cl are concentrated in the bone, but also infiltrate the matrix in contact with the bone (Fig 5, see E & F). The concentration decreases with distance from the bone, indicating that Cl may have been incorporated into the bone or deposited in pore spaces in the bone in past concentrated fluids, now dispersing in low salinity surface and subsurface waters. If the bone is modified to chlorapatite, this indicates that the level of environmental impact on bone chemistry may be greater than implied by Raman comparisons which expected modified hydroxylapatite to approach fluorapatite chemistry. Despite the peak position in Raman, F is abundant throughout the sampled area and concentrated in the bone (H).

6. Discussion & Conclusion

The preservation of soft tissue structures such as the feathers of *Beipiaosaurus inexpectus* is exceptional in the span of fossil quality. In our suite of analyses, we collected evidence that the apatite of the holotype's bone is also minimally altered in terms of incorporated fluoride, resembling modern bone more closely than non-biological apatite. However, we also observed concentrated chlorine in the bone, possibly the result of apatite alteration, and higher than surrounding concentrations of fluorine in TOF-SIMS analysis. Despite crushing and possible alteration, the histological details preserved are clearly excellent. Fine webs of canaliculi are easily observed throughout longitudinal and cross sectional thin sections of this specimen. However, the prevalence of abundant inorganic materials in the vasculature of this specimen indicates that visible excellence does not necessarily indicate a fossil is pristine. It is hard to imagine a mechanism for cytological preservation in a specimen where the open spaces have been subject to authigenic crystallization or infiltrated by diagenetic fluids. Molecularly, we did not recover evidence of exceptional biomolecular preservation. Instead, we see concentrations of organics within the bone and other permeable spaces in the surrounding sediment (Fig 5, J), and the segments of organics collected are not attributable to a unique compound. Since the exceptional qualities of this specimen do not seem to correlate to anything special on the microscopic scale, we wonder what qualities could be predictive of potentially productive specimens for biomolecular studies. The assumption that biomolecules, if preserved, should be present in exceptional fossils has been subverted somewhat by studies which searched "low-quality" fossils for blood cell and soft tissue preservation (24, 43). If valid, these at least show that soft tissue preservation is not exclusive to traditionally exceptional fossils. With the addition of the evidence herein, that a traditionally exceptional fossil does not represent a pristine

environment for cytological and molecular preservation, it seems that traditional views of quality are not enough to predict microscopic-scale quality.

The spheres in *B. inexpectus*' vasculature have the texture of framboids, the most popular alternative hypothesis for the identity of purported blood cells in the fossil record. However, we have collected no evidence that implies any pyrite (the most common framboid forming mineral) is currently or was previously present. Pyrite framboids sometimes occur in confined spaces in anoxic environments, often alongside more massive pyrite grains and crystals (88). In the case of *B. inexpectus*, there is neither pyrite in the vessels nor massive pyrite in the surrounding sediment. Still, the diagenetic origins of framboidal minerals in fossil-bearing beds presents a gap in our knowledge of taphonomy. Though framboids are not fossils, they may be evidence of bacterial activity during the decomposition of an organism's soft tissues (89, 90). This activity may account for the presence of low oxygen zones in boney pores. There is not enough iron in blood to account for the amount of Fe present in pyrite framboids (43), and even though this could conceivably have been a contributor to pyrite formation, it seems unlikely that we could learn anything about an organism or its environment from the demonstration of this relationship between heme and pyrite iron. Many purported blood cells are visually similar to those we observed in this study (35, 37, 40, 41), and they could share traits of diagenetic history across many fossil localities, revealing similarities in the taphonomic histories of very different fossil-bearing environments. Their morphology and presence in enclosed spaces is distinctive, but their mineral makeup is usually guessed in the absence of pyrite. We appear to have clay mineral framboids, possibly pseudomorphs of previously formed framboidal pyrite. The patterns in their formation and mineral replacement could yield new insights into the pathway from sediment deposition to exhumation, and the history of fluids in the sediments of this Lagerstätte.

Lagerstätten are presumed to exist due to very specific and rare preservational environments. The taphonomic processes which favored integumentary preservation and well-articulated specimens in the Yixian Formation are not necessarily those which would produce cellular-level and biomolecule-level preservation. For this reason, indicators other than the designation “exceptional” are likely better predictors of cytological and biomolecule preservation. We feel that a deeper understanding of fluid history throughout diagenesis of Lagerstätten and other fossil sites, fluids having a large potential to influence local chemistry, may yield these indicators. By identifying and screening by these traits, we could make better informed future decisions of which specimens to sample destructively in our search for unusually excellent fossils.

7. Acknowledgements

This work was completed as part of an MS thesis by DEK. First, we thank Jinxian Yao for lending us the thin sections used in her initial histological study of *Beipiaosaurus inexpectus* and associated bone chips for additional thin sectioning. We thank Xu Xing and the IVPP for lending us additional bone fragments used in this study. We thank Andrei Dolocan at the University of Texas at Austin for his expertise with the Time of Flight Secondary Ion Mass Spectrometer, assistance with and instruction in data processing, and advice on data interpretations. We thank Chunchi Liao and Shiying Wang for their help in the field, expertise on *B. inexpectus* and the Yixian Formation, friendship, and hospitality. We are grateful to Caitlin Colleary for helpful conversation and assistance with the use of TOF-SIMS in this study and to Qing Tang for instruction in EDS and advice on data presentation for these analyses. We thank The Geological Society of America, The International Conference on Ediacaran and Cambrian Sciences, and Virginia Tech for providing funding for TOF-SIMS and field and museum visits to DEK. SX was supported by NASA grant NNX15AL27G.

References

1. Zhou Z (2014) The Jehol Biota, an Early Cretaceous terrestrial Lagerstätte: new discoveries and implications. *National Science Review* 1(4):543-559.
2. Pan Y, Sha J, & Fuersich FT (2014) A model for organic fossilization of the Early Cretaceous Jehol Lagerstätte based on the taphonomy of "*Ephemeropsis trisetalis*". *Palaios* 29(7):363-377.
3. Muscente AD, *et al.* (2017) Exceptionally preserved fossil assemblages through geologic time and space. *Gondwana Res* 48:164-188.
4. Chang M-M (2011) *The Jehol fossils: the emergence of feathered dinosaurs, beaked birds and flowering plants* (Academic Press).
5. Pan Y, Sha J, Zhou Z, & Fürsich FT (2013) The Jehol Biota: definition and distribution of exceptionally preserved relicts of a continental Early Cretaceous ecosystem. *Cretaceous Research* 44:30-38.
6. Sun G, Dilcher DL, Zheng S, & Zhou Z (1998) In search of the first flower: a Jurassic angiosperm, Archaefructus, from northeast China. *Science* 282(5394):1692-1695.
7. Hou L-h, Zhou Z, Martin LD, & Feduccia A (1995) A beaked bird from the Jurassic of China. *Nature* 377(6550):616.
8. Chinsamy A, Chiappe LM, Marugán-Lobón J, Chunling G, & Fengjiao Z (2013) Gender identification of the Mesozoic bird Confuciusornis sanctus. *Nature Communications* 4:1381.
9. Zhou Z (2006) Evolutionary radiation of the Jehol Biota: chronological and ecological perspectives. *Geological Journal* 41(3-4):377-393.

10. Zhou Z (2006) Adaptive radiation of the Jehol Biota and its evolutionary ecological background. *Originations and radiations-evidences from the Chinese fossil record*, eds Rong J, Fang Z, Zhou Z, Zhan R, Wang X, & YUan X (Science Press, Beijing, China), pp 705-732, 943-945.

11. Li Q, *et al.* (2012) Reconstruction of Microraptor and the evolution of iridescent plumage. *Science* 335(6073):1215-1219.

12. Xu X, Cheng Y, Wang X, & Chang C (2003) Pygostyle-like Structure from *Beipiaosaurus* (Theropoda, Therizinosauroidea) from the Lower Cretaceous Yixian Formation of Liaoning, China. *Acta Geologica Sinica-English Edition* 77(3):294-298.

13. Xu X, Zheng X, & You H (2009) A new feather type in a nonavian theropod and the early evolution of feathers. *Proceedings of the National Academy of Sciences* 106(3):832-834.

14. Wang Y, Dong L, & Evans SE (2010) Jurassic-Cretaceous herpetofaunas from the Jehol associated strata in NE China: evolutionary and ecological implications. *Bulletin of the Chinese Academy of Sciences* 24(2):76-79.

15. Yuan W (2000) A new salamander (Amphibia: Caudata) from the Early Cretaceous Jehol biota. *Vertebrata Pal Asiatica* 38(2):100-103.

16. Wang X & Zhou Z (2006) Pterosaur assemblages of the Jehol Biota and their implication for the Early Cretaceous pterosaur radiation. *Geological Journal* 41(3-4):405-418.

17. Jin F, Zhang J, & Zhou Z (1995) Late Mesozoic fish fauna from western Liaoning, China. *Vertebrata Pal Asiatica* 33(3):169-193.

18. Xu X, Tang Z, & Wang X (1999) A therizinosauroid dinosaur with integumentary structures from China. *Nature* 399(6734):350.

19. Ji Sa, Ji Q, Lü J, & Yuan C (2007) A new giant compsognathid dinosaur with long filamentous integuments from Lower Cretaceous of Northeastern China. *Acta Geologica Sinica* 81(1):8-15.

20. Zhou Z & Wang Y (2010) Vertebrate diversity of the Jehol Biota as compared with other lagerstätten. *Science China Earth Sciences* 53(12):1894-1907.

21. Rogers AF (1924) Mineralogy and petrography of fossil bone. *Bulletin of the Geological Society of America* 35(3):535-556.

22. Schweitzer MH, Wittmeyer JL, Horner JR, & Toporski JK (2005) Soft-tissue vessels and cellular preservation in *Tyrannosaurus rex*. *Science* 307(5717):1952-1955.

23. Schweitzer MH, Wittmeyer JL, & Horner JR (2007) Soft tissue and cellular preservation in vertebrate skeletal elements from the Cretaceous to the present. *Proceedings of the Royal Society B: Biological Sciences* 274(1607):183-197.

24. Schweitzer MH (2011) Soft tissue preservation in terrestrial Mesozoic vertebrates. *Annual review of earth planetary sciences* 39:187-216.

25. Schweitzer MH, Zheng W, Cleland TP, & Bern M (2013) Molecular analyses of dinosaur osteocytes support the presence of endogenous molecules. *Bone* 52(1):414-423.

26. Kaye TG, Gaugler G, & Sawlowicz Z (2008) Dinosaurian soft tissues interpreted as bacterial biofilms. *PLoS One* 3(7):e2808.

27. Poust AW (2014) Description and ontogenetic assessment of a new Jehol microraptorine. (Montana State University-Bozeman, College of Letters & Science).

28. Yao J, Zhang Y, & Tang Z (2002) Small Spheres Preserved in a Therizinosauroid Dinosaur's Blood Vessels from Northeast China. *Acta Scientiarum Naturalium* 38(2) 221-225.

29. O'Connor JK, Wang M, Zheng X-T, Wang X-L, & Zhou Z-H (2014) The histology of two female Early Cretaceous birds. *Vertebrata Pal Asiatica* 52(1):112-128.

30. Moyer AE, *et al.* (2014) Melanosomes or microbes: testing an alternative hypothesis for the origin of microbodies in fossil feathers. *Scientific reports* 4:4233.

31. Colleary C, *et al.* (2015) Chemical, experimental, and morphological evidence for diagenetically altered melanin in exceptionally preserved fossils. *Proceedings of the National Academy of Sciences* 112(41):12592-12597.

32. Lindgren J, *et al.* (2012) Molecular preservation of the pigment melanin in fossil melanosomes. *Nature Communications* 3:824.

33. Wogelius R, *et al.* (2011) Trace metals as biomarkers for eumelanin pigment in the fossil record. *Science* 333(6049):1622-1626.

34. Pan Y, *et al.* (2016) Molecular evidence of keratin and melanosomes in feathers of the Early Cretaceous bird *Eoconfuciusornis*. *Proceedings of the National Academy of Sciences* 113(49):E7900-E7907.

35. Seitz ALL (1907) *Vergleichende studien über den mikroskopischen knochenbau fossiler und rezenter reptilien und dessen bedeutung für das wachstum und umbildung des knochengewebes im allgemein* (E. Karras).

36. Pawlicki R & Nowogrodzka-Zagórska M (1998) Blood vessels and red blood cells preserved in dinosaur bones. *Annals of Anatomy-Anatomischer Anzeiger* 180(1):73-77.

37. Wilby PR (1993) The role of organic matrices in post-mortem phosphatization of soft-tissues. *Kaupia : Darmstädter Beiträge zur Naturgeschichte* 2:99-113.

38. Schweitzer MH, *et al.* (1997) Heme compounds in dinosaur trabecular bone. *Proceedings of the National Academy of Sciences* 94(12):6291-6296.

39. Martill DM & Unwin DM (1997) Small spheres in fossil bones: blood corpuscles or diagenetic products? *Palaeontology* 40:619-624.

40. Schweitzer MH & Horner JR (1999) Intravascular microstructures in trabecular bone tissues of *Tyrannosaurus rex*. *Annales de Paléontologie*, (Elsevier), pp 179-192.

41. Moodie RL (1920) Concerning the fossilization of blood corpuscles. *The American Naturalist* 54(634):460-464.

42. Plet C, *et al.* (2017) Palaeobiology of red and white blood cell-like structures, collagen and cholesterol in an ichthyosaur bone. *Scientific Reports* 7(1):13776.

43. Bertazzo S, *et al.* (2015) Fibres and cellular structures preserved in 75-million–year-old dinosaur specimens. *Nature Communications* 6:7352.

44. Muscente AD, Czaja AD, Riedman LA, & Colleary C (2017) Organic Matter in Fossils. *Earth Science Series*, ed W.M. White S, Cham, SwitzerlandEncyclopedia of Geochemistry), pp 1-5.

45. Isaacs W, Little K, Currey J, & Tarlo L (1963) Collagen and a cellulose-like substance in fossil dentine and bone. *Nature* 197(4863):192.

46. San Antonio JD, *et al.* (2011) Dinosaur peptides suggest mechanisms of protein survival. *PLoS ONE* 6(6):e20381.

47. Cleland TP, Schroeter ER, & Schweitzer MH (2015) Biologically and diagenetically derived peptide modifications in moa collagens. *Proceedings of the Royal Society B: Biological Sciences* 282(1808):20150015.

48. Avci R, *et al.* (2005) Preservation of bone collagen from the late Cretaceous period studied by immunological techniques and atomic force microscopy. *Langmuir* 21(8):3584-3590.

49. Brocks JJ, *et al.* (2017) The rise of algae in Cryogenian oceans and the emergence of animals. *Nature* 548(7669):578-581.

50. Williams K & Smith G (1977) A critical evaluation of the application of amino acid racemization to geochronology and geothermometry. *Origins of life* 8(2):91-144.

51. Hare PE, Fogel ML, Stafford Jr TW, Mitchell AD, & Hoering TC (1991) The isotopic composition of carbon and nitrogen in individual amino acids isolated from modern and fossil proteins. *Journal of Archaeological Science* 18(3):277-292.

52. Schroeder RA & Bada JL (1976) A review of the geochemical applications of the amino acid racemization reaction. *Earth-Science Reviews* 12(4):347-391.

53. Asara JM, Schweitzer MH, Freimark LM, Phillips M, & Cantley LC (2007) Protein sequences from mastodon and *Tyrannosaurus rex* revealed by mass spectrometry. *Science* 316(5822):280-285.

54. Schweitzer MH, *et al.* (2007) Analyses of soft tissue from *Tyrannosaurus rex* suggest the presence of protein. *Science* 316(5822):277-280.

55. Schweitzer MH, *et al.* (2009) Biomolecular characterization and protein sequences of the Campanian hadrosaur *B. canadensis*. *Science* 324(5927):626-631.

56. Schroeter ER, *et al.* (2017) Expansion for the *Brachylophosaurus canadensis* collagen I sequence and additional evidence of the preservation of Cretaceous protein. *Journal of proteome research* 16(2):920-932.

57. Hedges SB, *et al.* (1995) Detecting dinosaur DNA. *Science* 268(5214):1191-1194.

58. Schwarz C, *et al.* (2009) New insights from old bones: DNA preservation and degradation in permafrost preserved mammoth remains. *Nucleic acids research* 37(10):3215-3229.

59. Allentoft ME, *et al.* (2012) The half-life of DNA in bone: measuring decay kinetics in 158 dated fossils. *Proceedings of the Royal Society B: Biological Sciences* 279(1748):4724-4733.

60. Schweitzer MH, Johnson C, Zocco TG, Horner JR, & Starkey JR (1997) Preservation of biomolecules in cancellous bone of *Tyrannosaurus rex*. *Journal of Vertebrate Paleontology* 17(2):349-359.

61. Schweitzer M, Chiappe L, Garrido A, Lowenstein J, & Pincus S (2005) Molecular preservation in Late Cretaceous sauropod dinosaur eggshells. *Proceedings of the Royal Society B: Biological Sciences* 272(1565):775-784.

62. Wang X-L (1998) Stratigraphic sequence and vertebrate-bearing beds of the lower part of the Yixian Formation in Sihetun and neigh-boring area, western Liaoning, China. *Vertebrata Pal Asiatica* 36:81-101.

63. Li J & Batten DJ (2007) Palynological evidence of an Early Cretaceous age for the Yixian Formation at Sihetun, western Liaoning, China. *Cretaceous Research* 28(2):333-338.

64. Wang X, *et al.* (1999) The Sihetun fossil vertebrate assemblage and its geological setting of western Liaoning, China. *Palaeoworld* 11:310-327.

65. He H, *et al.* (2004) Timing of the Jiufotang Formation (Jehol Group) in Liaoning, northeastern China, and its implications. *Geophysical Research Letters* 31(12).

66. Liu Y-Q, *et al.* (2012) Timing of the earliest known feathered dinosaurs and transitional pterosaurs older than the Jehol Biota. *Palaeogeography, Palaeoclimatology, Palaeoecology* 323:1-12.

67. Yang W, Li S, & Jiang B (2007) New evidence for Cretaceous age of the feathered dinosaurs of Liaoning: zircon U-Pb SHRIMP dating of the Yixian Formation in Sihetun, northeast China. *Cretaceous Research* 28(2):177-182.

68. Swisher III CC, Wang Y-q, Wang X-l, Xu X, & Wang Y (1999) Cretaceous age for the feathered dinosaurs of Liaoning, China. *Nature* 400(6739):58.

69. Swisher C, *et al.* (2002) Further support for a Cretaceous age for the feathered-dinosaur beds of Liaoning, China: New 40 Ar÷ 39 Ar dating of the Yixian and Tuchengzi Formations. *Chinese Science Bulletin* 47(2):136-139.

70. Pflug HD & Heinz B (1997) Analysis of fossil organic nanostructures: terrestrial and extraterrestrial. *Instruments, Methods, and Missions for the Investigation of Extraterrestrial Microorganisms*, (International Society for Optics and Photonics), pp 86-98.

71. Winkler W, Kirchner EC, Asenbaum A, & Musso M (2001) A Raman spectroscopic approach to the maturation process of fossil resins. *Journal of Raman spectroscopy* 32(1):59-63.

72. Brody RH, Edwards HG, & Pollard AM (2001) A study of amber and copal samples using FT-Raman spectroscopy. *Spectrochimica Acta Part A: Molecular Biomolecular Spectroscopy* 57(6):1325-1338.

73. Schopf JW, Kudryavtsev AB, Agresti DG, Wdowiak TJ, & Czaja AD (2002) Laser–Raman imagery of Earth's earliest fossils. *Nature* 416(6876):73.

74. Bernard S, *et al.* (2007) Exceptional preservation of fossil plant spores in high-pressure metamorphic rocks. *Earth and Planetary Science Letters* 262(1-2):257-272.

75. Jehlička J, Jorge Villar S, & Edwards H (2004) Fourier transform Raman spectra of Czech and Moravian fossil resins from freshwater sediments. *Journal of Raman Spectroscopy* 35(8-9):761-767.

76. Witke K, Götze J, Rößler R, Dietrich D, & Marx G (2004) Raman and cathodoluminescence spectroscopic investigations on Permian fossil wood from Chemnitz—a contribution to the study of the permineralisation process. *Spectrochimica Acta Part A: Molecular Biomolecular Spectroscopy* 60(12):2903-2912.

77. Thomas DB, Fordyce RE, Frew RD, & Gordon KC (2007) A rapid, non-destructive method of detecting diagenetic alteration in fossil bone using Raman spectroscopy. *Journal of Raman Spectroscopy* 38(12):1533-1537.

78. Thomas DB, McGoverin CM, Fordyce RE, Frew RD, & Gordon KC (2011) Raman spectroscopy of fossil bioapatite — A proxy for diagenetic alteration of the oxygen isotope composition. *Palaeogeography, Palaeoclimatology, Palaeoecology* 310(1):62-70.

79. Thomas DB, Nascimbene PC, Dove CJ, Grimaldi DA, & James HF (2014) Seeking carotenoid pigments in amber-preserved fossil feathers. *Scientific Reports* 4:5226.

80. Vogt H, Chattopadhyay T, & Stolz H (1983) Complete first-order Raman spectra of the pyrite structure compounds FeS2, MnS2 and SiP2. *Journal of physics and chemistry of solids* 44(9):869-873.

81. De Faria D, Venâncio Silva S, & De Oliveira M (1997) Raman microspectroscopy of some iron oxides and oxyhydroxides. *Journal of Raman spectroscopy* 28(11):873-878.

82. Henss A, *et al.* (2013) Applicability of ToF-SIMS for monitoring compositional changes in bone in a long-term animal model. *Journal of The Royal Society Interface* 10(86):20130332.

83. Thiel V & Sjövall P (2014) Time-of-flight secondary ion mass spectrometry (TOF-SIMS): Principles and practice in the biogeosciences. *Analytical Techniques in Geosciences* 4:122.

84. Puech P-F, Dhamelincourt P, Taieb M, & Serratrice C (1986) Laser Raman microanalysis of fossil tooth enamel. *Journal of Human Evolution* 15(1):13-19.

85. Morris MD & Mandair GS (2011) Raman assessment of bone quality. *Clinical Orthopaedics Related Research*® 469(8):2160-2169.

86. Lee Y-C, *et al.* (2017) Evidence of preserved collagen in an Early Jurassic sauropodomorph dinosaur revealed by synchrotron FTIR microspectroscopy. *Nature communications* 8:14220.

87. Wang Y & Yang Q (2007) Raman Spectra of Different Done Part of Fossils Dinosaurs. *The Journal of Light Scattering* 2.

88. Sawlowicz Z (1993) Pyrite framboids and their development: a new conceptual mechanism. *Geologische Rundschau* 82(1):148-156.

89. Folk RL (2005) Nannobacteria and the formation of framboidal pyrite: Textural evidence. *Journal of Earth System Science* 114(3):369-374.

90. Popa R, Kinkle BK, & Badescu A (2004) Pyrite framboids as biomarkers for iron-sulfur systems. *Geomicrobiology Journal* 21(3):193-206.

Figures

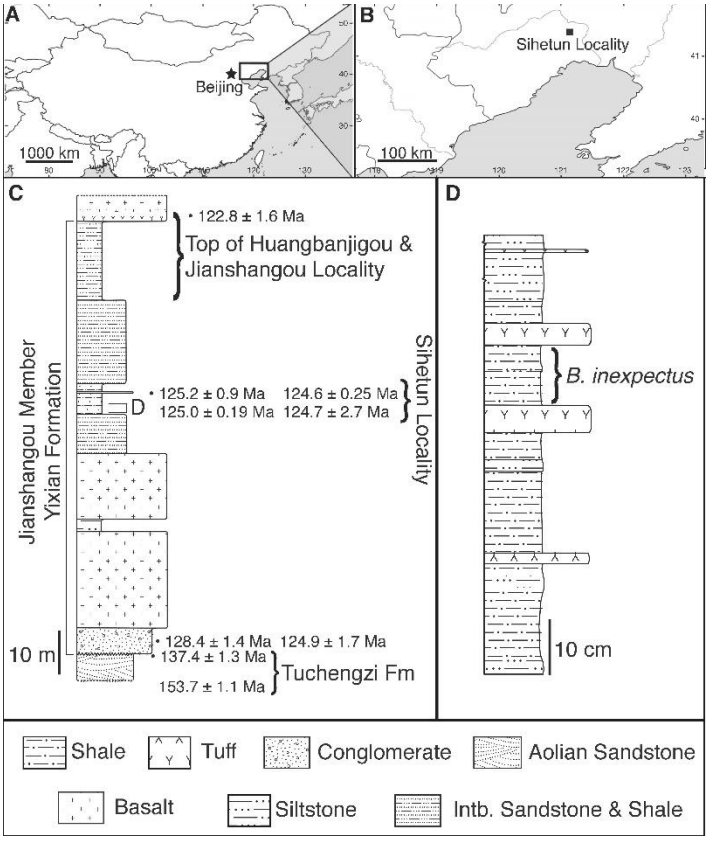

Figure 1. Geographic and stratigraphic setting. **A**: Map of China with panel denoting the area enlarged in (B). **B**: The Sihetun locality in Liaoning Province. Boundaries with the Hebei Province to the west and Inner Mongolia to the north shown in black. **C**: Combined stratigraphic column of the Jianshangou Member of the lowermost Yixian Formation bounded by an unconformity with the Tuchengzi Formation below and volcanics above. The bracketed strata correspond to the column in D. See Wang et al. 1998 for details on igneous rocks (62). **D**: Stratigraphic column of the lower Yixian Formation at Sihetun, showing the stratigraphic horizon of *Beipiaosaurus inexpectus*. Beds at the top of this column (dominated by blocky siltstones) top the modern exposure and are eroded to various thicknesses. They are abbreviated in this column. This section is approximately 15 meters from the original collection site of

Beipiaosaurus inexpectus, now covered by new construction. Tuff thicknesses vary laterally. Basaltic layers are present about 150 meters away from this exposure, in an exposure about 10 meters up-section from the fossil bed.

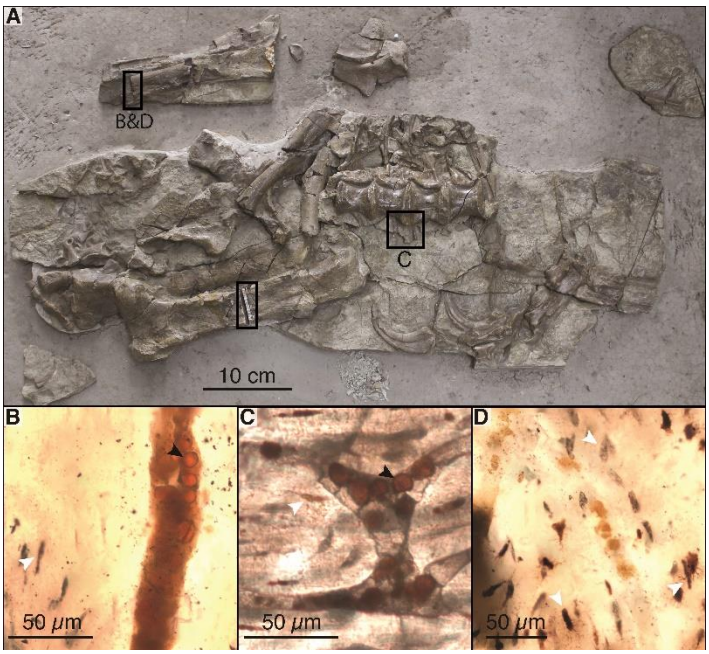

Figure 2. Sampled specimen and histology. **A**: Initially published half of IVPP V11559, with sampled areas marked. In this study, we used gastralia from associated fragments (sample area C) stored with thin sections from Yao et al. (2002, sample areas B & D). **B**: Spheres as observed in Yao et al. (2002) along with non-spherical vessel fill in thin section LJ98B1 provided by Dr. Jinxian Yao. **C**: Spheres in an anastomosing vessel in thin section VTL2, newly prepared at Virginia Tech. **D**: Small grainy fill in a vessel in thin section LJ98B1. **B-D:** Black arrows indicate spheres and white arrows indicate lacunae, both filled and unfilled.

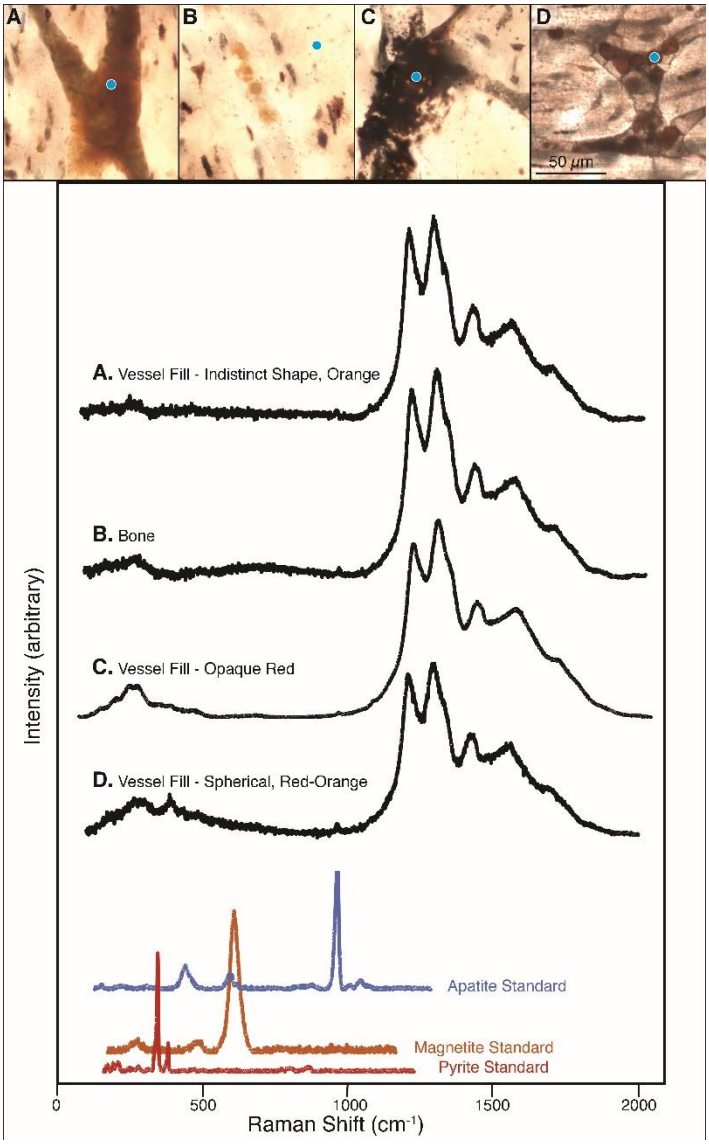

Figure 3. Raman spectra collected from VTL1-5. **A-D**: Examples of the sample locations represented in the spectra below, with circles (at approximate size of sample area) marking targeted locations. **Below**: Spectra corresponding to the targeted areas in our samples. At the bottom are three standard spectra for minerals hypothesized to be present in parts of the thin sections. Apatite is apparent throughout, whereas the iron bearing minerals are not, though there may be some peaks obscured in the low wave numbers.

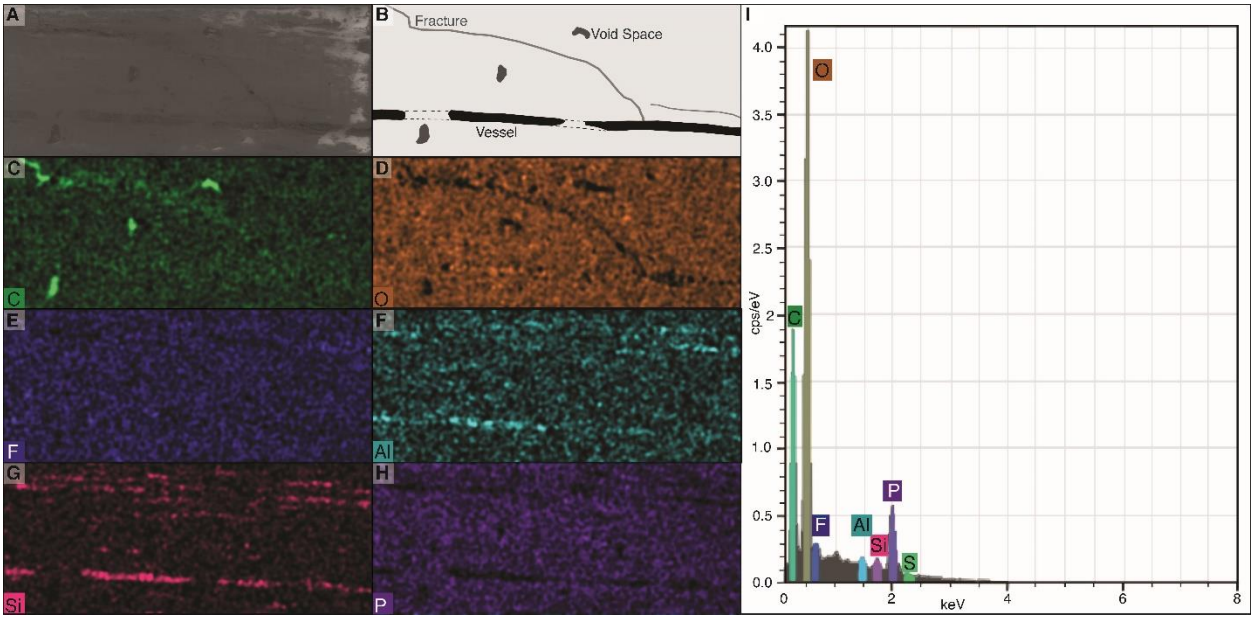

Figure 4. Energy Dispersive X-ray Spectroscopy (EDS/EDX) data from an area of the thin section VTL2 where a vessel is exposed at the surface. **A**: Scanning electron micrograph of the area sampled with EDS. **B**: Drawing of the sampled area emphasizing the locations of the exposed vessel, fractures, and void spaces. The vessel either passes into the depth of the thin section or passed through bone removed by sectioning. These non-exposed lengths are indicated by dashed lines. **C-H**: EDS elemental maps (bottom left). Relative abundance of an element is indicated by color brightness. **I**: Spectrum of elements present across the whole scanned area.

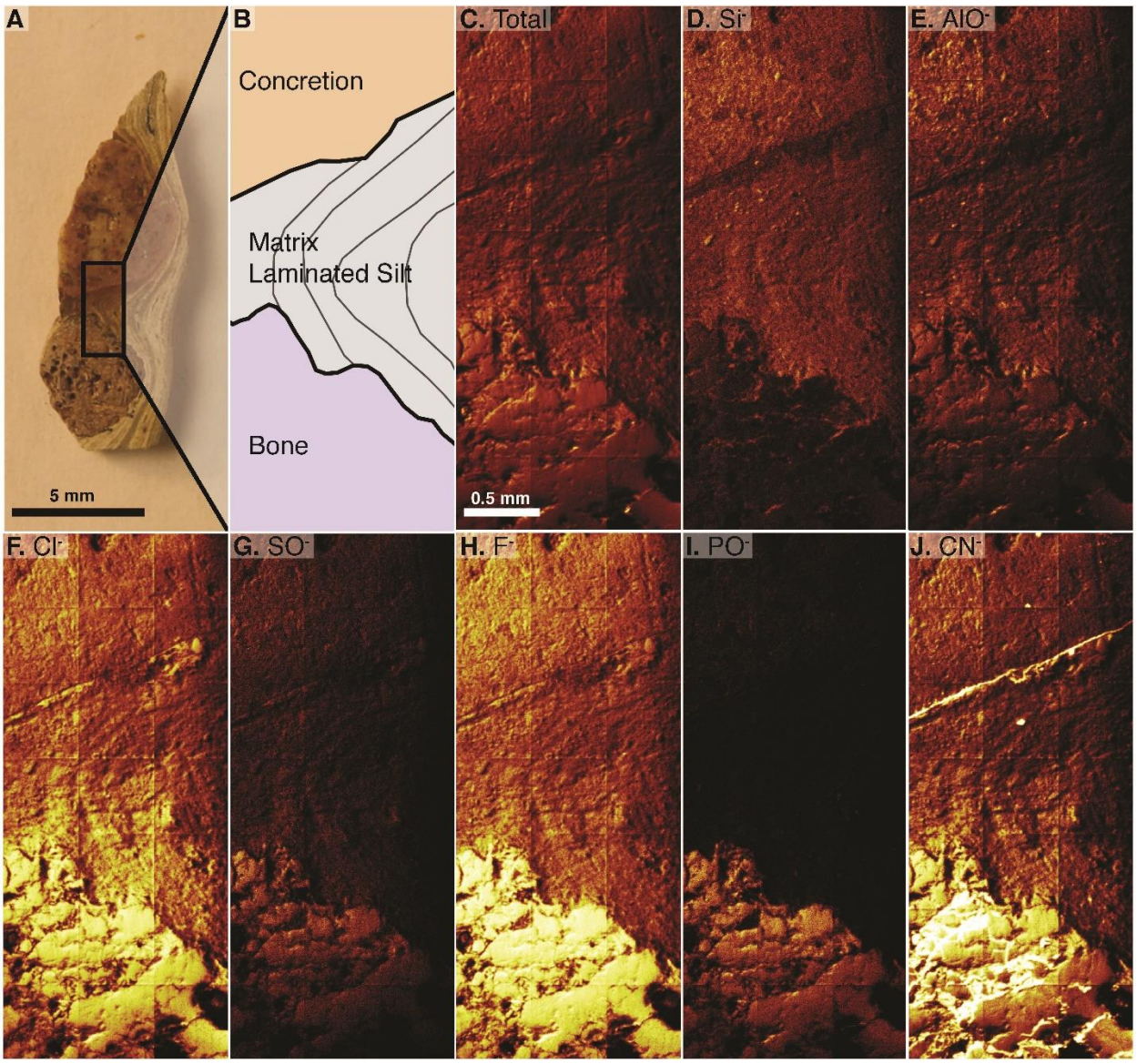

Figure 5. Time of Flight Secondary Ion Mass Spectrometry (TOF-SIMS) maps of an *in situ* bone fragment and the surrounding matrix. **A**: Cut fragment with cross section of a gastralium, fine lamination in surrounding shale, and an orange-tinted concretion. Scanned area indicated by rectangle. **B**: Drawing of the scanned area emphasizing borders between bone, sedimentary matrix, and concretion. **C**: TOF-SIMS map of total chemical species, each a collage of 21 half-millimeter squares. **D**–**J**: TOF-SIMS maps of species of interest, representing a subset of the total collected species. Additional species maps and spectral data are available in the appendices.

Tables

Section Name	Element	Position	Sectioned by	Orientation
VT-X1 2018	Gastralia	near broken end of ~2 cm fragment	DEK	Cross Section
VT-X2 2018	Gastralia	serial section from VT-X1, farther from break	DEK	Cross Section
VT-L1 2018	Gastralia	exterior	DEK	Longitudinal
VT-L2 2018	Gastralia	interior, serial section with VT-L1-5	DEK	Longitudinal
VT-L3 2018	Gastralia	interior, serial section with VT-L1-5	DEK	Longitudinal
VT-L4 2018	Gastralia	interior, serial section with VT-L1-5	DEK	Longitudinal
VT-L5 2018	Gastralia	exterior, serial section with VT-L1-5	DEK	Longitudinal
HO-9601	Humerus	unknown	JY	Longitudinal
HO-9602	Humerus	shaft	JY	Cross Section
LJ98B-1	Humerus	unknown	JY	Longitudinal
LJ98B-4	Humerus	shaft	JY	Cross Section

Table 1. Thin sections used in this study. Materials for new thin sections were provided by Jinxian Yao along with her original thin sections.

Appendices

Appendix A: Histology

Table characterizing features throughout thin sections made for this study (VTX1 & VTX2, VTL1 – VTL5) followed by exemplar images of textures and colors under microscope. All coordinates on Olympus objective microscope with labels on observer's right-hand side.

Appendix Table 1. Cross sectional thin sections from an associated *B. inexpectus* gastralium.

Thin Section #	Coordinates	O-cytes?	Osteocyte shape	Distribution
VT-X1 2018	15.4,97.3	y		
VT-X1 2018	15.8,98.2	y		
VT-X1 2018	15.8,99.3	y	elliptical and round	internal
VT-X1 2018	15.6,100.4	y	elliptical and round	internal
VT-X1 2018	15.4,100.9	y	elliptical and round	whole visible
VT-X1 2018	15.0, 97.6	y	round	whole visible
VT-X1 2018	15.3, 98.7	y	round and elongate	whole visible
VT-X1 2018	15.2, 99.5	y	round	whole visible
VT-X1 2018	14.9, 100.6	y	round	internal
VT-X2 2018	11.7, 92.1	y	round	internal
VT-X2 2018	11.4, 93.2	Y	Round	Internal
VT-X2 2018	11.5, 94.3	y	round and elongate	internal
VT-X2 2018	11.4, 95.4	y	round and elongate	internal
VT-X2 2018	11.1, 91.8	y	round	random
VT-X2 2018	10.9, 92.8	y	round	random
VT-X2 2018	10.9, 94.0	y	round and elongate	random
VT-X2 2018	11.0, 95.1	y	round	random
VT-X2 2018	11.1, 96.1	N		

Orientation	Osteocyte Density	Length	Width	Additional notes
random	~100 in field of view	5-10 um	5-7 um	
NW-SE	~75 in field of view	5-10 um	5-7 um	
NW-SE	~100 in field of view	5-10 um	5-7 um	
slight NE-SW	~100 in field of view	5 um	5 um	
random	~100 in field of view	5-12 um	5 um	
random	~100 in field of view	5 um	5 um	
NW-SE	~75 in field of view	5 um	5-7 um	
random	~75 in field of view	5 um	5 um	dubious rust-colored rounds
random	~75 in field of view	5 um	5 um	slide difficult to view above 20x- approx. measures
NE-SW	~100 in field of view	5-15 um	3-5 um	edge of slide, only 80% of view bone
NE-SW	~75 in field of view	5-10 um	3-5 um	sig overlap with 15.4,97.3
random	~50 in field of view	5 um	5 um	very fractured at edge
random	~50 in field of view	5 um	5 um	fractured edges to bottom and right of field of view
slight E-W	~75 in field of view	5-10 um	5 um	
slight NE-SW	~75 in field of view	5-7 um	3-5 um	highly fractured, overlap with 11.7, 92.1
				very fractured far corner of slide

Appendix Table 2. VT-L1 2018. Longitudinal thin section from associated *B. inexpectus* gastralia.

Location on Slide	**Spheres?**	**Location**	**Size**	**Shape**	**Color**
13.1, 88.9	n				
13.0, 89.6	y	vessels	8-12 um	sphere	red-orange
13.0, 90.9	y	vessel confluence	8-10 um	sphere	red-orange
13.0, 92.0	y	vessels	6-10 um	sphere and dubious round	red-orange
13.0, 92.9	y	vessels	10-12 um	round & dubious	red-orange
13.0, 93.8	y	vessel	10-13 um	oval & round	red-orange
13.0, 94.8	y	vessel	8-10 um	sphere	red-orange
12.9, 95.6	d	vessel	na	indistinct	red-orange
12.9, 96.5	n				
13.0, 97.6	n				
11.9, 89.0	n				
11.9, 90.1	n				
11.9, 91.3	n				
11.8, 92.5	n				
11.8, 93.8	n				

Other Vessel Fill	Raman Data (514 nm)	Additional notes
translucent yellow and orange		
opaque and translucent yellow	spectrum taken, pos1&2	too thin
opaque, dark red specks, translucent red-orange	spectra taken pos 3 in confluence	?osteocytes very poor, excellent vessels
translucent red-orange & grey, opaque, red specks	spectra taken pos5	excellent confluence of 5 vessels
translucent orange and grey, red specks		
translucent orange and grey, red specks		narrower part of section
opaque and translucent red-orange		narrower part of section
translucent red-orange		narrower part of section
none		too thin, narrow end of section
none		too thin
translucent red-orange & grey		too thin
none		too thin
red specks		too thin
red and black specks		too thin

Appendix Table 3. VT-L2 2018. Longitudinal thin section from associated *B. inexpectus* gastralia.

Location on Slide	**Spheres?**	**Location**	**Size**	**Shape**	**Color**
12.9, 93.0	n				
12.9, 94.1	y	vessels	8-15 um		
12.9, 95.0	d	vessels	8-10 um	sphere & round	red-orange
12.9, 96.1	n			indistinct	red-orange
12.9, 97.2	n				
12.9, 98.3	n				
12.9, 99.4	d	vessels	8 um	indistinct&round	red-orange
13.0, 100.5	y	vessels	6-15 um	round, indistinct, & sphere	red-orange
13.1, 101.5	y	vessels	8-10 um	round	red-orange
13.1, 102.5	n				
11.8, 93.1	n				
11.9, 94.2	d	vessel	8-10 um	indistinct	orange
11.9. 95.3	n				
11.9, 96.4	n				
11.9, 97.5	n				
11.9, 98.2	n				

Other Vessel Fill	Raman Data (514 nm)	Additional notes
translucent red-orange		
translucent red-orange	spectra taken, pos1	
red specks & translucent red-orange	spectra taken pos 2	thin
translucent orange		
nearly opaque red, translucent red-orange, red specks		
translucent grey & orange, red specks		
opaque and grey		
grey		
translucent grey & red-orange		
opaque specks		
none		
translucent grey, red specks		thin
opaque, translucent grey		
translucent grey		orange splotchy stains
opaque and near opaque red		
near opaque red, red specks		

Appendix Table 4. VT-L3 2018. Longitudinal thin section from associated *B. inexpectus* gastralia.

Location on Slide	Spheres?	Location	Size	Shape	Color
15.7, 92.5	n				
15.7, 93.3	n				
15.7, 94.2	y	vessel	10-15 um	indistinct	red-orange
15.4, 95.1	y	vessels	7-13 um	spheres and indistinct	orange and red-orange
15.3, 96.1	y	vessels	8-10 um	spheres	red-orange
15.2, 97.0	y	vessel	10-15 um	spheres	red-orange
14.8, 92.4	y	vessels	10-12 um	spheres and indistinct	red-orange
14.8, 93.3	y	vessels	8-16 um	spheres and elongate	red-orange
14.8, 94.3	y	vessels	10-11 um	spheres	red-orange
14.8, 95.3	y	vessels	8-10 um	indistinct to round	red-orange
14.8, 96.0	y	vessels	5-11 um	spheres to conglomerated round	red-orange & orange
14.9, 96.8	d	vessels		indistinct	red-orange
14.9, 97.6	N				

Other Vessel Fill	Raman Data (514 nm)	Additional notes
none		
5 um red specks and dark translucent red fill, & some translucent orange		red specks outside vessels
translucent grey & dark opaque grainy		red specks outside vessels
translucent grey & orange, red specks		red specks outside vessels
opaque, translucent dark red, red specks	spectrum taken pos 1 &4	red specks outside vessels
translucent red-orange, opaque, opaque specks	spectra taken red specks	red specks outside vessels
translucent orange, translucent grey, opaque	spectra taken red specks pos 2	brown-orange stains
opaque grey, translucent orange	spectra taken pos 3	thin & fragmented edge, elongate greyish specks across area
dark red to opaque, translucent orange		
opaque, translucent grey & orange		
translucent orange & red specks	spectra taken, pos5-6	
opaque grey & red specks		
translucent grey & orange		very edge of slide

Appendix Table 5. VT-L4 2018. Longitudinal thin section from associated *B. inexpectus* gastralia.

Location on Slide	Spheres?	Location	Size	Shape
12.4, 88.9	n			
12.5, 89.9	n			
12.4, 90.8	n			
12.2, 92.0	y	vessels & unclear fractured areas	6-12 um	round, lumpy, & indistinct
12.2, 92.9	y	vessels	8-15 um	round & blocky
12.2, 94.0	y	vessels	6-9 um	round
12.6, 94.5	n			

Color	Other Vessel Fill	Raman Data (514 nm)	Additional notes
	none		
	translucent orange & grey, red specks		
orange	translucent orange & red specks		
orange and red-orange	translucent orange & red specks	spectra taken pos 1	reddish dots and smudges
orange	red specks	spectra taken pos 5	narrow fractured section
	translucent orange & red specks		far edge of slide. Only one pass along length due to small width

Appendix Table 6. VT-L5 2018. Longitudinal thin section from associated *B. inexpectus* gastralia.

Location	**Spheres?**	**Location**	**Size**	**Shape**	**Color**
13.9, 88.0	n				
13.5, 89.0	d	vessels		vessels & unclear near vessel area	
13.3, 90.0	y	vessel	8-11 um	lumpy	
13.3, 91.0	d	vessels	6-8 um	round & indistinct	orange and red-orange
13.4, 92.2	d	vessels	8 um	indistinct	orange
13.4, 93.1	y	vessels & unclear areas	8-12 um	round	orange
13.3, 94.1	d	vessels	6-11 um	indistinct, blocky, and round	red-orange
13.3, 95.3	y	vessel	12 um	sphere	orange and red-orange
13.3, 96.2	n				red-orange
12.5, 89.8	n				orange
12.5, 90.8	n				
12.5, 91.9	n				
12.5, 92.8	n				
12.5, 94.0	y	vessels	9-13 um	spheres	orange and red-orange
12.5, 95.2	y	vessel	8-11 um	spheres	red-orange
12.5, 95.8	n				
11.8, 90.6	n				
11.8, 91.6	n				
11.8, 92.7	n				
11.8, 93.8	n				
11.8, 94.9	n				
11.8, 96.0	n				

Other Vessel Fill	Additional notes
red specks	
red specks & opaque reddish round & translucent orange	
opaque reddish rounds and opaque grey	
opaque grey & translucent orange	
red specks and rusty fill	
translucent orange, red specks	
dark red, translucent orange, and translucent orange specks	
dark red & translucent orange	red blurry stain on spur of slide
translucent orange & opaque	linear fracture in middle of this field of view
red specks and dark transluncent reddish	vessels somewhat unclear, big fracture on right side in field of view
dark opaque and red specks	fracture on left and big bubble
translucent orangey-red specks	far edge, another bubble
translucent orange & red specks	edge
translucent orange, opaque rounds	some spheres have darker middles and lighter outsides. Replacement?
red specks	
dark & translucent red-orange	edge
none	partially filled field of view, along bottom edge. Many red specks
none	""
translucent orange specks	""
none	"" + a bubble
none	""
none	bottom corner

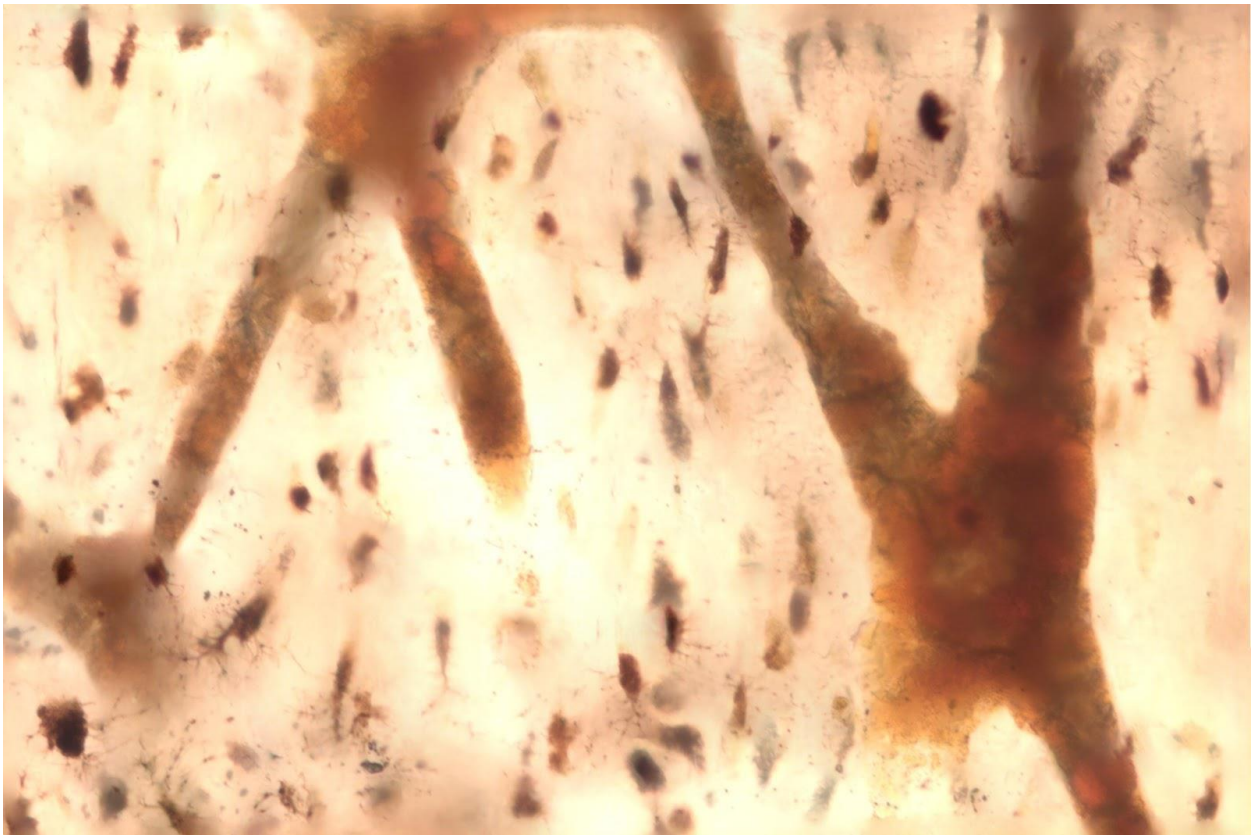

LJ98B_1 (40x)

- Filled Lacunae with Canaliculi
- Orange Fill
- Red-orange Fill
- Blocky and Indistinct Texture
- Anastomosing vessels
- Grey Fill

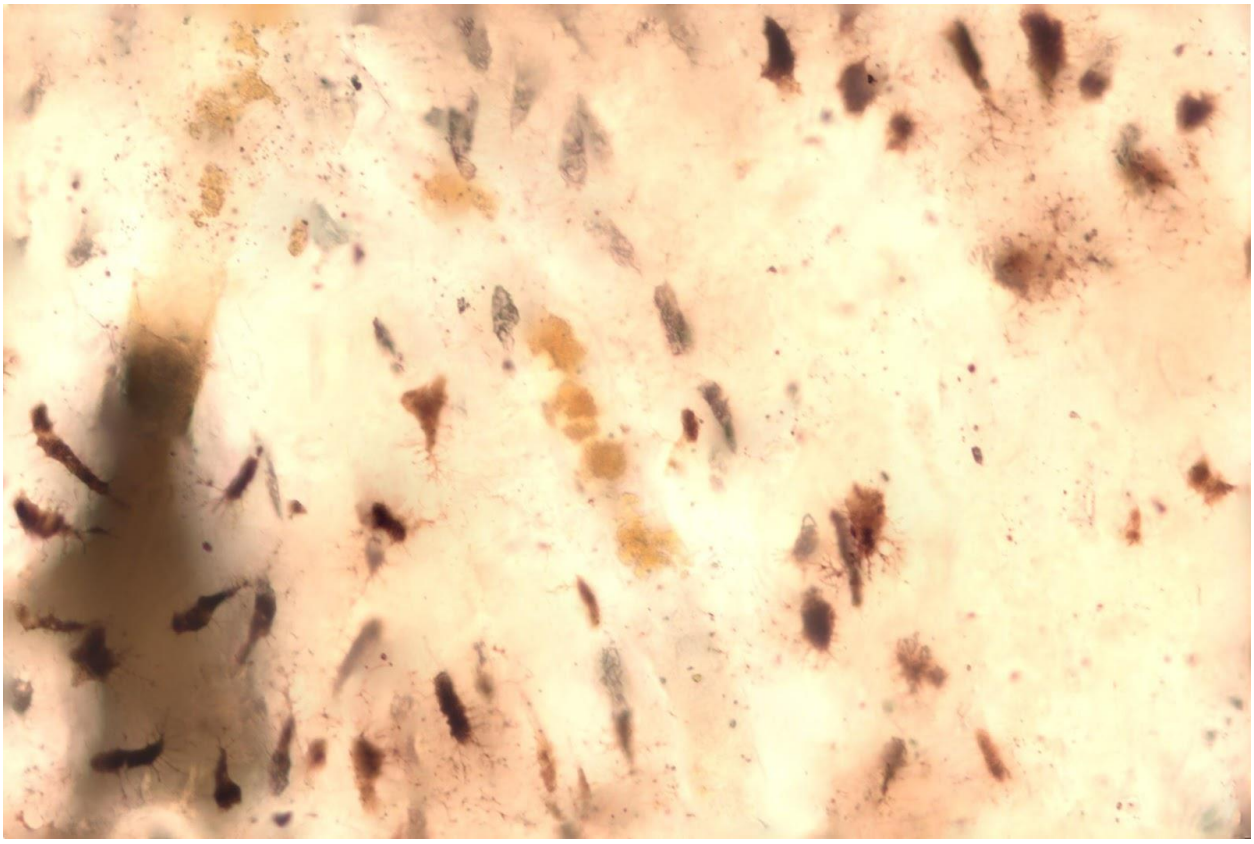

LJ98B_1 (40x)

- Small Rounds (orange)
- Unfilled Vessels
- Grey Fill
- Unfilled Lacunae with canaliculi
- Filled Lacunae with canaliculi (grey and opaque)
- Yellow Fill
- Small Red Specks

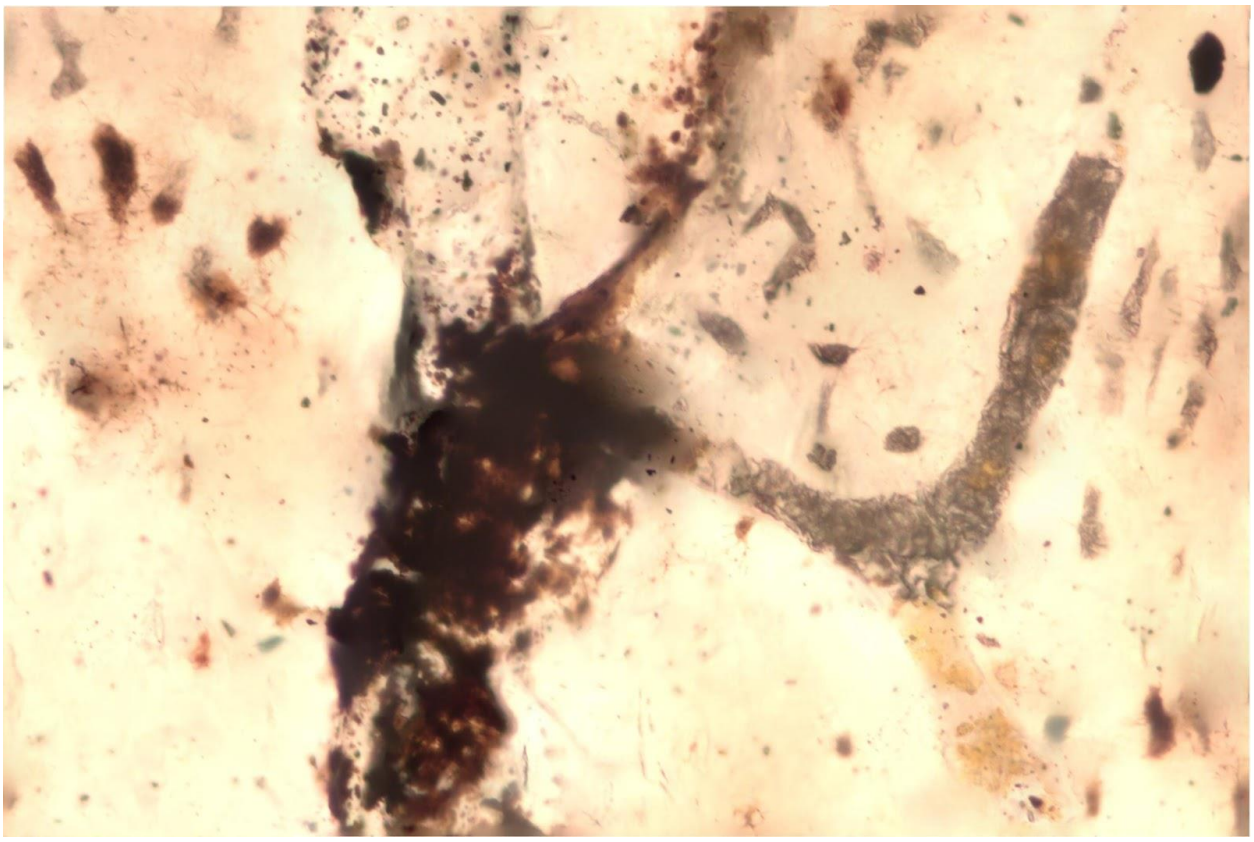

LJ98B_1 (40x)

- Red Specks
- Opaque red fill
- Black fill
- Grey Fill
- Yellow Fill
- Small Rounds
- Filled Lacunae with Canaliculi

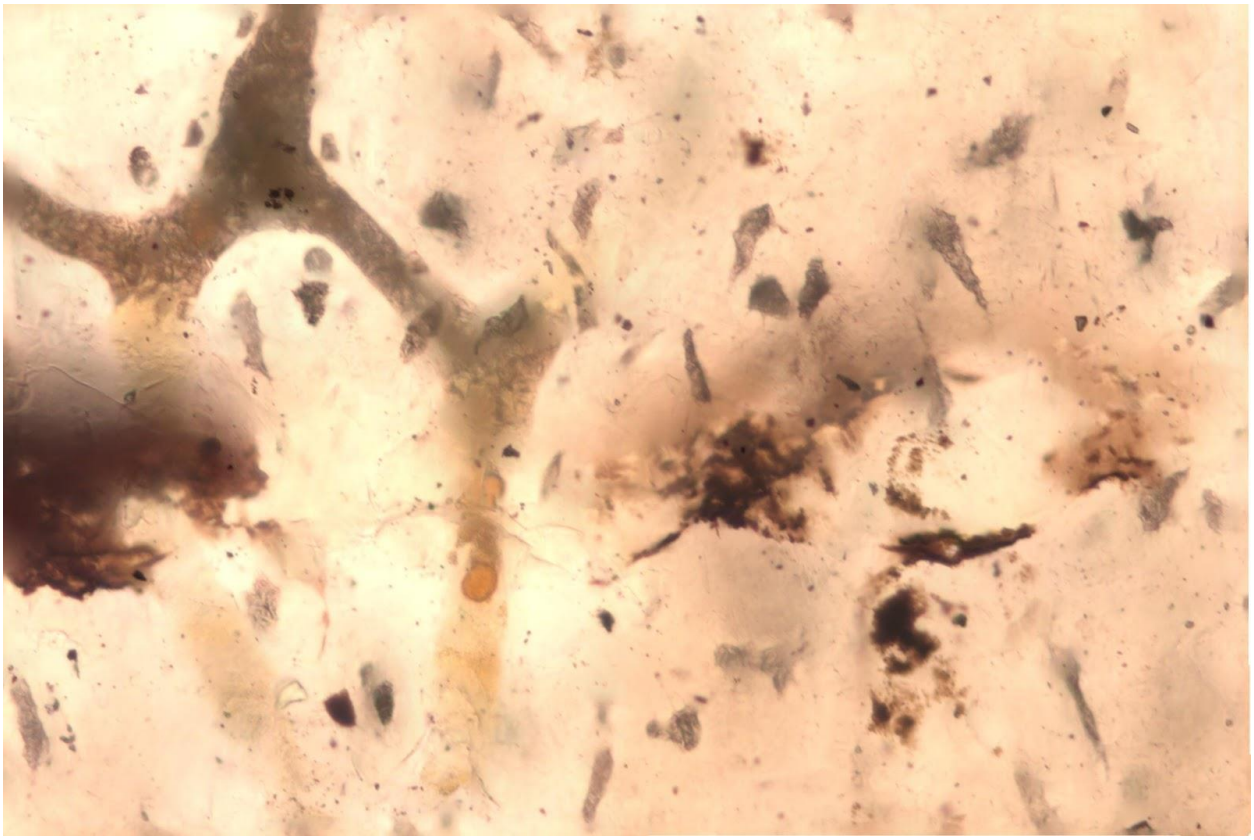

LJ98B_1 (40x)

- Orange Sphere
- Round orange
- Grey Vessel Fill
- Unfilled Lacunae with Canaliculi
- Yellow Vessel Fill

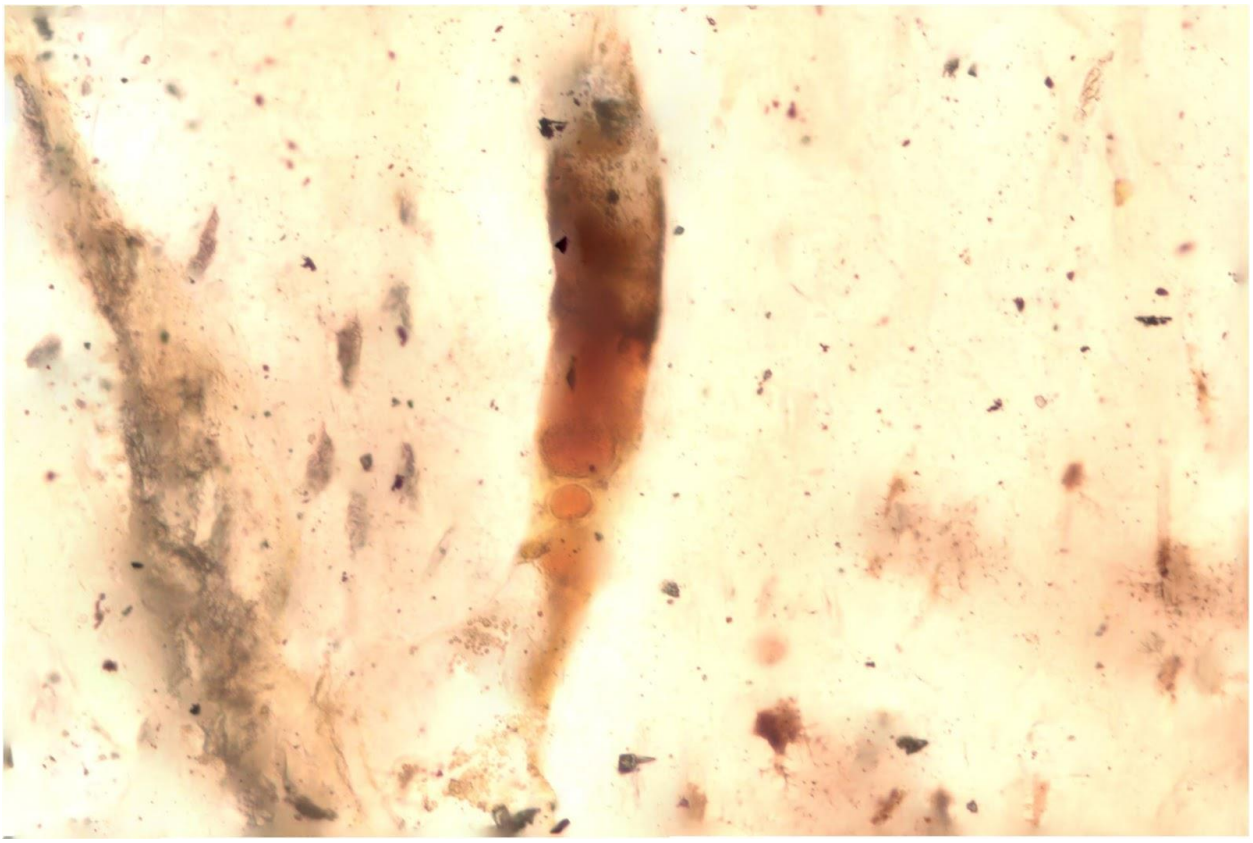

LJ98B_1 (40x)

- Red-orange Sphere
- Textured Sphere
- Abnormally Large Sphere
- Red-orange Vessel Fill
- Indistinct texture vessel fill
- Grey Fill in Fractured Vessel
- Filled and Unfilled Lacunae with Canaliculi

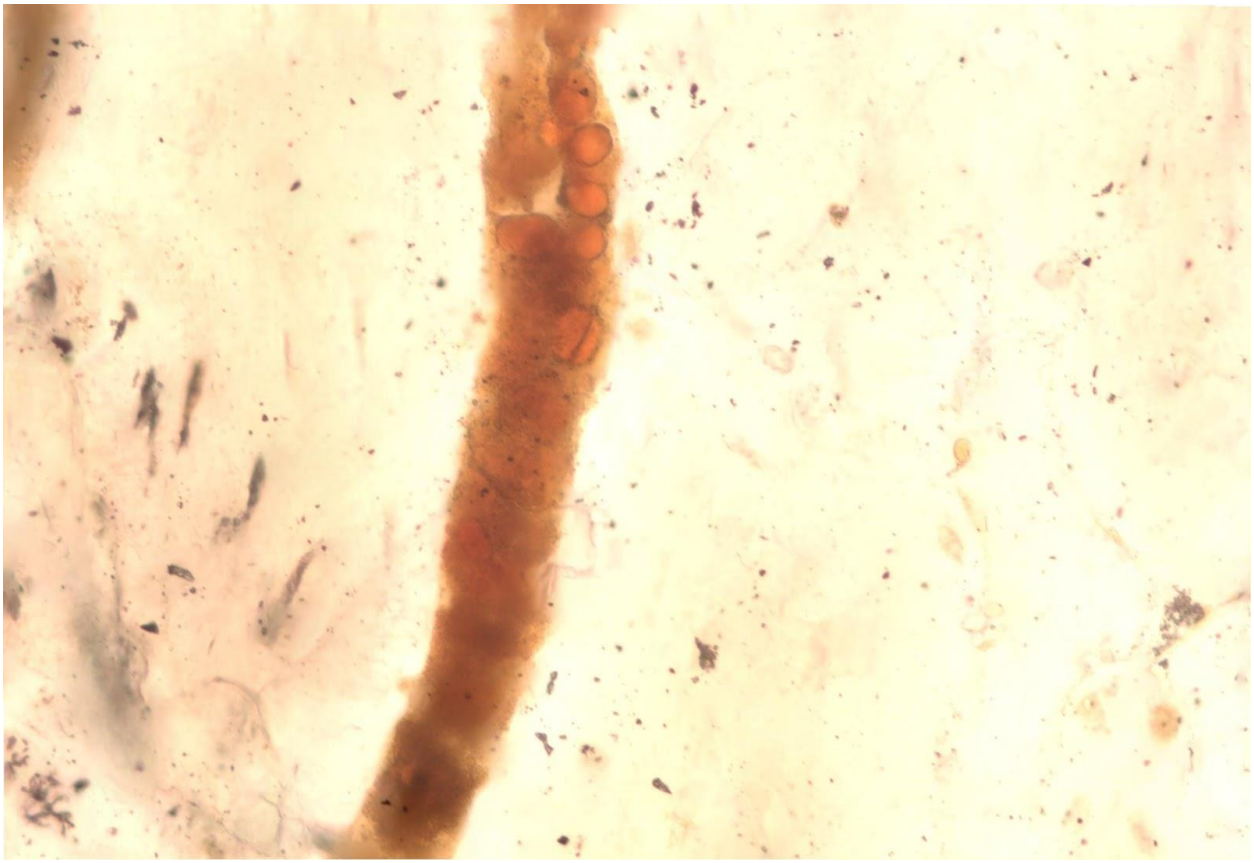

LJ98B_1 (40x)

- Red-orange Rounds
- Red-orange Vessel Fill
- Textured Spheres
- Red-orange Spheres

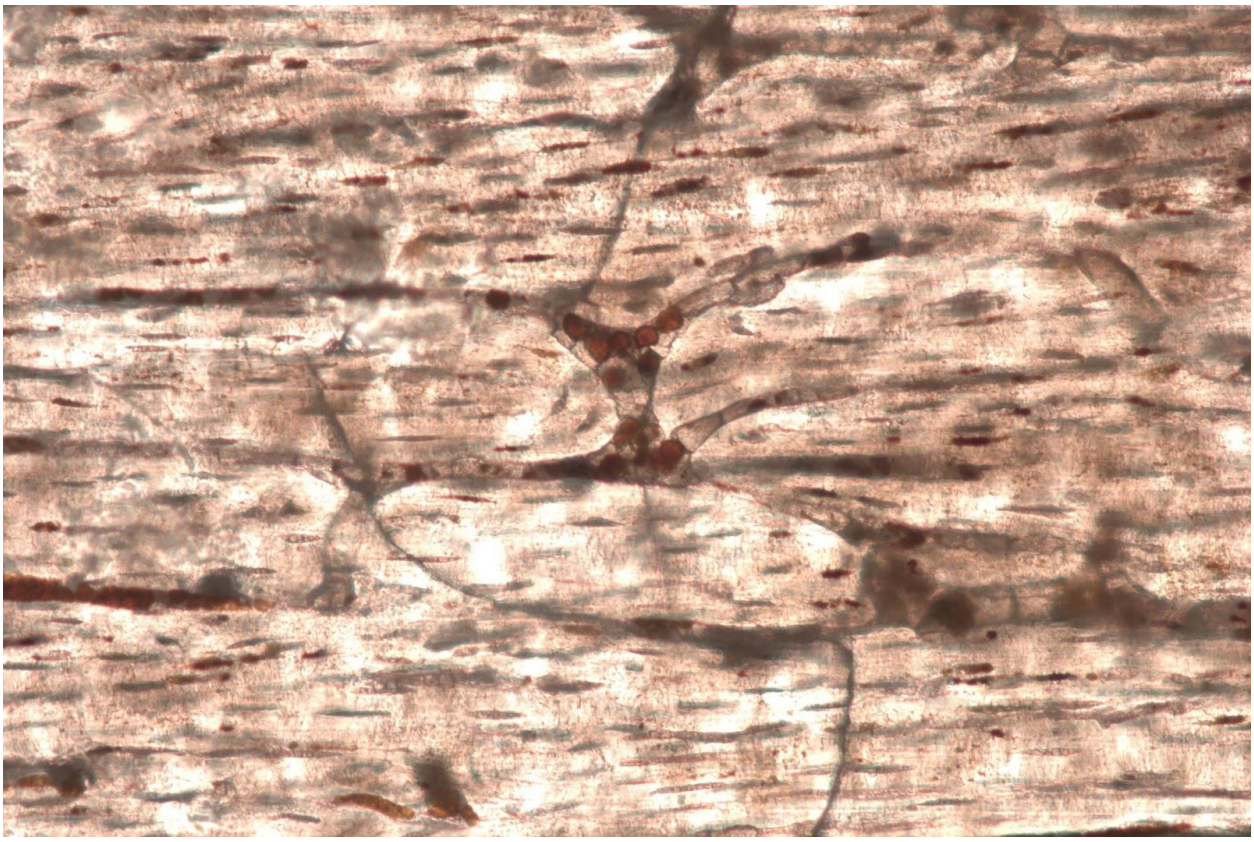

VTL2 (20x)

- Red-orange Spheres
- Round Vessel Fill
- Red-orange Lacunae fill
- Red Specks
- Grey Vessel Fill
- Unfilled Vessels
- Blocky Vessel Fill
- Anastomosing Vessels

- Well sampled with Raman Spectroscopy

Appendix B: Field Photos – Sihetun Locality

Grainy Tuff. Layers of tuff varied laterally in how concreted they were, with the grainiest tuffs generally having the darkest orange color. Up-section of Figure 1, panel D. Jianshangou Member, Yixian Formation, Sihetun Locality, Liaoning Province, China.

Finely Laminated Shale. Characteristic of large portions of the Yixian at Sihetun. Often interbedded with blockier silty shales. Hand sample fallen from section represented in Figure 1, panel D. Jianshangou Member, Yixian Formation, Sihetun Locality, Liaoning Province, China.

Hand sample of basalt at the opposite side of the museum from where *B. inexpectus* was collected, about 10m upsection. Jianshangou Member, Yixian Formation, Sihetun Locality, Liaoning Province, China.

Basaltic layer about 10m up-section from *B. inexpectus* bearing strata and at opposite side of the Sihetun locality. Chunchi Liao for scale. Jianshangou Member, Yixian Formation, Sihetun Locality, Liaoning Province, China. Igneous rocks left out of our stratigraphic column are represented in Wang et al., 1998.

Rutile in hand sample found nearby current exposure of *B. inexpectus* bearing strata. Likely from a thin bed of shale interbedded with blockier silty shale up-section. Jianshangou Member, Yixian Formation, Sihetun Locality, Liaoning Province, China.

Current exposure of *B. inexpectus* bearing strata, between the two thicker orange beds. This section was the basis for the stratigraphic column in Figure 1, panel D. Top of exposure is not far above top of frame. Rock hammer for scale. Jianshangou Member, Yixian Formation, Sihetun Locality, Liaoning Province, China.

Closeup of *B. inexpectus* layer (bounded by the two orange layers). Jianshangou Member, Yixian Formation, Sihetun Locality, Liaoning Province, China. Shown in Figure 1, Panel D.

Closeup of *B. inexpectus* layer (bounded by the two orange layers). Jianshangou Member, Yixian Formation, Sihetun Locality, Liaoning Province, China. Shown in Figure 1, Panel D.

Nearer the exact site where *B. inexpectus* was collected (from Layer 15). Will ultimately be the wall of the museum under construction. Jianshangou Member, Yixian Formation, Sihetun Locality, Liaoning Province, China. Shown in Figure 1, Panel D.

Appendix C: Raman Data

Supplementary excel file

Appendix D: EDS Data.

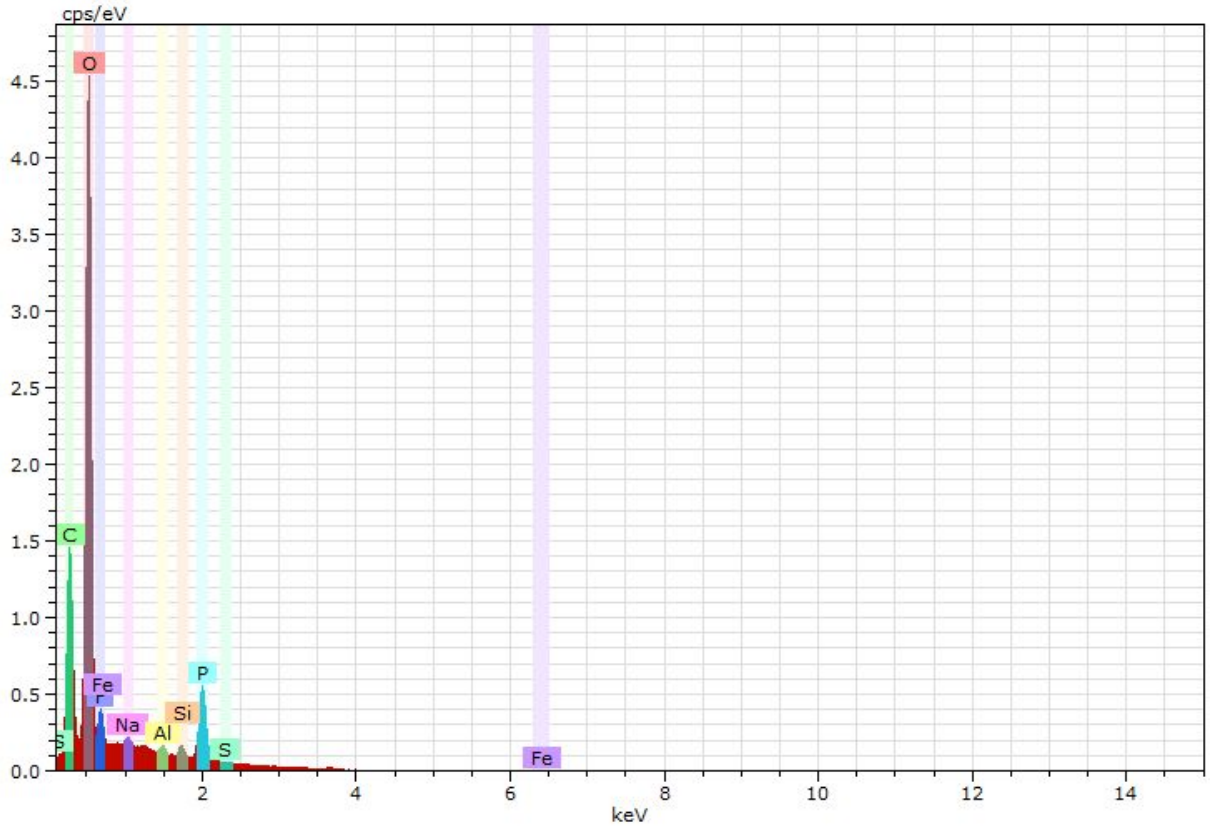

VTL2 Position 1 Spectrum

Vessel Exposed at Surface, appears filled

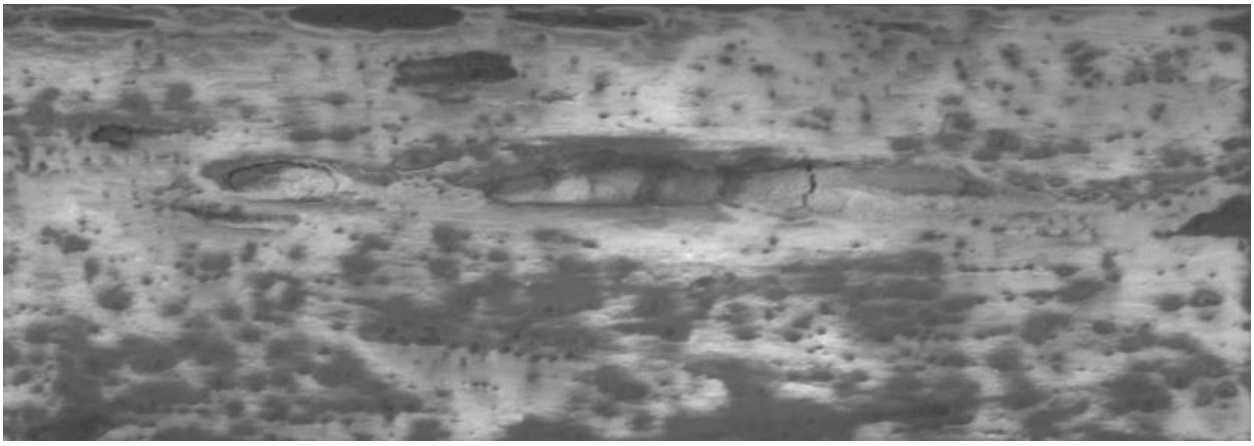

VTL2 Position 1 Sampled Area in SEM

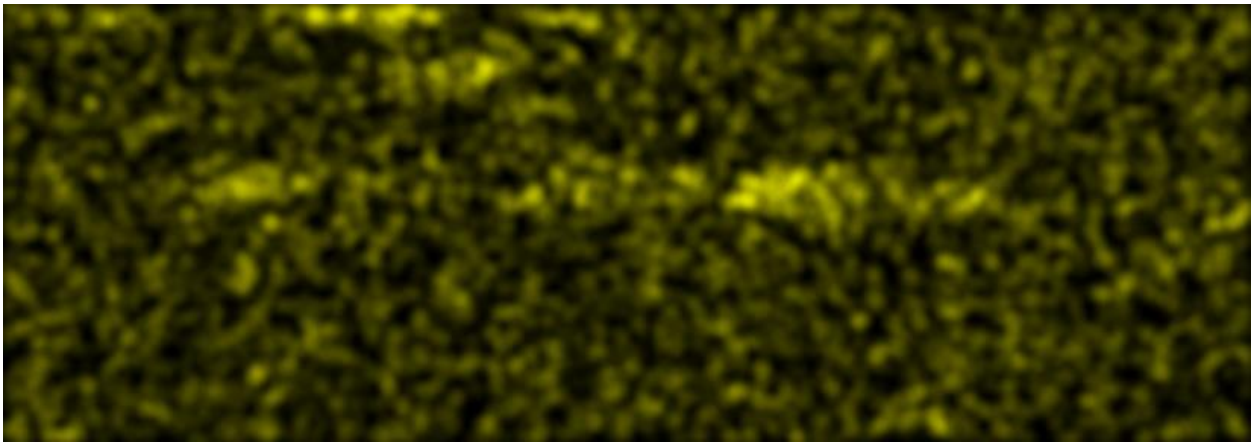

VTL2 Position 1 Aluminum

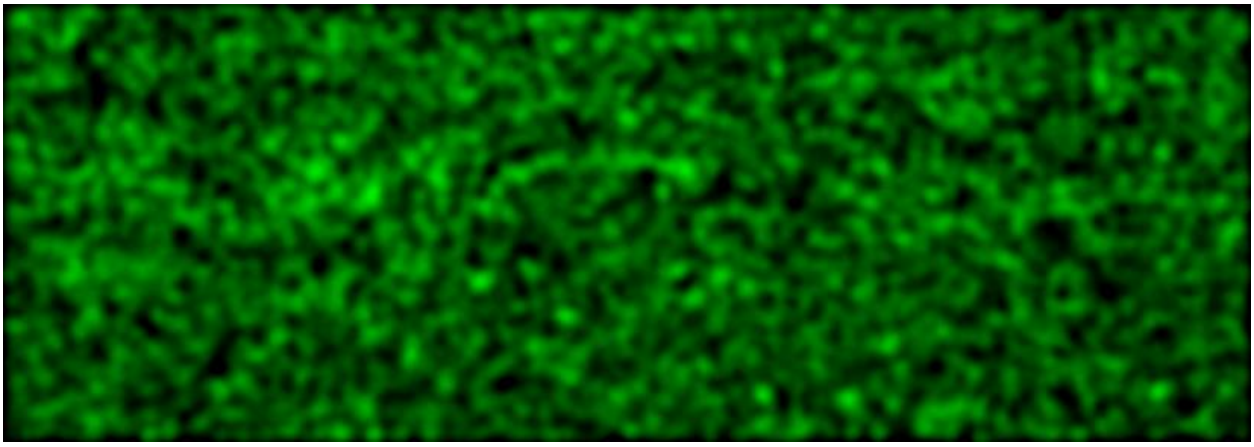

VTL2 Position 1 Carbon

VTL2 Position 1 Iron

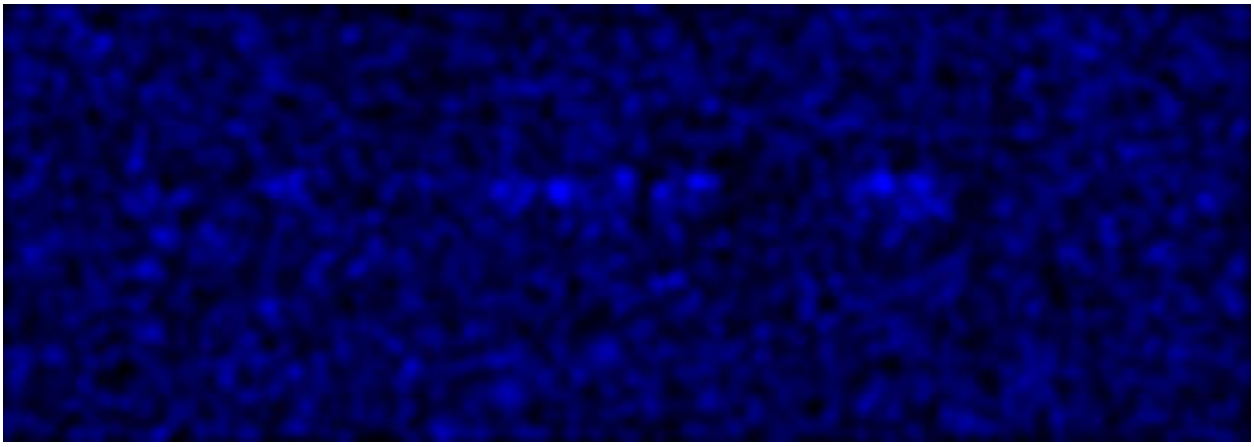

VTL2 Position 1 Fluorine

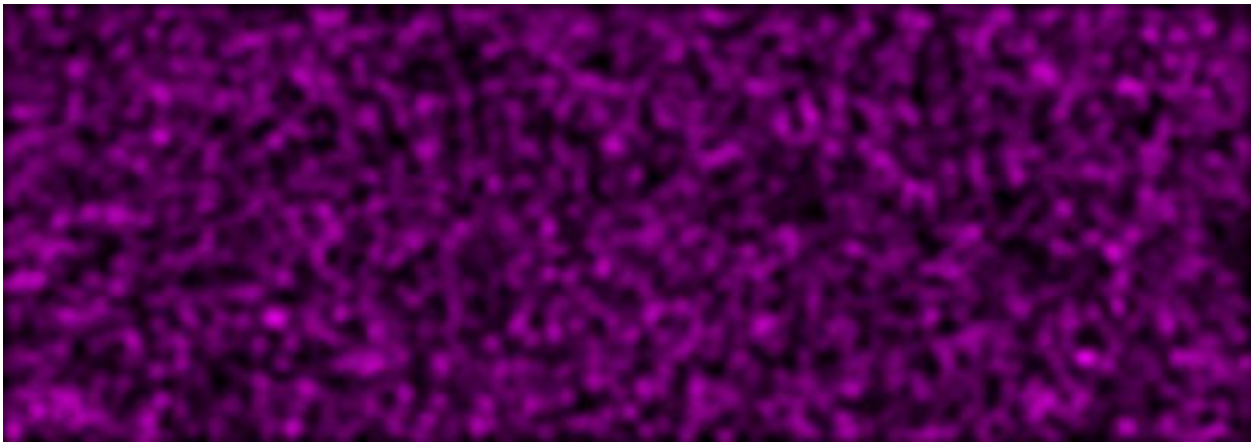

VTL2 Position 1 Sodium

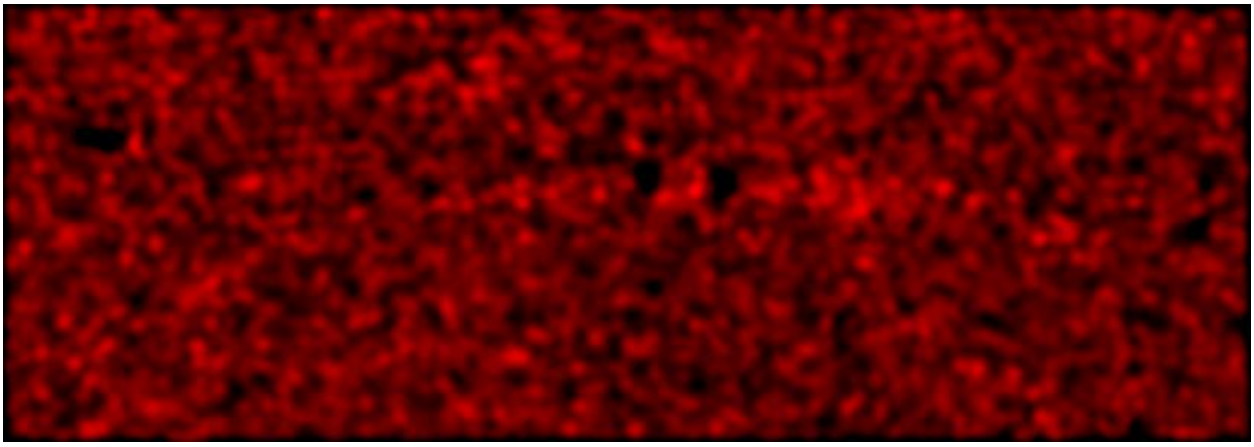

VTL2 Position 1 Oxygen

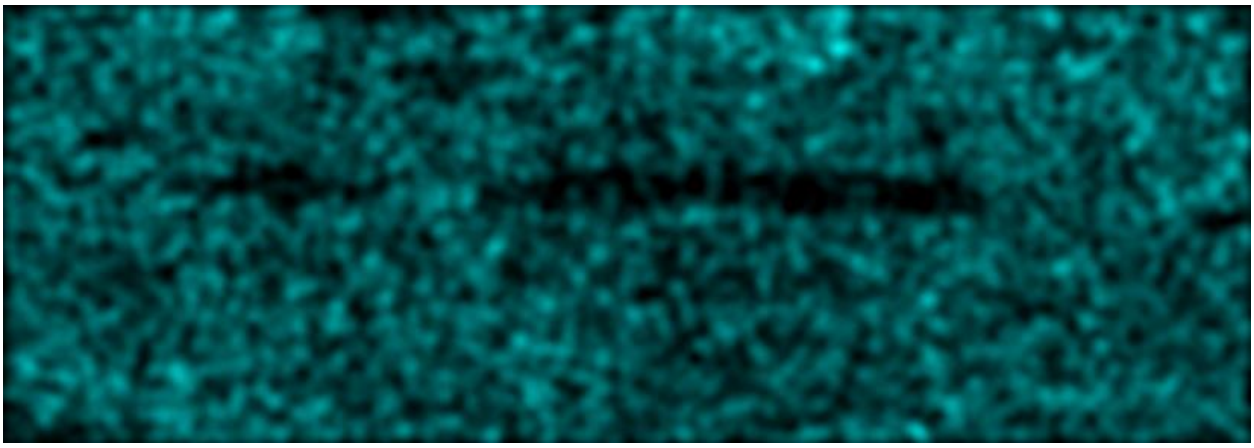

VTL2 Position 1 Phosphorus

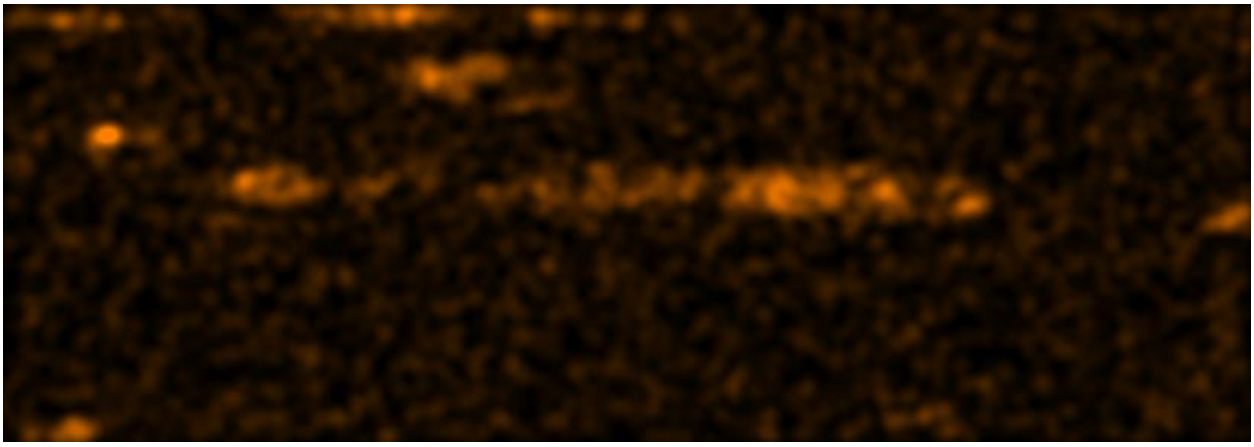

VTL2 Position 1 Silicon

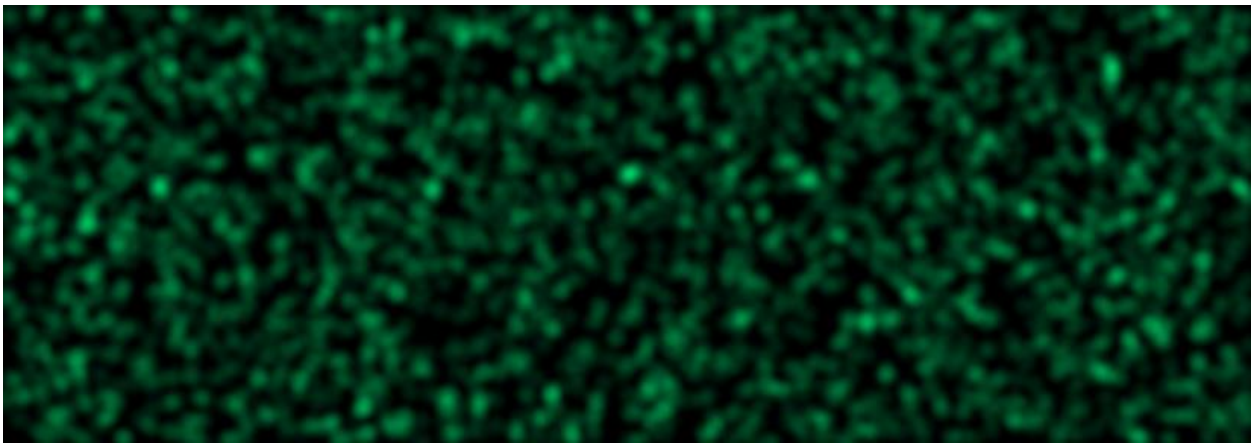

VTL2 Position 1 Sulfur

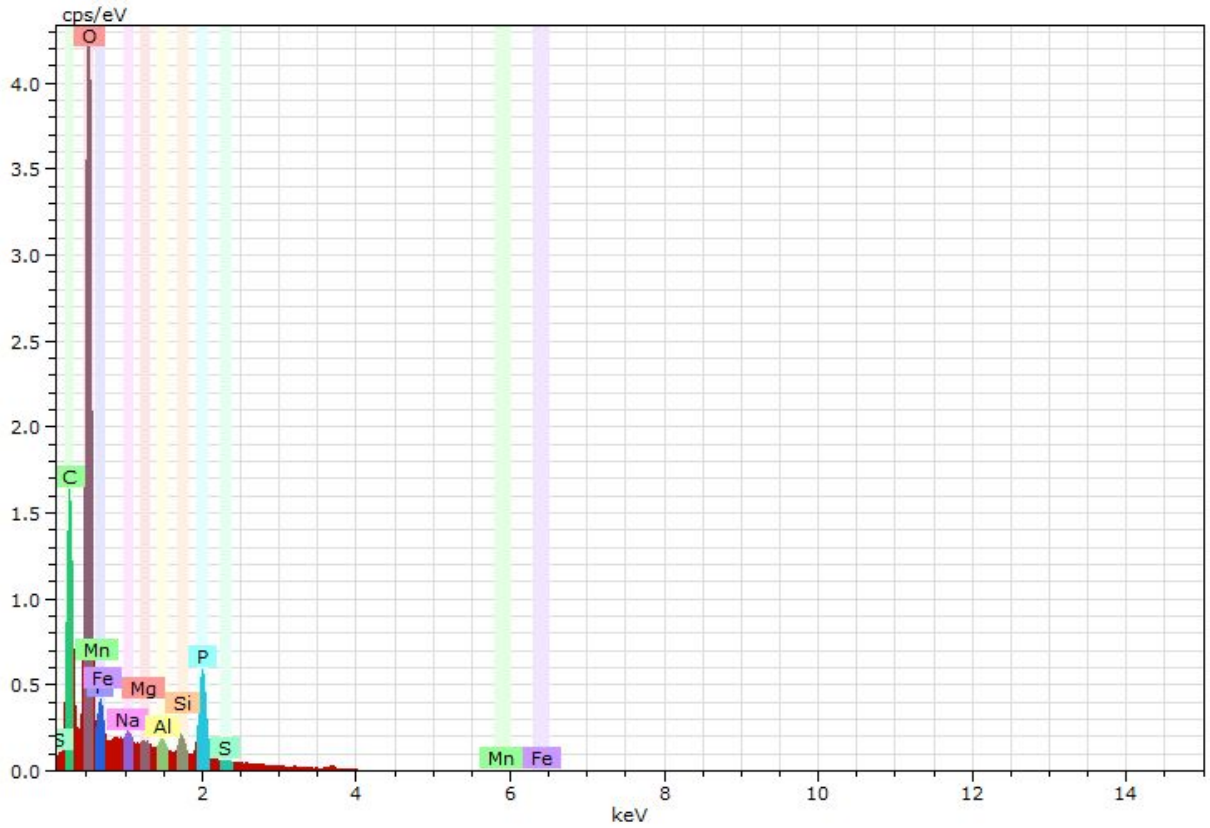

VTL2 Position 2 Spectrum

Vessel Exposed at Surface partially filled

VTL2 Position 2 Sampled Area in SEM

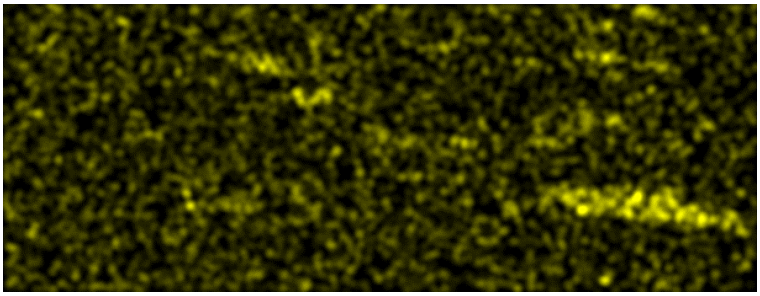

VTL2 Position 1 Aluminum

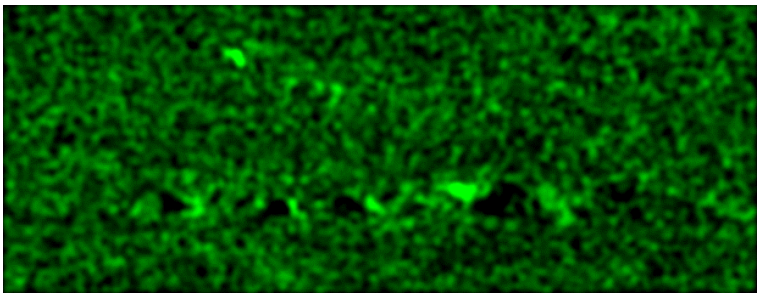

VTL2 Position 1 Carbon

VTL2 Position 1 Iron

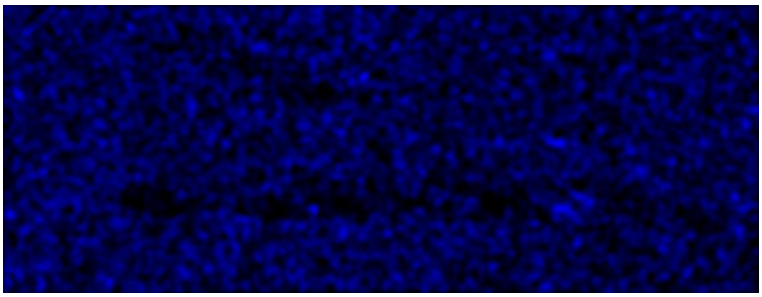

VTL2 Position 1 Fluorine

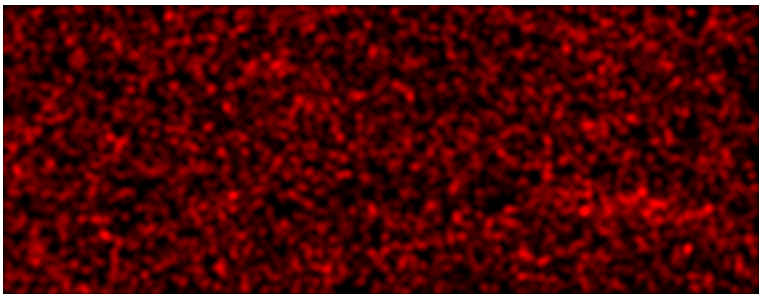

VTL2 Position 1 Magnesium

VTL2 Position 1 Manganese

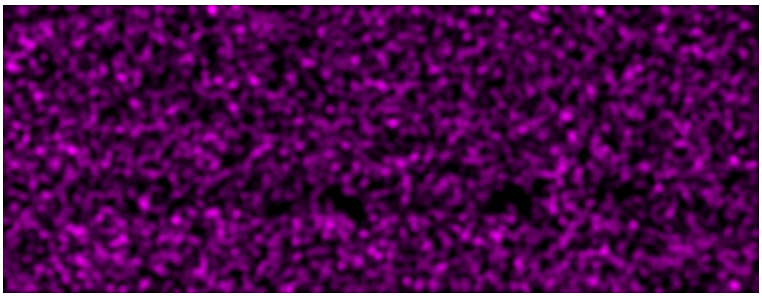

VTL2 Position 1 Sodium

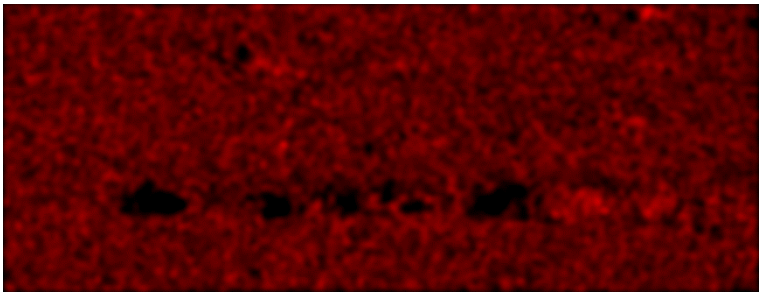

VTL2 Position 1 Oxygen

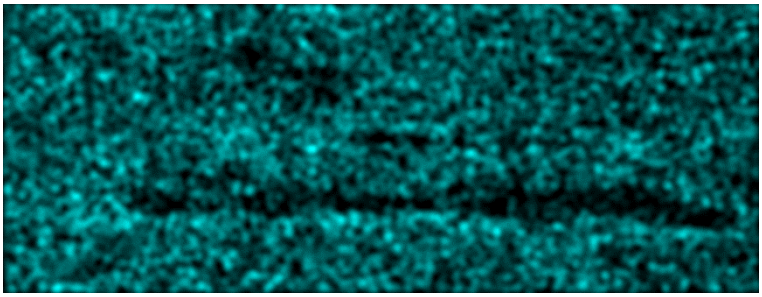

VTL2 Position 1 Phosphorus

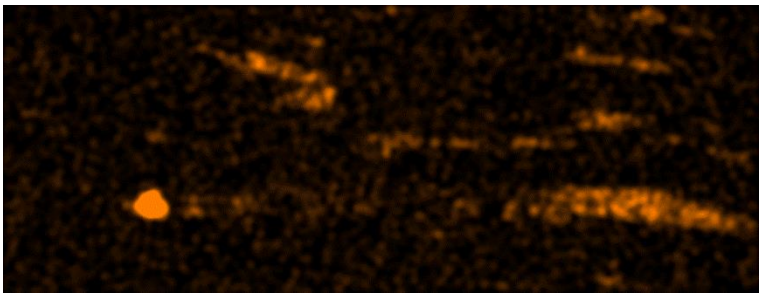

VTL2 Position 1 Silicon

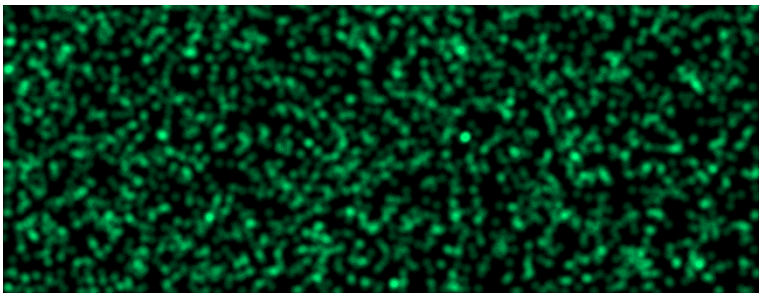

VTL2 Position 1 Sulfur

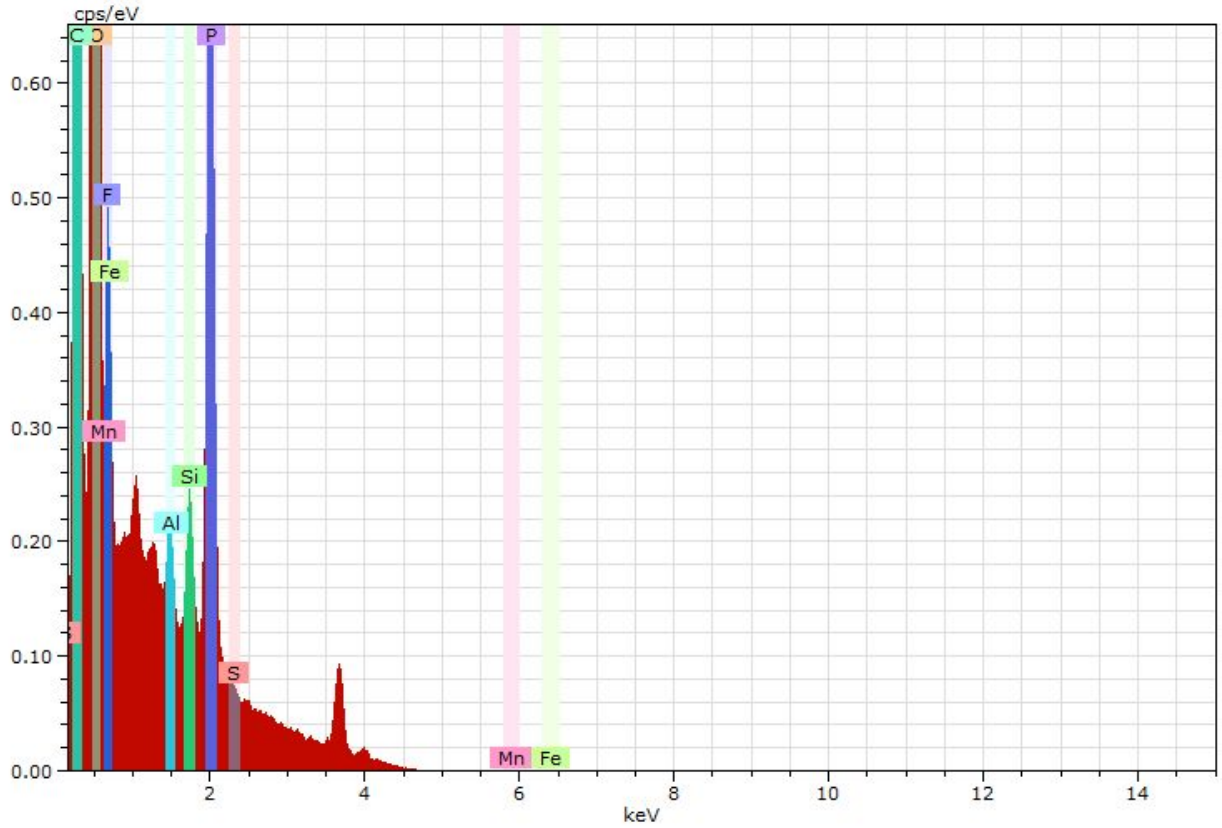

VTL2 Position 3 Spectrum - Vessels Exposed at Surface, appear partially filled

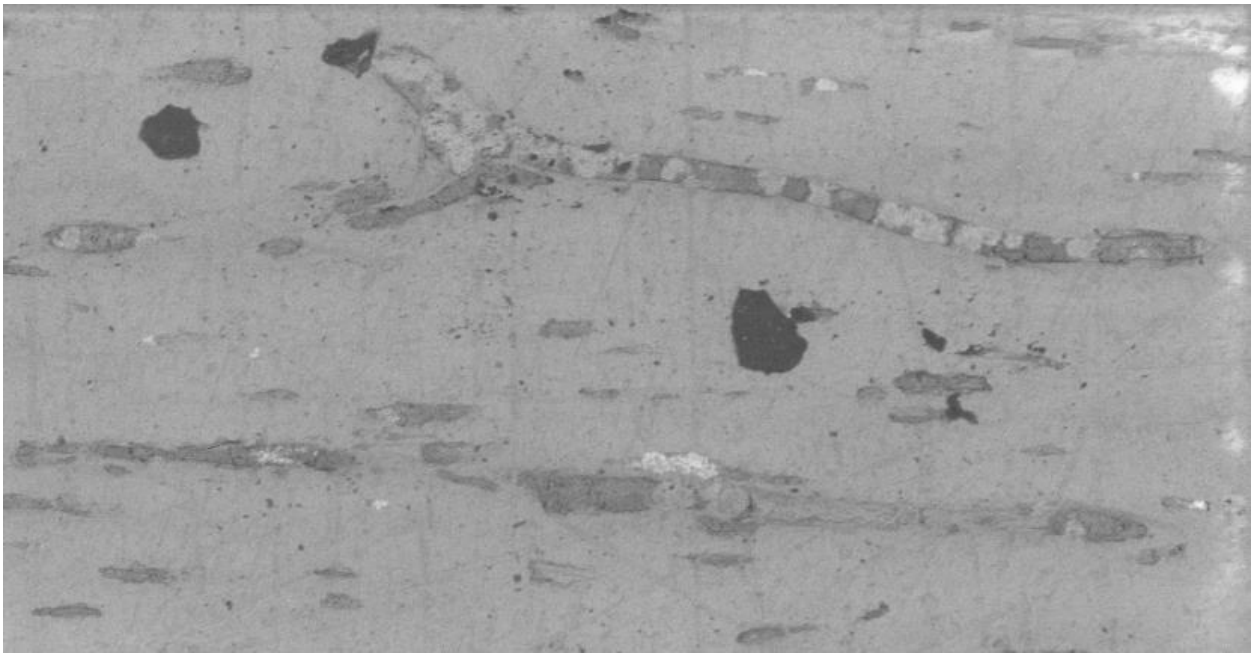

VTL2 Position 3 Sampled Area in SEM

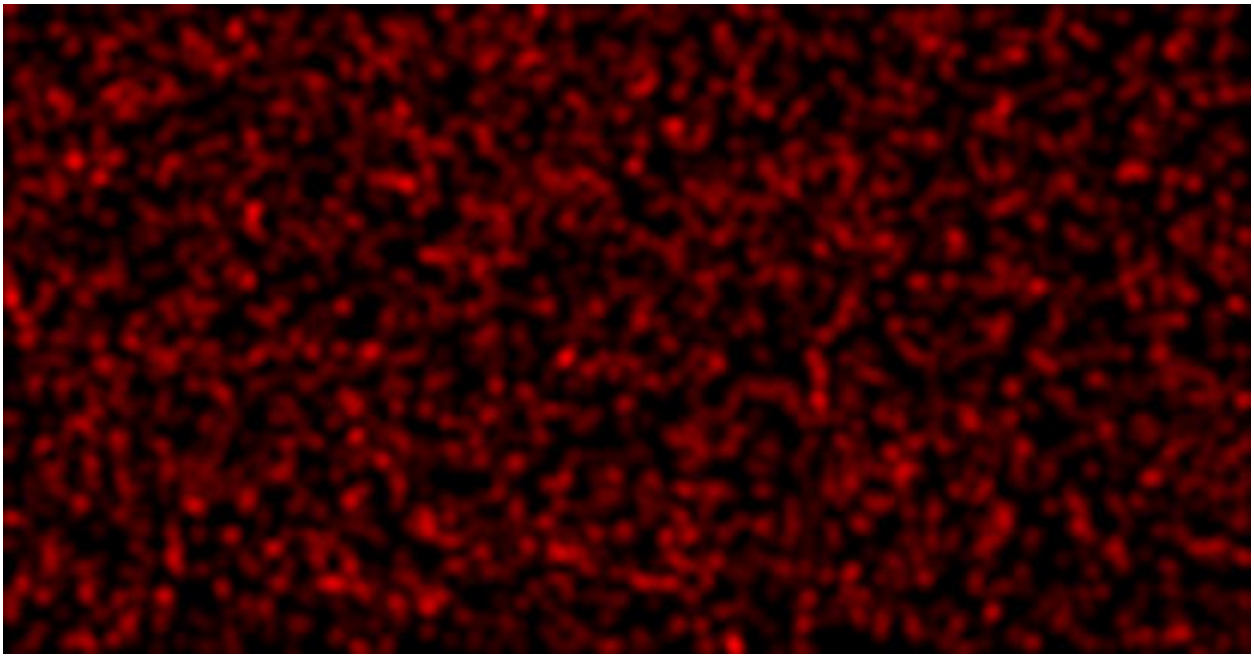

VTL2 Position 3 Sulfur

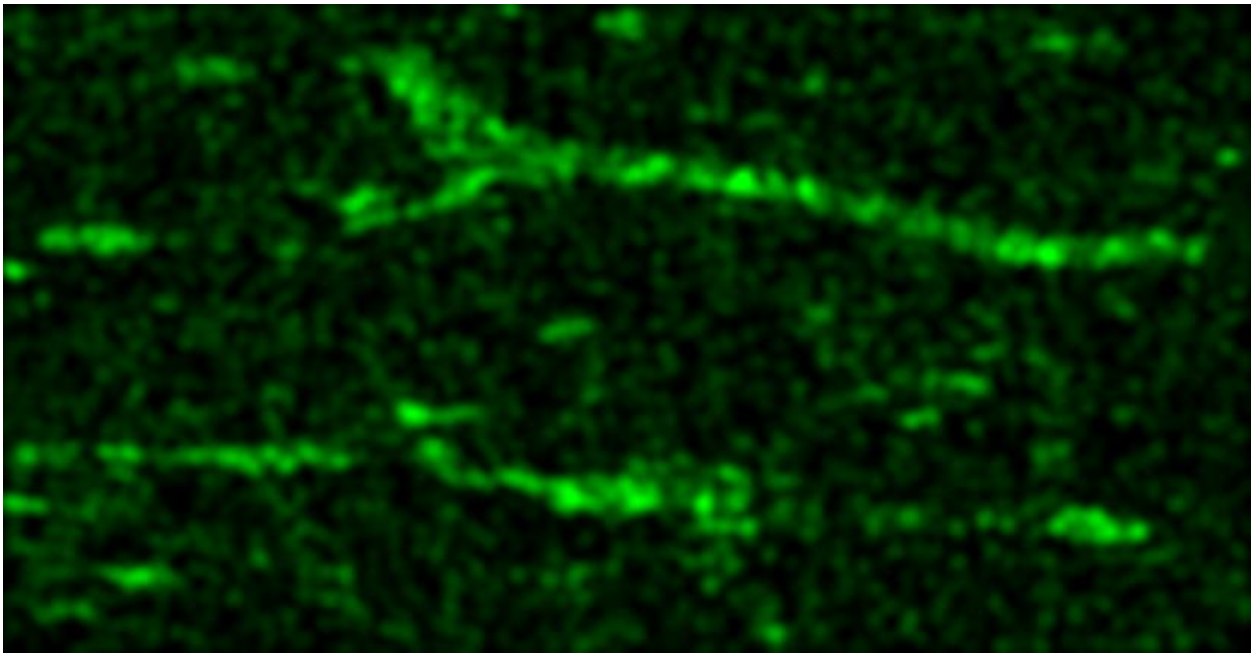

VTL2 Position 3 Silicon

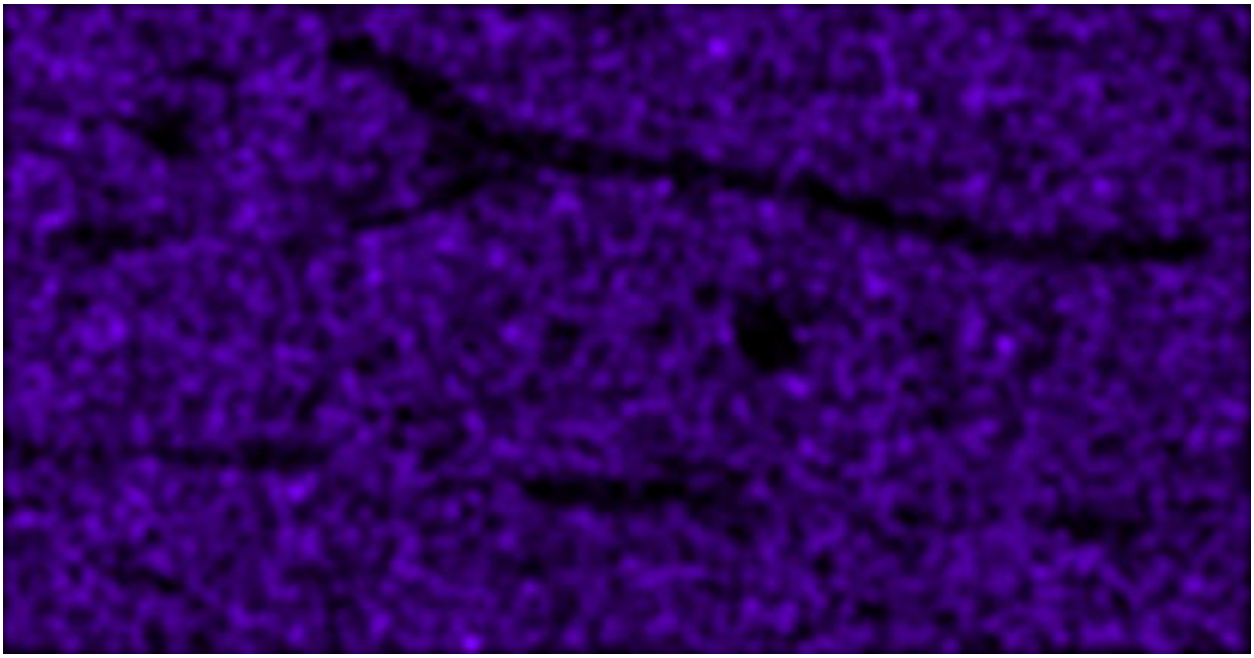

VTL2 Position 3 Phosphorus

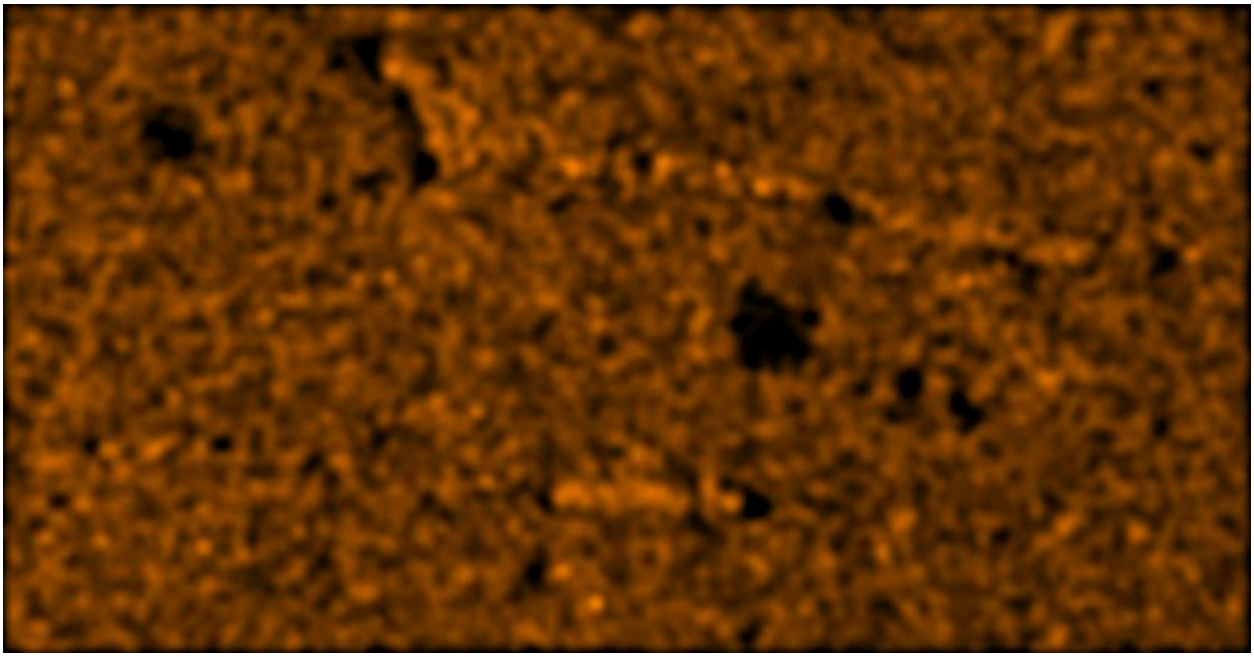

VTL2 Position 3 Oxygen

VTL2 Position 3 Manganese

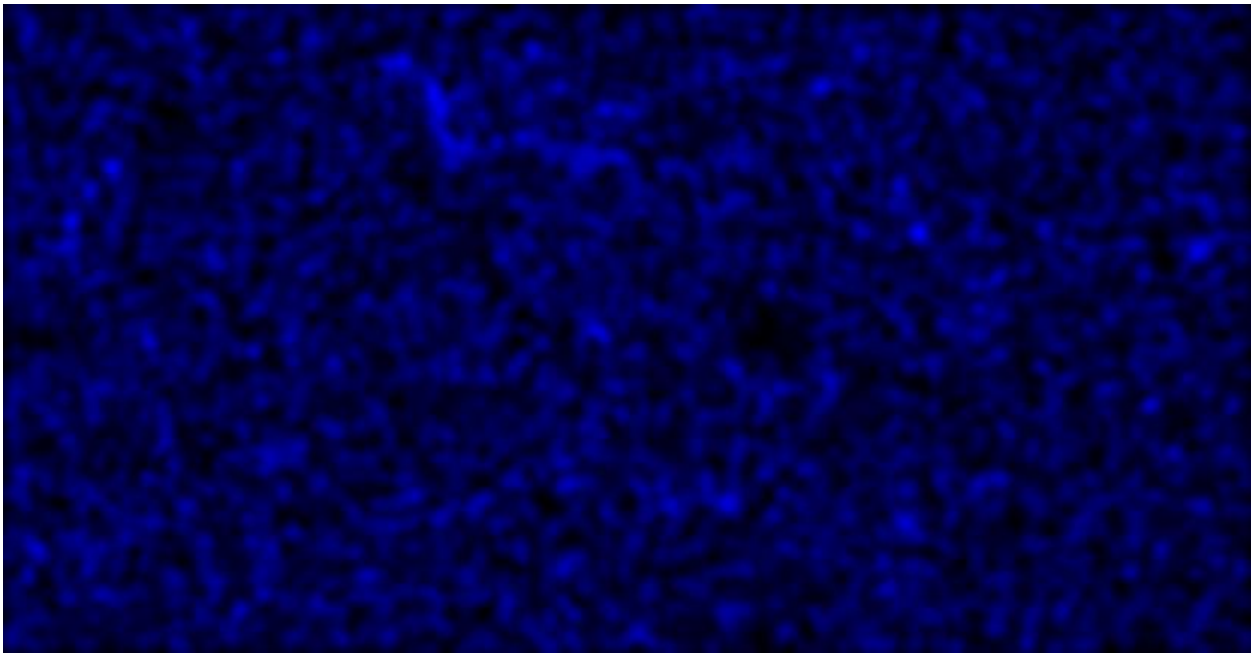

VTL2 Position 3 Fluorine

VTL2 Position 3 Iron

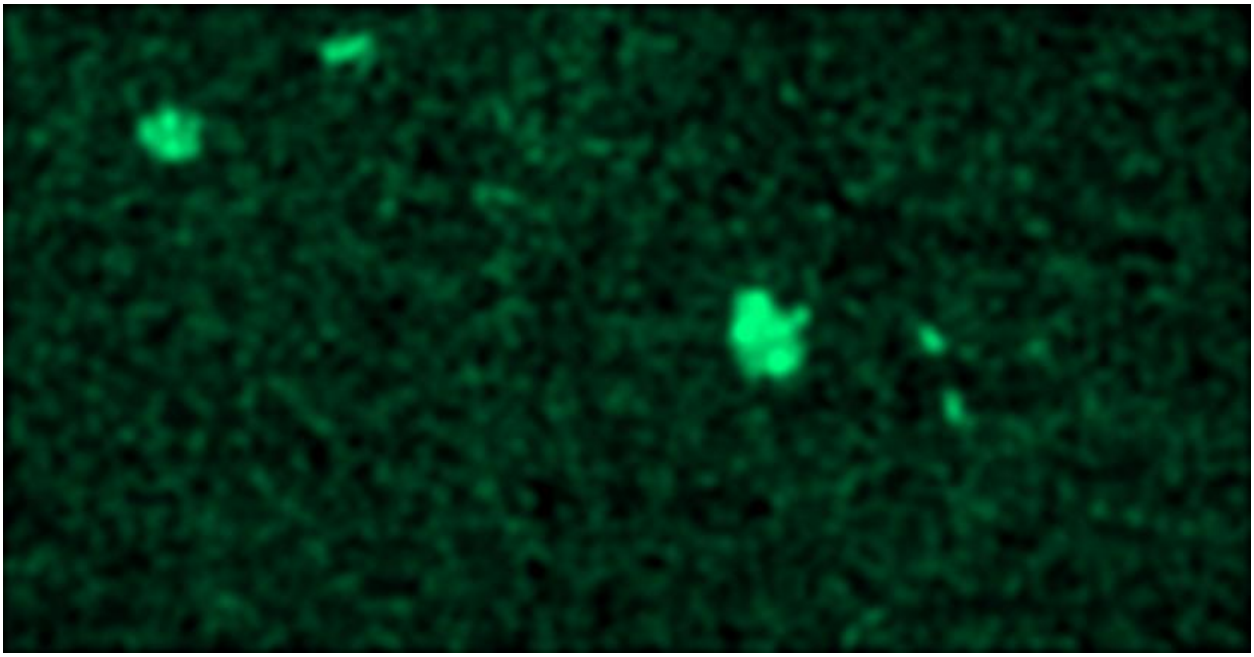

VTL2 Position 3 Carbon

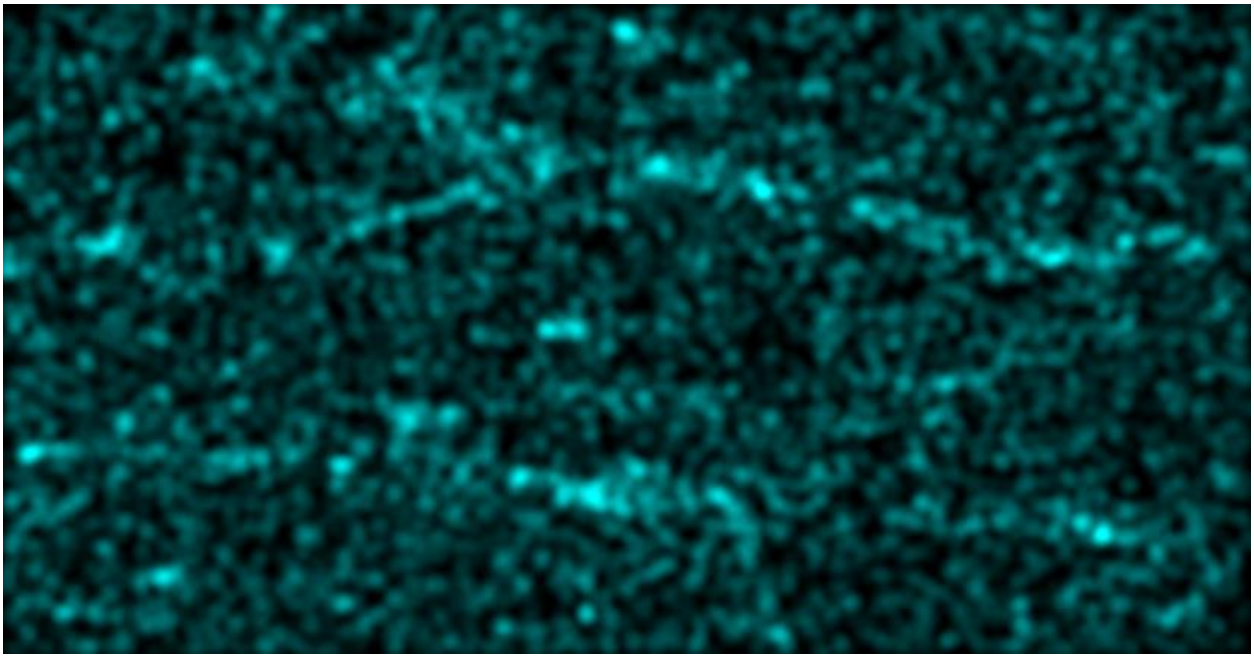

VTL2 Position 3 Aluminum

VTL2 Position 3 Transects

Yellow line indicates transect with spectrum tracked below.

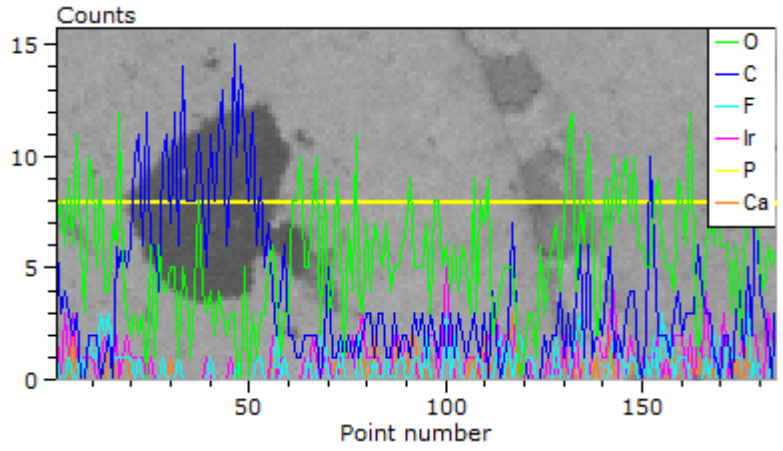

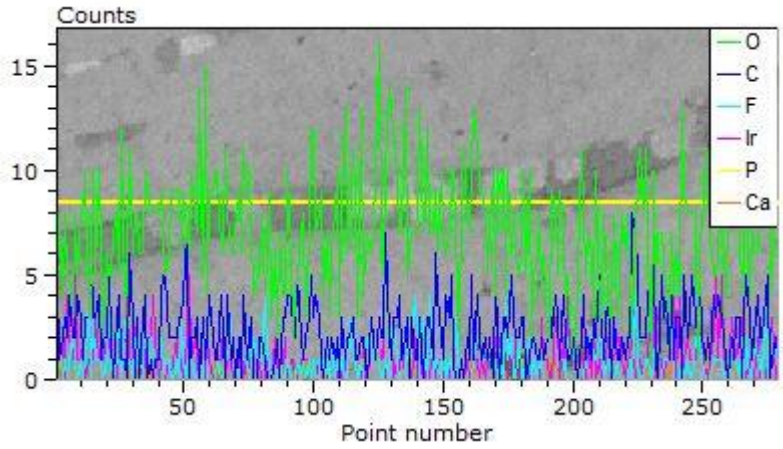

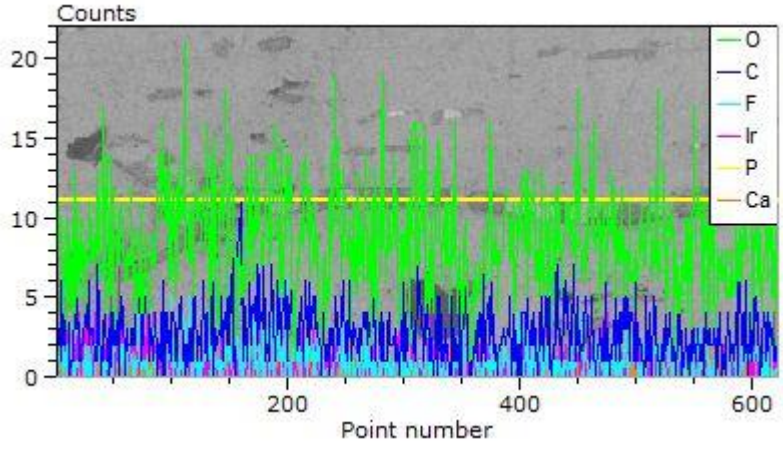

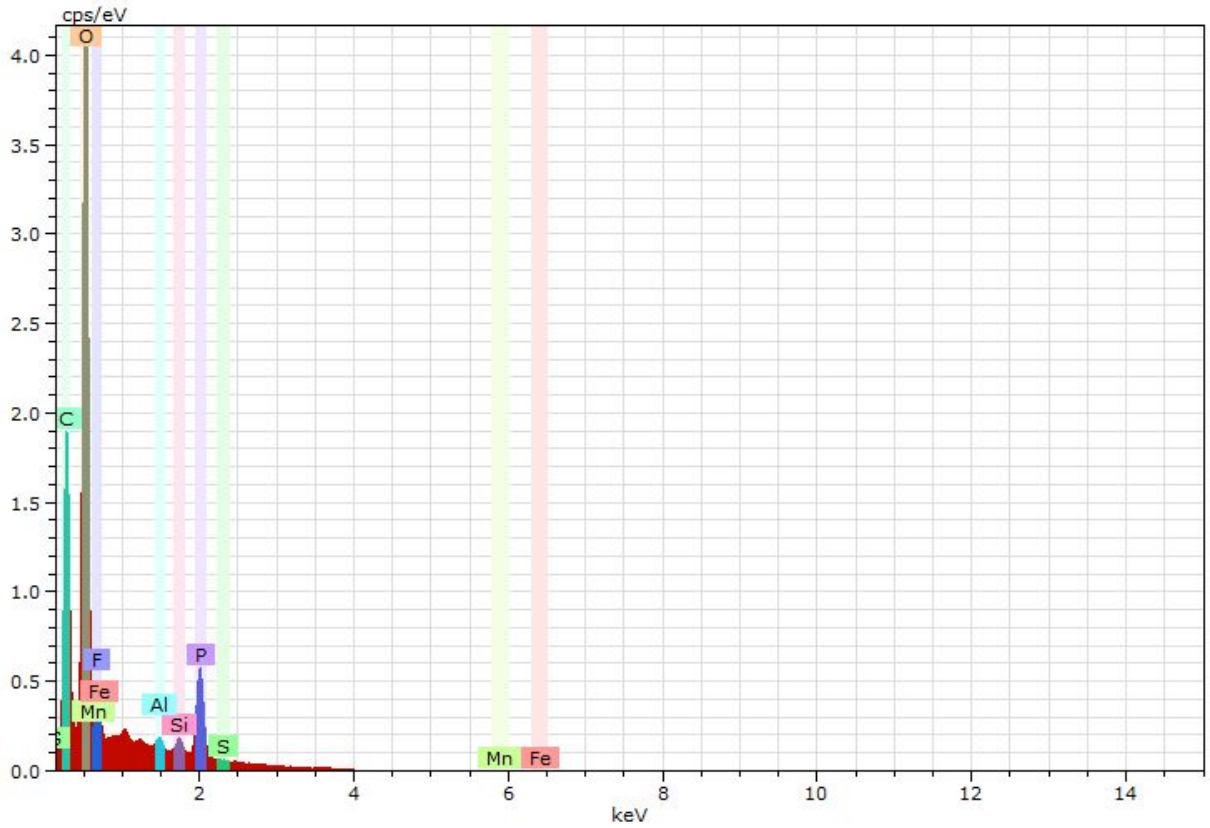

VTL2 Position 4 Spectrum

Sample slightly fractured with vessel in and out of surface

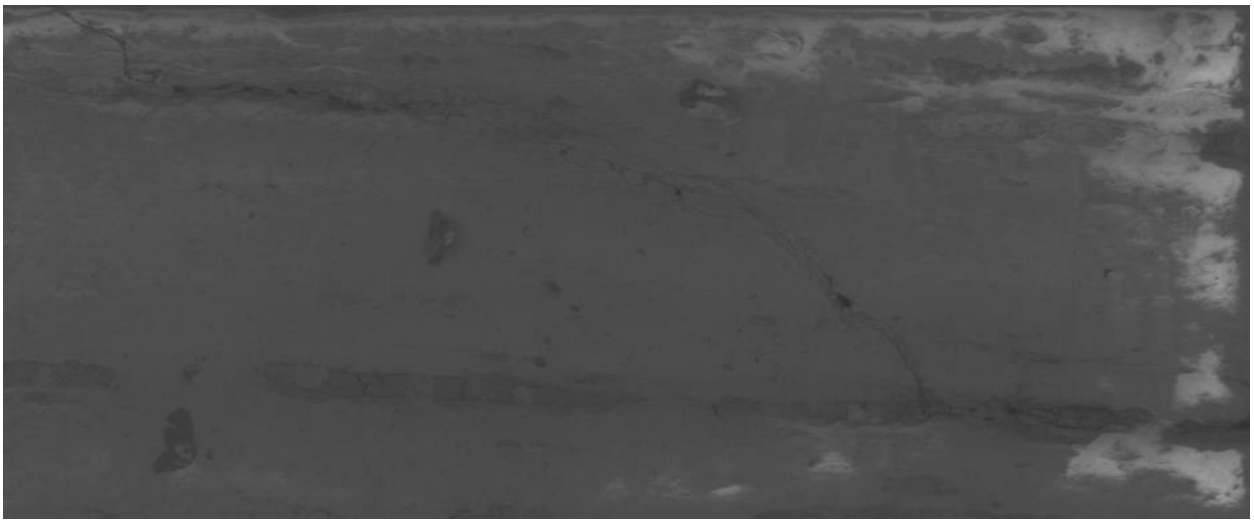

VTL2 Position 4 Sampled area in SEM

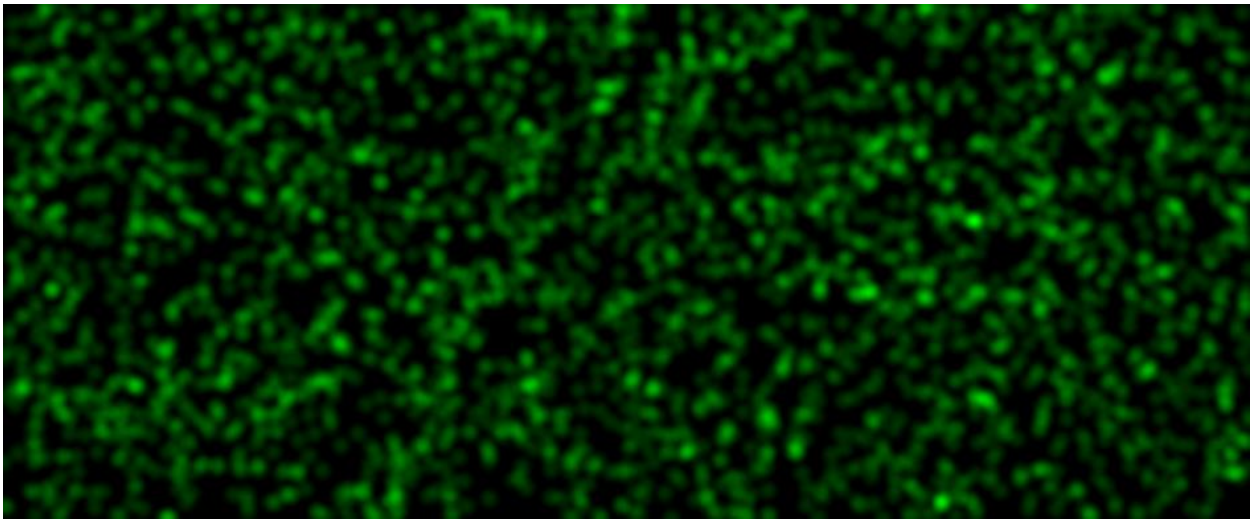

VTL2 Position 4 Sulfur

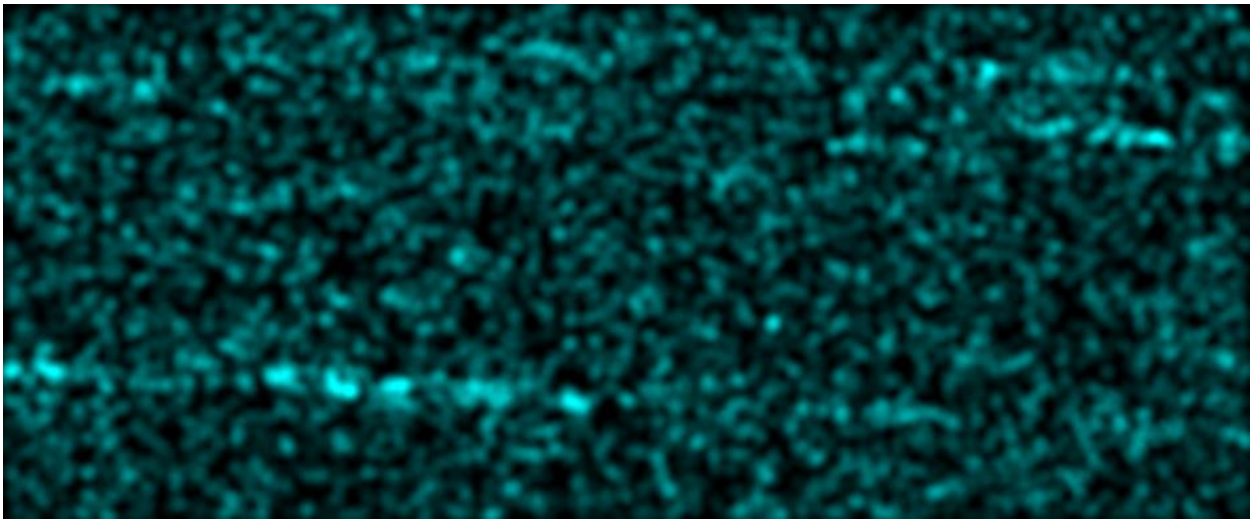

VTL2 Position 4 Aluminum

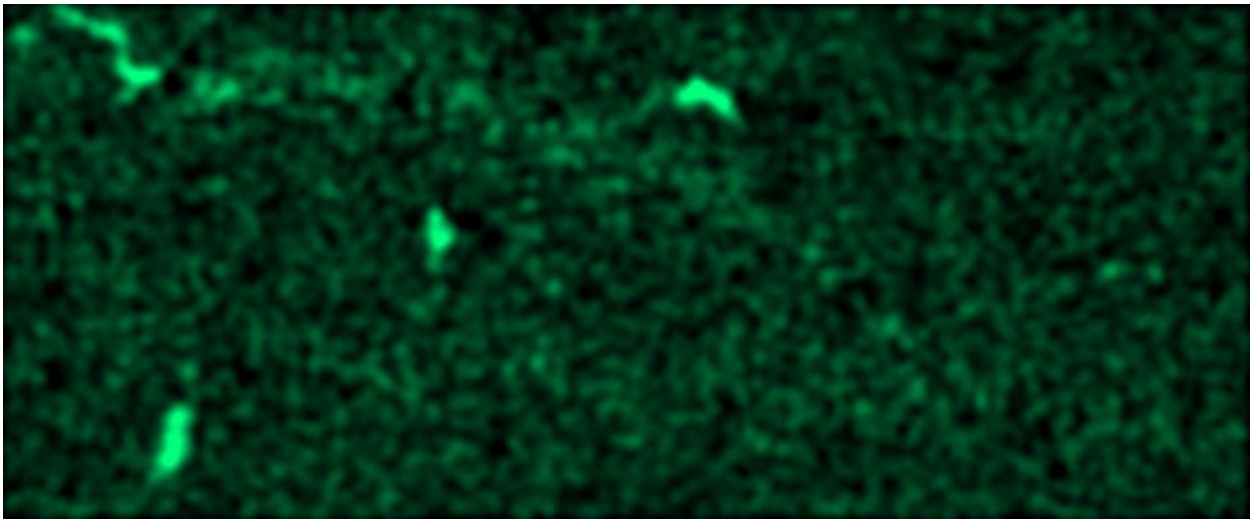

VTL2 Position 4 Carbon

VTL2 Position 4 Iron

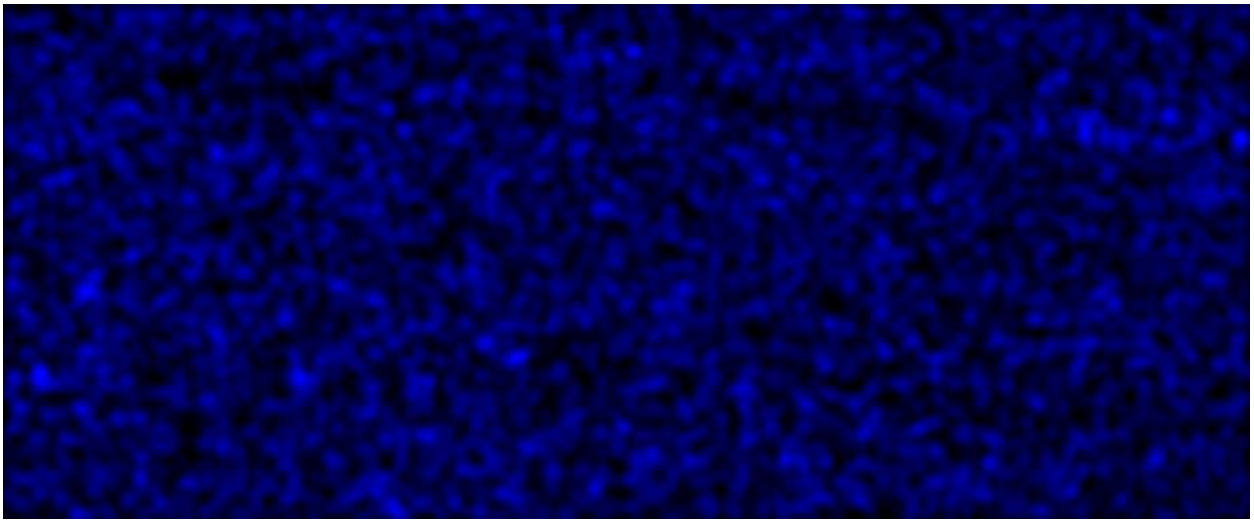

VTL2 Position 4 Fluorine

VTL2 Position 4 Manganese

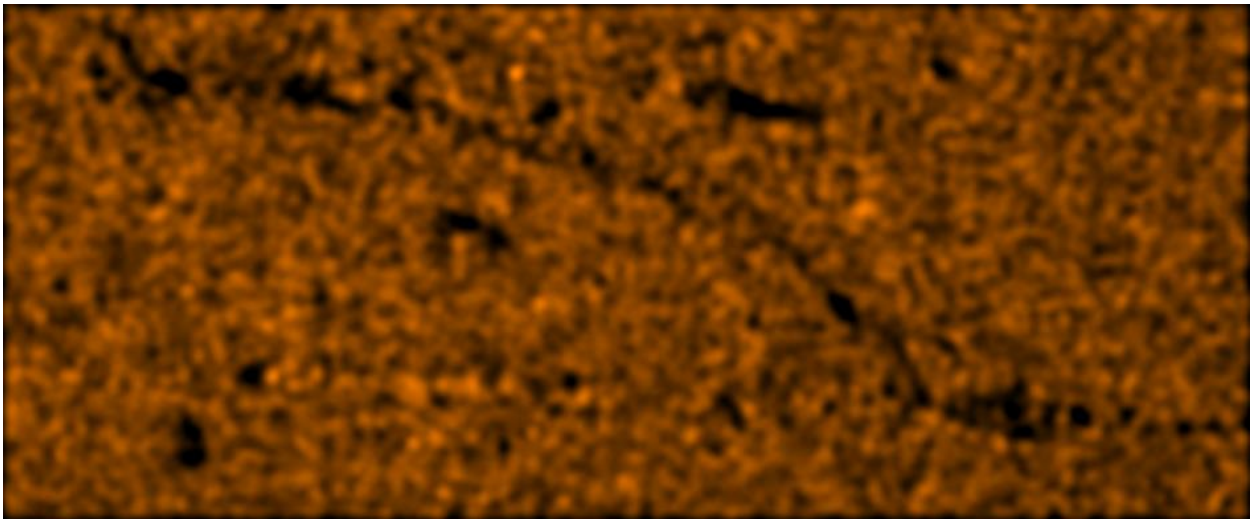

VTL2 Position 4 Oxygen

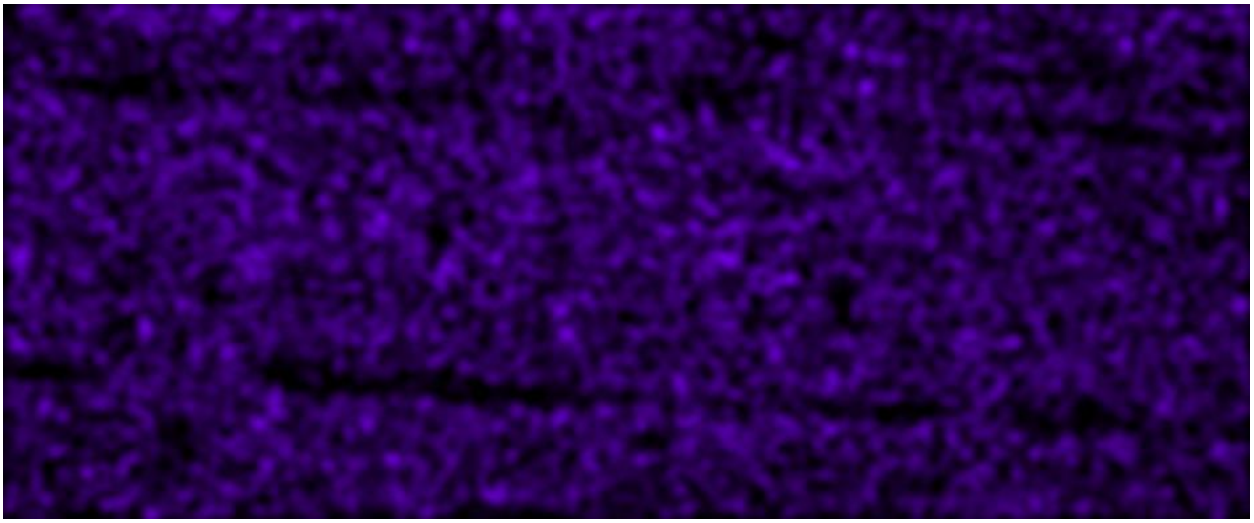

VTL2 Position 4 Phosphorus

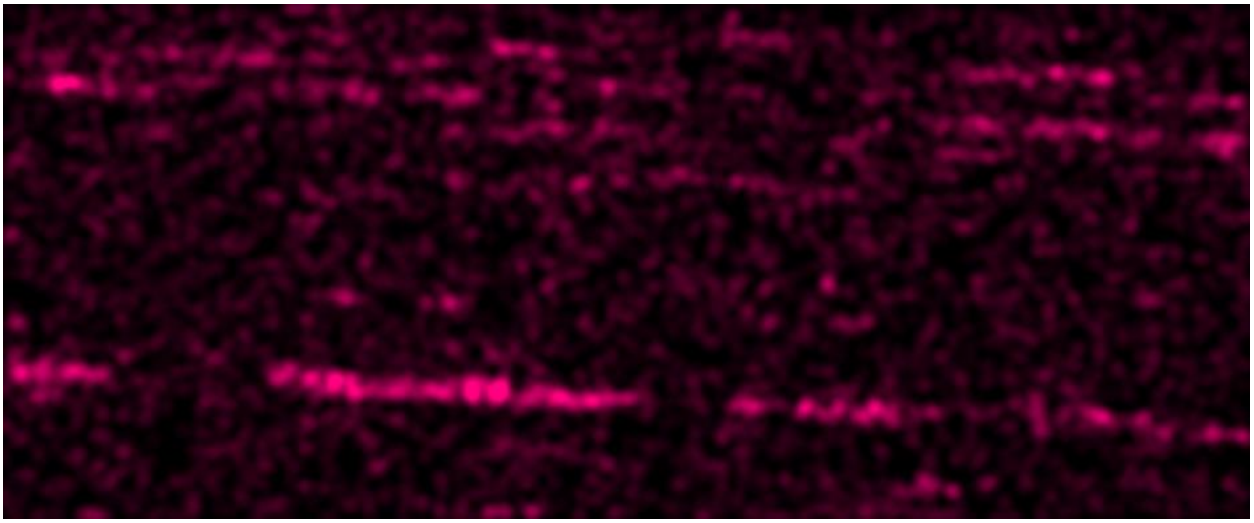

VTL2 Position 4 Silicon

Appendix E: TOF-SIMS Peak Assignment Table

Appendix Table 7. TOF-SIMS on *in situ* specimen (Fig 5). Calibration Peaks. Deleted OH- from calibration as it was 1.23 counts/shot, identified as unreliable by ionTOF. Small shoulder to the positive side of the main ^{37}Cl peak could not be distinguished by IONTOF.

Peak Identity	+/-(mu)	Mass	Dev. (ppm)	Counts/Shot	Min Mass (m/z)	Max Mass (m/z)	Shift Direction
C-	10	12.00055	247.3	0.13	11.99	12.021	+
^18O-	10	17.99971	82.9	0.02	17.982	18.029	+
F-	10	18.99895	189.4	0.61	18.981	19.027	narrow
Na-	10	22.99032	-109.3	0	22.967	23.011	narrow
C2-	10	24.00055	111.3	0.13	23.982	24.041	+
Al-	10	26.98209	-390.4	0	26.952	26.988	+
Si-	5	27.97748	-195.3	0.07	27.946	28.01	narrow
P-	5	30.97431	-65.9	0.02	30.941	31.006	+
Cl-	5	34.9694	89.1	0.6	34.935	35.021	narrow
^37Cl-	5	36.96645	34.7	0.21	36.929	37	+
PO-	10	46.96923	-31.3	0.03	46.928	47.031	+
PO2-	10	62.96414	86.3	0.36	62.922	63.046	widen
PO3-	10	78.95905	18.5	0.43	78.899	79.088	+

Appendix Table 8. TOF-SIMS on *in situ* specimen (Fig 5). Peak Assignments. (tables of 20)

Peak Identity	Mass	Deviation (ppm)	Min Mass(m/z)	Max Mass(m/z)	Shift	Dev.	Explained	AltIdentit
^10B-	10.0135	85.1	10.006	10.027	narrow	85.1	78.8	BeH-
B-	11.0099	-10.4	11.001	11.027	narrow	-10.4	100	^10BH-
CH-	13.0084	311.7	12.991	13.066	widen	311.	100	^13C-
O-	15.9955	455.4	15.985	16.023	narrow	455.	100	NH2-
OH-	17.0033	348	16.988	17.03	narrow	348	100	NH3-
C2H-	25.0084	162.3	24.988	25.045	narrow	162.	100	BN-
CN-	26.0036	189.5	25.984	26.049	+	189.	100	^10BO-
CHN-	27.0114	137.5	26.988	27.067	none	137.	100	^10BOH-
SiH-	28.9853	-139.2	28.946	29.032	narrow	-	100	^29Si-
SiH2-	29.9931	-96.1	29.942	30.052	+	-96.1	100	^29SiH-
CH3O-	31.0189	33.2	31.005	31.047	-	33.2	100	LiC2-
O2-	31.9904	-151.1	31.941	32.027	narrow	-	100	PH-
PH2-	32.99	-2.6	32.948	33.041	+	-2.6	100	^30SiH3-
^34S-	33.9684	107.1	33.934	34.04	narrow	107.	100	H2S-
C3-	36.0005	47.6	35.974	36.045	narrow	47.6	100	OHF-
C2O-	39.9955	11	39.946	40.059	narrow	11	100	NaOH-
C2HO-	41.0033	-19.8	40.946	41.073	+	-19.8	100	LiH2S-
CNO-	41.9985	107.2	41.963	42.078	+	107.	100	CH3Al-
AlO-	42.977	65.5	42.933	43.068	+	65.5	100	MgF-
CO2-	43.9904	-4.2	43.93	44.071	+	-4.2	100	AlOH-

Dev.	Explained	m/z	AltIdentit	Dev.	Explained	m/z	AltIdentity	Dev.	Explained	m/z
-620.9	100	10.0206	^30Si--	2250	0.3	9.9918				
-1051	100	11.0213	BeH2-	-1693.1	100	11.0284				
655.3	12.9	13.0039	BH2-	-1004.8	100	13.0255				
-1032.4	100	16.0193	^13CH3-	-1539	0.1	16.0274	CH4-	-1818.3	100	16.0318
-1051.8	100	17.0271	^13CH4-	-1528.3	100	17.0352				
-19.8	100	25.0129	^LiF-	-65.6	43.1	25.0141	BeO-	-191.4	100	25.0076
5.8	1.6	26.0084	C^13CH-	-122.1	29.6	26.0117	LiF-	-246.2	100	26.015
-39.3	17.8	27.0162	C^13CH2-	-162.5	58.2	27.0196	BeH2O-	-301.1	100	27.0233
145.7	17.6	28.977	AlH2-	-568.3	100	28.9977	^13CO-	-605.6	7.3	28.9988
179.3	14.2	29.9849	NO-	-276.5	100	29.9985	AlH3-	-510.8	100	30.0056
110.1	100	31.0166	^13CH2O	177.3	1	31.0145	H4Al-	212.3	100	31.0134
106.6	100	31.9821	^30SiH2-	-138.3	0.7	31.99	S-	404.1	47.9	31.9726
-240	2.1	32.9978	O2H-	-252.4	100	32.9982	HS-	285.9	100	32.9804
-477.3	100	33.9883	PH3-	-757.4	100	33.9978	^SiH4-	-988	100	34.0056
15.8	100	36.0017	CHNa-	114.4	100	35.9981	^LiNO-	-316.6	37.9	36.0137
71.2	100	39.9931	LiHS-	-13.6	100	39.9964	^25MgNH-	-34.5	3.3	39.9973
-4.2	100	41.0043	CH2Al-	155.2	100	40.9977	BeO2-	37.6	100	41.0026
-60.1	100	42.0056	MgH2O-	163.9	42	41.9962	^10BO2-	-6.6	10.7	42.0033
-97.1	100	42.984	CP-	128.2	100	42.9743	BS-	-49	100	42.9819
121.9	100	43.9848	BHS-	10	100	43.9897	CHP-	183.1	100	43.9821

Notes
under dev threshold but substantiated by presence in EDS
presence of C2H- seemed better supported due to alignment with calibration peaks not assigned peaks
shouldered peak, could not distinguish species
shouldered peak, could not distinguish species
slight shoulder, could represent PH- & O2-
slight shoulder, could represent ^34S- & H2S-
shouldered, small peak slightly heavier
possible lighter shoulder, very faint

Peak Identity	Mass	Deviation (ppm)	Min Mass (m/z)	Max Mass (m/z)	Shift Direction	Dev.	Explained	AltIdentity1
C2HO-	41.0033	-19.8	40.946	41.073	+	-19.8	100	LiH2S-
CNO-	41.9985	107.2	41.963	42.078	+	107.2	100	CH3Al-
AlO-	42.977	65.5	42.933	43.068	+	65.5	100	MgF-
CO2-	43.9904	-4.2	43.93	44.071	+	-4.2	100	AlOH-
CHO2-	44.9982	-2.1	44.946	45.063	+	-2.1	100	CNF-
NO2-	45.9935	3	45.951	46.055	+	3	100	CH2S-
SO-	47.9675	-51.1	47.923	47.982	narrow	-51.1	100	Mg2-
CHOF-	48.0017	-6.5	47.982	48.056	-	-6.5	100	CH4S-
CH2OF-	49.0095	36.9	48.94	49.2	widen	36.9	100	SiH5O-
^34SO-	49.9633	-184.3	49.93	49.97	+	-184.3	87.4	^49TiH-
H_4FAl-	50.0118	-40	49.97	50.42	+	-40	100	C3^13CH-
ClO-	50.9643	-7.1	50.92	90.99	none	-7.1	100	CK-
^37ClO-	52.9614	-103.4	52.91	52.97	none	-103.4	100	VH2-
H3SF-	53.9945	20.3	53.93	54.13	widen	20.3	100	NaNOH-
SiAl-	54.959	146.9	54.89	54.98	none	146.9	100	NaS-
CaO-	55.9581	11	55.86	56.06	none	11	100	MgS-
CaOH-	56.9659	56.4	56.87	57	none	56.4	100	MgHS-
SiHNO-	58.9833	0.2	58.92	59.09	none	0.2	100	CHSN-
CaHF-	59.9694	55.8	59.9	60.12	widen	55.8	100	CHPO-
PNO-	60.9723	19.6	60.92	61.08	widen	19.6	100	CNCl-

Dev.	Explained	m/z	AltIdentity2	Dev.	Explained	m/z	AltIdentity3	Dev.	Explained	m/z
-4.2	100	41.0043	CH2Al-	155.2	100	40.9977	BeO2-	37.6	100	41.0026
-60.1	100	42.0056	MgH2O-	163.9	42	41.9962	^10BO2-	-6.6	10.7	42.0033
-97.1	100	42.984	CP-	128.2	100	42.9743	BS-	-49	100	42.9819
121.9	100	43.9848	BHS-	10	100	43.9897	CHP-	183.1	100	43.9821
-87	100	45.002	AlH2O-	121.3	100	44.9927	CH2P-	181.1	100	44.99
115.7	100	45.9883	PNH-	182.2	100	45.9852	SiH2O-	120.7	100	45.988
-115.7	19.2	47.9706	^34SN-	-133.5	1.6	47.9715	^46TiH2-	-78	0.6	47.9688
-52.9	100	48.0039	PNH3-	10.9	100	48.0009	C4-	17.4	100	48.0005
-3.8	100	49.0115	CNOLi-	-65.6	100	49.0145	C4H-	60.3	100	49.0084
-42.5	4.5	49.9562	^50Ti	175.8	70.3	49.9453	^50Cr-	150.6	1.6	49.9466
-38.7	9.3	50.0117	C4H2-	-128.1	100	50.0162	CH3OF-	-151	100	50.0173
-5.9	100	50.9643	^49TiH2	-2.3	4	50.9641	SF-	-138.7	100	50.971
-80.7	100	52.9602	C^41K-	-122.5	22.6	52.9624	CrH-	132.3	100	52.9486
-10	100	53.9961	C2NO-	-54.5	100	53.9985	CHNAl-	48.3	100	53.993
85.5	100	54.9624	CrH3-	46.5	100	54.9645	^41KN-	29.9	18.3	54.9654
18	100	55.9577	C^44Ca-	47.1	1	55.956	^54FeH2-	51	9.9	55.9558
63.4	100	56.9655	^29SiCO-	-50.2	10.5	56.972	CH^44Ca-	92	1.1	56.9639
-3.7	100	58.9835	MgH3S-	36.7	100	58.9811	MgOF-	74.5	100	58.9789
-72.2	100	59.977	C2HCl-	-75.2	23.3	59.9772	CSO-	86.4	100	59.9675
16.7	100	60.9725	SiHO2-	-26.8	100	60.9751	CHSO-	-30.6	100	60.9754

Notes
under dev threshold but substantiated by presence in EDS
presence of C2H- seemed better supported due to alignment with calibration peaks not assigned peaks
shouldered peak, could not distinguish species
shouldered peak, could not distinguish species
slight shoulder, could represent PH- & O2-
slight shoulder, could represent ^34S- & H2S-
shouldered, small peak slightly heavier
possible lighter shoulder, very faint
messy, looks like 3-4 similar mass peaks stacked up, cut off clearest shoulder but program couldn't pick it up separately
small - shoulder, could be MgS-
many fits

Peak Identity	Mass	Deviation (ppm)	Min Mass (m/z)	Max Mass (m/z)	Shift Direction	Dev.	Explained	AltIdentity1
Mg2O-	63.9655	20.1	63.89	64.14	widen	20.1	100	^34SNO-
C3H3Al-	66.0056	4.7	65.91	66.11	none	4.7	100	C2H5^37Cl-
C3H4Al-	67.0134	0.3	66.9	67.12	none	0.3	100	C^13CN3-
C4HF-	68.0068	1.5	67.89	68.17	+	1.5	100	CH2OF2-
SiC2H3N-	69.004	-26	68.95	69.1	narrow	-26	100	CH2SNBe-
Cl2-	69.9383	-38.3	69.87	69.97	-	-38.3	100	CNi-
C4H6O-	70.0424	62.3	69.97	70.12	-	62.3	100	C3H6N2-
C3H3O2-	71.0139	23.1	70.96	71.14	none	23.1	100	SiC2H5N-
FeO-	71.9304	23.2	71.85	71.98	none	23.2	100	C^60Ni-
C2H2NO2-	72.0091	-3.7	71.98	72.12	none	-3.7	100	CH3SNB-
FeOH-	72.9382	29.5	72.87	72.97	+	29.5	100	CH^60Ni-
C2H3NO2-	73.0169	-10.8	72.97	73.15	none	-10.8	100	^30SiC2H5N-
H2Al2F-	74.9777	1.7	74.87	75.11	none	1.7	100	SiHNO2-
CSO2-	75.9624	29.5	75.9	76.06	none	29.5	100	CH2O^46Ti-
CNOCl-	76.9674	15.6	76.9	77.07	none	15.6	100	^SiH2SN-
CH2S2-	77.9603	11	77.9	78.08	+	11	100	SiH2SO-
PSOH-	79.9491	-14.2	79.87	80.03	narrow	-14.2	100	ZnNH2-
PH2SO-	80.9569	4	80.85	81.1	+	4	100	CH2SCl-
AlH3-	81.953	7.1	81.86	82.08	+	7.1	100	TiH2O2-
H3SO3-	82.9808	-10	82.86	83.12	narrow	-10	100	CH2SNNa-

Dev.	Explained	m/z	AltIdentity2	Dev.	Explained	m/z	AltIdentity3	Dev.	Explained	m/z
6.7	4.3	63.9664	SO2-	68.5	100	63.9624	^46TiH2O-	48.3	5.4	63.9637
4.5	65.2	66.0056	CH2SN^6Li-	-9	2.5	66.0065	CHSNLi-	96.2	100	65.9995
4.3	10.8	67.0131	CH3SN^6Li-	-13.1	100	67.0143	C3^13CH2O-	-15.8	14.5	67.0145
-15.3	100	68.0079	BF3-	26.7	100	68.0051	SiC3H4-	-27.9	100	68.0088
-18.8	100	69.0035	C^13CN2O-	-39.7	0.5	69.005	CH2NO^25Mg-	31.9	2.3	69
-4.6	100	69.5359	^FeO-	7.1	95.1	69.9351	FeN-	-42.8	100	69.9386
-98	100	70.0536	C2^13CH5N2-	-34.2	50.3	70.0492	C2H4N3-	81.5	100	70.0411
-58.9	100	71.0197	^30SiC3H5-	28.8	5.1	71.0134	CH3SN^10B-	47.7	30.5	71.0121
10.2	2.6	71.9313	^17GaH-	-14	4.4	71.9331	CaS-	-43.6	100	71.9352
5	100	72.0085	^30SiC2H4N-	2	0.4	72.0087	LiSNOH3-	-17.4	100	72.0101
16.7	8.1	72.9392	^71GaH2-	-7.2	12.8	72.9409	CoN-	48.8	100	72.9368
-5.2	1.3	73.0165	^29SiCH4N2-	22.5	2.8	73.0145	SiCH5N2-	-90.6	100	73.0227
-5.3	100	74.9782	MgH3SO-	23.4	100	74.9761	^30SiH3N-	0.2	10.9	74.9778
12.5	6.6	75.9637	ScNOH-	31.9	100	75.9623	SiO3-	32.6	100	75.9622
9.8	12.8	76.9678	AlH2SO-	50.3	100	76.9647	CH2PS-	85.2	100	76.962
13.9	100	77.9601	CaF2-	16	100	77.9599	^44CaH2O2	-4	1.2	77.9615
-5.4	30.9	79.9484	CHOV-	9.2	100	79.9473	CHSCl-	-16.4	48.6	79.9493
1.8	57.1	80.9571	CO2^37Cl-	12.2	100	80.9563	Si2C2H-	-61.2	100	80.9622
-4.9	100	81.954	C3^46Ti-	4.8	9.1	81.9532	SNCH-	14.6	100	8.9524
-13.3	100	82.9811	O4F-	16.8	100	82.9786	C2H3OCa-	-18.4	100	82.9815

Notes
many fits
- shoulder program doesn't pick up

Peak Identity	Mass	Deviation	Min Mass (m/z)	Max Mass (m/z)	Shift Direction	Dev.	Explained	AltIdentity1
C3HO3-	84.9931	-4.5	84.87	85.13	none	-4.5	100	^30SiC3H3O-
Cl2O-	85.9332	-113.7	85.86	85.97	+	-113.7	100	C^37Cl2-
KSO-	86.9312	-8.4	86.85	86.98	none	-8.4	100	CHGe-
C2H3N2O2-	87.02	20.7	86.98	87.14	none	20.7	100	^13CC3H3OF-
MnHS-	87.9185	-16.9	87.84	88.07	none	-16.9	100	^87RbH-
MnH2S-	88.9263	-50.7	88.85	88.98	none	-50.7	100	AsN-
C2H6O2Al-	89.0189	-3.7	88.98	89.16	none	-3.7	100	C2H5SN2-
CSNO2-	89.9655	2.5	89.95	90.17	none	2.5	100	SiNO3-
CaH3SO-	90.9536	-16.3	90.82	91.14	none	-16.3	100	CHNOTi-
S2N2-	91.9508	8.7	91.84	92.11	none	8.7	100	CH3SSc-
SiHSO2-	92.9472	-15.4	92.83	92.98	none	-15.4	100	CHO2Ti-
C3HN4-	93.0207	1.5	92.98	93.14	none	1.5	100	C5H3NO-
Na2SO-	93.9471	-0.1	93.82	94.13	none	-0.1	100	CoH3O2-
Na2SOH-	94.9549	7.3	94.84	95.14	none	7.3	100	CH4OCu-
Si2C2O-	95.9493	-17.6	95.82	96.15	none	-17.6	100	CHNO^53Cr-
C3HSN2-	96.9866	0.4	96.84	97.19	none	0.4	100	SiC2HN2O-
SiCl2-	97.9152	70.1	97.83	97.95	none	70.1	100	^96MoH2-
C4H2O3	98.0009	-5	97.95	98.17	none	-5	100	^30SiC4H4O-
Si3CH3-	98.9548	-8.3	98.83	99.19	none	-8.3	100	CH2SNK-
CHSOK-	99.9391	-25.4	99.84	100.1	none	-25.4	100	VO3H-

Dev.	Explained	m/z	AltIdentity2	Dev.	Explained	m/z	AltIdentity3	Dev.	Explained	m/z
0.3	2.2	84.9827	Si2C2H5-	-9.3	100	84.9935	SiHN4-	-57.2	100	84.9976
-104.2	6.6	85.9324	CGe-	19.5	51.9	85.9217	RbH-	37.7	100	85.9202
11	60.4	86.9296	^53H2S-	18.3	10.6	86.9289	COCo-	21.2	100	86.9287
12.7	3.3	87.0207	^30SiC2H5N2-	25.4	3.8	87.0196	C6^13CH2-	25.8	5.7	87.0196
-6.3	5.2	87.9176	^72GeO-	-6.1	9.2	87.9175	^87SrH-	-2.8	2.5	87.9173
-38.3	100	88.9252	^72GeOH-	-39.9	35	88.9254	^57FeO2-	-44.6	9.4	88.9258
7.2	100	89.0179	SiCh5N2O-	9.8	100	89.0177	C2^13CH4O3-	-15.8	3.2	89.0199
5	100	89.9653	^30SiCH2SN-	7	63.7	89.9651	CH2NO^46Ti-	-11.9	11.2	89.9668
-24.1	100	90.9543	CH3S^44Ca-	6	2.4	90.9516	Si2H3S-	23.9	100	90.9499
-4	100	91.952	^41KH3SO-	-13	11.9	91.9528	CH3O^61Ni-	17.8	1.4	91.95
-4.1	100	92.9461	ScSNH2-	-16	100	92.9473	CH2N^66Cu-	-14	60.7	92.9471
-12.9	100	93.022	C2H5O4-	15.9	100	93.0193	C3H9Ti-	20.3	100	93.0189
0.1	100	93.9471	^77SeNH3-	0.5	44.7	93.947	CH3S^47Ti-	-8.5	18.3	93.9479
-8.1	100	94.9564	^29SiH2SO2-	10.5	3.3	94.9546	^29SiSiC2N-	-15.3	7	94.957
6.4	7.7	95.947	ScH3SO-	7.4	100	95.9469	CH3O^65Cu-	9.4	14.9	95.9467
2.8	100	96.9864	C2H4O2^37Cl	-9.8	19.6	96.9876	^29SiSiC3H4-	14	13.5	96.9853
11.9	100	97.9209	CHS^53Cr-	9.7	17.8	97.9211	CHRb-	19.2	100	97.9202
-0.8	4.5	98.0005	Si2C3H6-	-9.2	100	98.0014	^30SiC2H2N3	12.9	4.2	97.9992
-10.8	100	98.9551	Si^30SiC2HO-	0	14.5	98.954	^30SiC3HS-	-2.3	16	98.9542
-5.6	100	99.9371	CH3S^53Cr-	-2.2	5.6	99.9367	CH3Rb-	7.1	100	99.9358

Notes
3 bumps on peak, possible overlap
3 bumps on peak, possible overlap
shouldered +
shouldered +
shouldered +
two peaks not distinguished by program
shouldered +

Peak Identity	Mass	Deviation (ppm)	Min Mass (m/z)	Max Mass (m/z)	Shift Direction	Dev.	Explained
Si2CHO2-	100.9521	0.3	100.85	101.15	none	0.3	100
CaSNO-	101.9332	-8	101.83	102.11	none	-8	100
FeSNH-	102.9185	41.5	102.84	103.09	none	41.5	100
FeSO-	103.9025	35.4	103.81	104.07	none	35.4	100
FeSOH-	104.9103	44	104.82	105.11	none	44	100
SiSN2-	105.9247	-19.6	105.81	106.16	+	-19.6	100
ZrOH-	106.908	5.9	106.8	107.16	none	5.9	100
Si2H6NO2-	107.9943	-8.6	107.95	108.16	none	-8.6	100
CH3S2NO-	108.9652	7.5	108.79	109.17	none	7.5	100
CaCl2-	109.9008	-17.5	109.8	109.95	none	-17.5	100
C4H2SN2-	109.9944	6	109.95	110.17	none	6	100
C6H4Cl-	111.0007	1.2	110.94	111.19	none	1.2	100
Fe2-	111.8704	180.4	111.79	111.95	none	180.4	100
C5H4O3-	112.0166	-0.5	111.95	112.22	none	-0.5	100
SiC3HO3-	112.97	-5.5	112.81	113.19	none	-5.5	100
CSNFe-	113.9106	-21.5	113.8	113.96	none	-21.5	100
Ca2OF-	114.919	7.1	114.8	114.98	none	7.1	100
C4H7SN2-	115.0335	2.5	114.98	115.22	none	2.5	100
Si3O2-	115.9212	-4.9	115.81	116.09	none	-4.9	100
Si2HSN2-	116.9404	10.9	116.83	117.12	none	10.9	100

AltIdentity1	Dev.	Explained	m/z	AltIdentity2	Dev.	Explained	m/z	AltIdentity3	Dev.
CSNOAl-	-0.6	100	100.9521	SN^37ClOH2-	-0.7	28.4	100.9522	^30SiSi2CH3-	4.4
CHNAs-	-6.5	100	101.933	CH2O^72Ge-	-7.9	100	101.9332	CH3^87Si-	-5.1
SINH-	55.1	100	102.9171	^70GeO2H-	2.8	9.5	102.9225	CH2Y-	6.7
SiO-	48.9	100	103.9011	MnSOH-	-69.8	100	103.9134	^104Ru-	1.7
CHS^60Ni-	35.1	100	104.9112	CH^92Mo-	-2.5	19.1	104.9152	^104RuH-	10.6
CH2^92Mo-	-3.7	60.4	105.923	CSNTi-	-9.7	100	105.9236	ZiNH2-	-12.9
CHS^62Ni-	-1.6	27.1	106.9088	NbN-	-12.9	100	106.91	^61NiSN-	17.5
SiCH6SNO-	-10.8	100	107.9943	^30SiCH4NO3-	-1.1	1.4	107.9934	C5H2SN-	18.3
^29SiC4O2	0.9	10.5	108.9669	Si2C2HN2-	-12.9	100	108.9684	SiH23SNO2-	9.6
CS^66Zn-	2.4	88.2	109.8987	Ti2N-	-5.5	100	109.8995	^77SeHS-	-13.1
C3H5O2^37Cl-	-2.9	56.7	109.9954	^29SiCH5O4-	-6.8	11.6	109.9958	SiC3H2N2O-	8.1
C5^13CF2-	1.2	5.6	111.0007	SiCHN5-	1.5	100	111.0007	CH5SNO3-	11.5
Ti2O-	-6.6	100	111.8914	ZnSO-	-54.1	100	111.8967	SeS-	13.2
Si2C4H8-	-4.2	100	112.017	C3H2N3O2-	11.5	100	112.0152	^30SiC5H6O-	3.2
C4HO2-	-7.5	100	112.9703	Si^30SiC3H3O-	-1.9	3.9	112.9696	SiC2HSN2-	52.3
^100RuN-	3	100	113.9078	CNSr-	-9.3	100	113.9092	Ti2H2O-	10.3
ZnH3SO-	-2.6	100	114.9202	CrSNOH-	8	100	114.9189	CH2ORb-	-26.5
SiC3H7N2O-	4.5	100	115.0333	C2^13CH4N3O2-	-3.6	2.5	115.0343	^13CC2H5OF3-	5.9
CH2Ru-	0.4	24.6	115.9205	Si2CSO-	-6.9	100	115.9214	SiC2S2-	-8.8
VH2O4-	16.2	100	116.9398	HOFAl3-	-39.2	100	116.9463	CH3NO^72Ge-	-20.2

Explained	m/z	Notes
8.5	100.9516	shouldered +
36.1	101.9329	
100	102.922	
21.3	103.906	
92.4	104.9138	
100	105.924	shouldered +
3.1	106.9068	shouldered +
100	107.9913	
100	108.9659	wide - shoulder
14.7	109.9004	
100	109.9942	
100	110.9996	
100	111.8891	
3.3	112.0162	
100	112.9635	small - shoulder
100	113.907	
100	114.9229	
1.9	115.0332	
100	115.9216	
16.3	116.9441	

Peak Identity	Mass	Deviation (ppm)	Min Mass (m/z)	Max Mass (m/z)	Shift Direction	Dev.	Explained
C4Cl2-	117.9383	7.3	117.83	118.13	none	7.3	100
SiCHS2N-	118.9325	2.8	118.83	119.11	none	2.8	81.9
Si2O4-	119.9341	-12.6	119.83	120.13	+	-12.6	100
Si3C3H3-	122.9548	1.9	122.8	123.18	none	1.9	100
Si3C2H2N-	123.9501	-1.3	123.79	124.14	none	-1.3	100
Si4CH-	124.9161	-28.8	124.79	124.96	none	-28.8	100
C5H5N2O2	125.0357	3.5	124.96	125.19	none	3.5	100
Si4CH2-	125.9239	-56.6	125.78	125.98	none	-56.6	100
C5H6N2O2-	126.0435	5	125.98	126.19	none	5	100
C8H8Na-	127.0529	7.5	126.98	127.21	none	7.5	100
KClF-	127.9004	-14.7	127.77	127.98	none	-14.7	100
C9H6N-	128.0506	4.8	127.98	128.21	none	4.8	100
Si3CHS-	128.9112	24	128.79	128.99	none	24	100
C9H7N-	129.0584	5.1	129	129.23	none	5.1	100
Si2SN3-	129.9357	-8	129.79	130.23	none	-8	100
Si3HSN-	130.9143	28.4	130.79	131.2	none	28.4	100
SiS2N3-	133.9308	-5.1	133.778	134.188	none	-5.1	100
Si3H3SO-	134.9218	-6.5	134.797	135.165	none	-6.5	100
Si2H2S2N-	135.9173	12.7	135.8	136.129	none	12.7	100
C2HO2Ca2-	136.9234	6.2	136.808	137.124	none	6.2	100

AltIdentity1	Dev.	Explained	m/z	AltIdentity2	Dev.	Explained	m/z	AltIdentity3	Dev.
^29SiSiHSN2-	-7.6	32	117.94	SiC2H2S2-	15.7	100	117.9373	Si2CH2SO-	17.6
^54CrSNOH3-	-1.1	2.7	118.933	Si2HSNO-	4.7	87.2	118.9323	CSNOSc-	53.2
RhNH3-	-0.5	100	119.9326	CH3SNCo-	1.5	100	119.9324	MnSNOH3-	3.4
S2N3OH-	-13.1	100	122.9567	^29SiSiH4SNO-	-2.3	15.1	122.9553	^30SiC5HS-	6.7
O2F2Al2-	-3	100	123.9503	^30SiC4SN-	3.4	23.3	123.9495	C3H2OCl2-	8.6
^94ZrNOH-	-1.6	100	124.9127	GeH3SO-	2.4	100	124.9122	CH2SOCu-	-2.4
^13CC6H5OF-	-2.1	2.7	125.0363	^29SiSiH10N3O-	-2.2	3.9	125.0364	^30SiC5H7N2-	6.8
Si^30SiC3S-	-51.9	12.5	124.9533	CH2SN^66Zn-	-4.8	65	125.9174	CHN^99Ru-	-4.9
^29SiSiH11N3O-	-0.6	32.5	126.0442	^29SiCH11SN3-	-2.4	23.4	126.0444	^30SiC5H8N2-	8.2
^13CC3H8O2F2-	5.8	0.7	127.0531	C10H7-	-11.4	100	127.0553	^29SiSiH12N3O-	14.7
S^81BrNH-	-10.4	100	127.8998	^96SrO2-	-1.4	20.9	127.8987	^112CdO-	2
SiC3H8N4-	4.8	100	128.0524	SiH10N3O3-	11.7	100	128.0497	SiC5H10NO-	-19.7
Si4HO-	4.2	100	128.911	^98RuNOH-	-0.9	9.6	128.9116	MoNOH-	-1.8
SiC3H9N4-	-8.9	100	129.0602	Si2C5H13-	22.6	100	129.0561	C6H9O3-	25.8
CH3SNO^53Cr-	-0.6	23.3	129.9347	CH3NORb-	6.6	100	129.9338	^29SiSi3H3N-	2.2
CHN^104Pd-	19.3	100	130.9155	CH2O^101Ru-	10.1	64.9	130.9167	CHN^104Ru-	8.7
^117SnNH3-	0.8	92.7	133.9301	^29SiSi2H3SN-	4.8	79.2	133.9395	^30SiSiCO4-	-5.6
^30SiC2HSO2-	-2.1	21.2	134.9212	Si^30SiCHSO2-	-0.4	20	134.921	SiCH3S2-	-8.2
^71GaSNOH3-	1.5	7.8	135.9188	^104PdNOH2-	5.7	3.3	135.9182	C2H2^110Cd-	-1.6
Si2H3S2N-	-6.2	100	136.9251	^30SiCHS2NO-	-0.3	2.9	136.9243	^30SiSiHSNO2-	1.4

Explained	m/z	Notes
100	117.937	
100	118.9265	
100	119.9321	
50.3	122.9542	2 peaks
100	123.9488	
100	124.9128	
2.7	125.0352	
48.6	125.9174	
3.3	126.0431	
1.8	127.052	
93.3	127.8982	
100	128.0537	
100	128.9118	
100	129.0557	
23.3	129.9347	wide + shoulder
48.4	130.9169	+ shoulder
24.6	133.9309	
100	134.922	
3.4	135.9192	
2.7	136.924	

Peak Identity	Mass	Deviation (ppm)	Min Mass (m/z)	Max Mass (m/z)	Shift	Dev	Explained
Si4C2H2-	137.9239	-0.9	137.806	138.145	none	-0.9	100
Si4CHO-	140.911	-9.6	140.779	140.977	none	-9.6	100
H2O2Al4-	141.9322	10.4	141.761	142.204	none	10.4	100
Fe2O2-	143.8603	58.6	143.739	143.933	none	58.6	100
SiC7H4N2-	144.0149	3.8	143.936	144.276	none	3.8	100
Ca2HS2-	144.8777	-6.2	144.753	144.921	none	-6.2	100
C7HN2O2-	145.0044	5.4	144.925	145.279	none	5.4	100
Si4H2S-	145.896	-1.3	145.764	146.154	none	-1.3	100
Si3HS2-	148.8833	6.6	148.765	149.109	none	6.6	100
Si3H2S2-	149.8911	1.8	149.763	150.139	none	1.8	100

AltIdentity1	Dev.	Explained	m/z	AltIdentity2	Dev.	Explained	m/z	AltIdentity3	Dev.
CH3OAg-	-1.8	27.9	137.924	Si^30SiC4S-	3.4	40	137.9233	^30SiSi2C3O-	5
^124SnOH-	7.6	91.4	140.9086	^110CdNOH-	1.9	31.2	140.9094	CH3SO^78Se-	9.4
Na2SO4-	13	100	141.9318	Si3^29SiCH3N-	-5	44.4	141.9344	Si3N3O-	-12.7
^96MoSO-	-24.4	100	143.8722	^10AgCl-	-37.9	100	143.8742	Zn2O-	103.9
^29SiC7H4N2-	1.7	20.2	144.0152	^30SiC2H4N5O-	-3	3.9	144.0159	^13CC6H2F3-	4.9
^113InS-	0.8	13.6	144.8767	CaCl3-	49	100	144.8697	^113CdS-	-1.6
Si^29SiC2H6N3O-	0.5	6.7	145.0051	^30SiC7H3N2-	8.2	4.2	145.0039	C6H6O2Cl-	-7.2
CH2S^100Mo-	0.3	11.4	145.8957	Si^30SiC2S2-	2.8	4.4	145.8954	^98RuSNH2-	-5.8
CHS^104Pd-	-1.4	4.1	148.8845	^116CdHS-	-6.2	4.1	148.8852	^100MoSOH-	9.6
^118SnO2-	-3.9	22.9	149.892	^100MoH2SO-	4.9	18	149.8907	^30SiCS2O-	7.3

Explained	m/z	Notes
38.2	137.9231	
29.1	140.9083	
100	141.9355	+ shoulder
100	143.8538	
16.2	144.0148	
38.2	144.877	
100	145.0062	
3.9	145.8966	
4.6	148.8828	
100	149.8903	

Appendix Table 9. TOF-SIMS on *in situ* specimen (Fig 5). Unassigned Peaks. (2 tables of 17)

Mean Mass	Potential Identity1	Deviation	Explained	m/z	Potential Identity	Deviation	Explained	m/z
2.0178	H2	791.8	100	2.0162				
7.02	Li-	484.6	100	7.0166	^6LiH-	-504.5	0.4	7.0235
14.021	CH2-	310.5	100	14.0162	^13CHH-	629.3	15.4	14.0117
15.03	CH3-	411.6	100	15.024	^13CH2-	709	2.6	15.0196
38.013	CH3Na-	-11	100	38.0138	B2O-	-18.4	100	38.0141
39.02	C2^13CH2	25.6	6.9	39.0196	CHO^10B-	110.9	84.4	39.0162
51.02	^13CH3OF-	16.6	4.6	51.0207	C4H3-	-48.7	100	51.024
52.01	CNO^10B-	3.5	23.5	52.0115	CH2F2	-25.9	100	52.013
53	H2O2F-	4.5	100	53.0044	CH2SLi-	7.5	100	53.0043
55.02	C3H3O-	-31.1	100	55.0189	C2^13CH2O-	50.1	100	55.0189
57.03	C3H5O-	-15.1	100	57.0346	C2^13CH4O-	57.0301	63.3	0.4
57.98	CHPN-	-10.4	100	57.9852	^25MgO2H-	9.8	8.4	57.984
61.97	C2H^37Cl-	-15	100	61.9743	^29SiHO2-	-21.8	17.4	61.9747
65	H3OFAl-	8.8	100	64.9989	^13CHO2F-	-7.8	4.8	65
74	SiCH4NO-	-11.4	100	74.0068	C2H4SN-	-14.5	100	74.007
83.99	CH3SNNa-	-9	100	83.9889	SiN4-	-19	100	83.9898
86	CH3SNOBe-	-5	100	86.0063	SiC2H4NO-	-10.8	100	86.0068

Potential Identity	Deviation	Explained	m/z
N--	2545.4	100	7.0021
BH3-	-911.4	100	14.0333
NH-	1248.3	100	15.0114
C2^13CH-	43.3	21.3	38.0117
CH2OBe-	-70.3	100	39.0233
NOH2F-	175.4	100	51.0126
^13CHF-	60.1	2	52.0085
C3HO-	26.1	100	53.0033
C2H4Al-	69.8	100	55.0134
C2H6Al-	82.3	100	57.029
NaH3S-	-21.7	100	57.9859
Na2O-	-26.7	100	61.975
C3^13CO-	9.8	11.6	64.9988
BeSNOH3-	-4.7	100	74.0063
CH3NOK-	29.3	100	83.9857
C3H4SN-	-13.5	100	86.007

Mean Mass	Potential Identity1	Deviation	Explained	m/z	Potential Identity	Deviation	Explained	m/z
107.91	CHSCu-	2.8	100	107.91	^94ZrN-	3.8	100	107.9099
110.92	^77SeH2S-	0.3	17.3	110.9082	^94MoOH-	-1.4	90.2	110.9084
114	C2H4O3F2-	2.4	100	114.0134	^30SiSiC4H8-	-1.6	10.9	114.0138
120.91	C3O3^37Cl-	-10.9	100	120.9512	^30SiSiH3SN2-	-25.3	100	120.9529
121.9	^76GeSN-	-2	100	121.8971	CSO^62Ni-	7.9	25.9	121.8959
121.99	C4H7O2Cl-	-1.4	99.7	122.014	^13CC3H3O2F2-	-1.5	18	122.014
126.88	NbH2S-	-77.1	100	126.8946	^94MoHS-	-5.3	3.3	126.8855
131.88	^98RuH2S-	-2.5	4.2	131.8936	Si3SO-	-38.5	100	131.8983
132.906	CSb-	4.8	80.3	132.0944	^116SnOH-	-0.2	36	132.905
138.906	^123SbNH2-	4.2	100	138.9235	^29SiSi3C2H2-	4.3	20.2	138.9235
139.898	YH3SO-	-0.2	100	139.8969	CNOCuCl-	-1.1	100	139.897
140.01	^30SiCH8N3O3-	1.4	8.5	140.0309	Si2H10N3O2-	-4.4	100	140.0317
141.012	Si2C5H11N-	4.5	100	141.0436	C6H7NO3-	7.4	100	141.0431
142.898	^95MoSNH2-	2.2	72.4	142.8972	^92MoH3SO-	-2.2	100	142.8978
143.064	^13CC4H9OF3-	-1.1	2.2	143.0645	SiC5H11N2O-	-2.2	100	143.0646
146.891	CHNO^104Pd-	-0.6	41.7	146.9104	Si2CHS2N-	5.9	100	146.9094
147.863	^99RuSOH-	1.4	2.2	147.8813	IrHS-	-19	100	147.8843

Potential Identity 3	Deviation	Explained	m/z
^76GeO2-	-13.3	22.3	107.9118
BrO2-	-4.5	100	110.9087
SiC4H6O2	-5.1	100	114.0143
SiHSN2O2-	-28.7	100	120.9533
Si^30SiS2-	12	100	121.8954
SiCh6N2O3-	-12.2	100	122.0153
^SBrO-	-8	8.6	126.8859
Si2CS2-	-40.3	100	131.8985
Cs-	-7.4	100	132.906
PdNOH3-	-10.2	35.5	138.9255
CSNO^66Zn-	1.3	100	139.8966
C4^13CH5N3O2-	1.7	17.4	140.0308
^30SiSiH11N4O-	-2.4	9.3	141.0445
CuPO3H-	7.1	100	142.8965
C6H11SN2-	-3.8	100	143.0648
Si3HSNO-	7.5	100	146.9092
CHSRh-	-30	100	147.8859